Four Point Bending Test in Thermal Barrier Coating System

Yasuhiro YAMAZAKI

February 2005

Contents

page

Four Point Bending Test in Thermal Barrier Coating Systems

Yasuhiro YAMAZAKI*
*Guest researcher from Niigata Institute of Technology, JAPAN

This is the report of my work at Institute of Materials Technology, Darmstadt University of Technology (Sep., 2, 2004 - Feb., 27, 2005). The aim of my work was to evaluate and investigate of the delamination resistance for thermal barrier coating systems by means of the four point bending test.

1. Introduction

Industrial gas turbines are used as electrical generators by both utilities and private industrial companies [1-10]. Nowadays so called 1500˚C level combined cycle gas turbines have been developed, which can provide thermal efficiencies greater than 55% [3]. The durability of a gas turbine is principally limited by those components operating at high temperatures in the turbine sections because those are exposed to hot gas. Thermal barrier coatings (TBC), that reduce the temperature in the underlying substrate material, are an essential requirement for the hot section components. A typical TBC system is composed of an oxidation resistant metallic bond coat (BC) on the superalloy substrate and a thermal insulating ceramic top coat (TC) attached to the BC. To take full advantage of the potential of TBC systems, the evaluation and the prediction of the lifetime of TBC systems are important. Therefore experimental and the analytical investigations in the TBC systems have been performed by many authors [4-10]. As a result of these energetic studies, it has clearly been shown that the adherence of TC is the most important parameter for the durability of TBC system [6-8, 14]. It was also cleared by recent investigations that thermal grown oxide (TGO) grows at the TC/BC interface due to the thermal aging as well as thermal cycle. In addition, it was believed that the TGO prays the important role in the spallation of TBC systems.

The final goal in this project is the development of a reliable life time model for the TBC systems. The object of the present work was to evaluate and investigate the delamination resistance of TBC systems by means of four point bending tests. The effects of thermal aging and TC/BC interface roughness on the delamination resistance were also discussed.

2. Literature Assessment

Before the tests, the literature, that reported about the evaluation and the investigation of the interfacial properties of coated materials by means of four point bending tests, was investigated and evaluated [11-18]. A summary of the literature evaluation is listed in Table 2-1 and Table 2-2.

Charalambides et al. proposed and discussed the evaluation of the critical energy release rate at the metal/ceramic interface by means of four-point bending tests [13]. This method has the advantage that

the specimen geometry and test technique are simple. The critical energy release rate by delamination at the metal-ceramic interface can be determined easily by using this method. However, this method is applicable to only for thick coated materials that have relatively high fracture toughness to prevent the vertical cracking. If it is applied to thin brittle coated material such as TBC systems, the vertical cracking and segmentation decrease the stored elastic energy and make the evaluation of the interface fracture energy significantly more difficult.

Hofinger et al. proposed a simple modification of the Charalambides test in order to evaluate the interfacial fracture toughness of thin brittle layers tending to separate by vertical cracks [11]. The modification by Hofinger is the bonding of a stiffener on the top of the thin brittle surface layer. This stiffening layer suppresses the segmentation of the brittle layer and increases the stored energy in the layer and therefore the driving force for delamination. Another advantage of this method is that an analytical solution is possible. This modified Charalambides test is suitable to evaluate the delamination resistance in TBC systems.

In this work, the delamination resistance of TBC systems was evaluated by means of the modified Charalambides 4-point bending test.

According to the literature assessments, most of the 4 – point bending test were perfumed under 1mm/min displacement speed or 5N/sec load speed. In this work, a constant loading rate of 5N/sec. was chosen.

Table 2-1 Results of literature evaluation.

Lit-No.	Alloy substrate	Bond coat	Top coat	Specimen size L,W,H	Environment, humidity	Loading rate	Bending type	Results	others
1	High alloyed steel t=3.7 mm (stiffer is same)	none	Plasma sprayed ZrO_2 t=2.3 mm	80 13 9.7 mm	R.T. Humidity :None	None (displacement control)	4-point	G_c?60 N/m	Using Stiffer
2	IN 617 Ni-base alloy	NiCrAlY (APS) t=0.1 -0.2 mm	8YSZ (VPS) t=0.3-0.5 mm	? 2.22-3.88 1.83-3.0 mm	R.T. and 800°C Humidity :None	**2.5 N/s**	4-point	G_c?131kN/m (as, RT) ?170kN/m (aged, RT) ?5.4kN/m (as, 800°C)	Effect of aging (1000°C for 200h)
3	PMMA (Acrylic resin)	None	Al	? ? >6 mm	R.T. Humidity :None	None (displacement control)	4-point	G_c? 11.5J/m2	Al bonded to PMMA using epoxy
4	CMSX-4 Ni-base superalloy t=2 mm	MCrAlY (?) t=0.15 mm	YSZ (APS) t=0.3 mm	80 6 4 mm (Gage L=20mm, t=2mm)	R.T. Humidity :None	0.035 mm/min (displacement control)	4-point	$\varepsilon_{delamination}$?+0.0045 ?-0.004 $\varepsilon_{segmentation}$?+0.01 ?-0.011	Porosity? 13 %
5	Tomilloy Ni-base superalloy t=5 mm	CoNiCrAlY (VPS) t=0.1 mm	8YSZ (APS) t=0.3 mm	50 5 5.4 mm	R.T. Humidity :None	0.002 mm/s (? 10 N/s*)	4-point	G?150 N/m (non-aged) ?300 N/m (aged 100h) ?150 N/m (aged >500h)	Aged at 1100°C for 100, 500, 1000 h

t: thickness, *: calculated from Load-displacement curves **: Critical load for crack initiation

Table 2-1 Results of literature evaluation (continued).

6	Hasteloy-X Ni-base superalloy t=3.0 mm	NiCrAlY (APS) t=0.1 mm	8YSZ (APS) t=2.0 mm	40 4 5.1 mm	R.T. Humidity :None	None (displacement control)	4-point	P_c** ? 650 N (non-aged) 550 N (aged >500h)	Aged at 900°C for 1, 10, 50, 500, 1000, 1500, 2000 h
7	MM247 Ni-base superalloy t=5 mm	CoNiCrAlY (VPS) t=0.1 mm	8YSZ (APS) t=0.5 mm	50 5 5.6 mm	R.T. Humidity :None	0.005 mm/s (? 10 N/s*)	4-point	P_c** ? 5000N COD_c ? 20 μm	AE COD
8	MM247 Ni-base superalloy t=5 mm	CoNiCrAlY (VPS) t=0.1 mm	8YSZ (APS) t=0.5 mm	50 5 5.6 mm	R.T. Humidity :None	0.005 mm/min (? 10 N/s*)	4-point	$\varepsilon_{c,interfacial}$? 0.014 (as) ? 0.015(aged)	AE

t: thickness, *: calculated from Load-displacement curves **: Critical load for crack initiation

Table 2-2 List of literature.

Lit. No.	Ref. No	Author name	Title of paper	Other information	Key words
1	11	I. Hofinger M. Oechsner, H. Barhr, M. V. Swain	Modified four-point bending specimen for determining the interface fracture energy for thin, brittle layers.	Modification of bending tests using stiffening layer to suppress the segmentation of the brittle layer, Plasma sprayed ZrO_2 coating (t=2.3 mm) on high alloyed steel substrate	Fracture mechanics, Four-pint bending, Delamination, Interface fracture energy
2	12	A. K. Ray, N. Roy, K. M. Godiwalla	Crack propagation studies and bond coat properties in thermal barrier coatings under bending.	Effects of test temperature and aging process on crack propagation, tested at R. T. and 800°C, Aged at 1000°C for 200 h	Coating, Thermal barrier, Bond coat. Superalloy, Crack propagation, Zirconia, Plasma spraying, stress, strain, modulus
3	13	P. G. Charallambides, J. Lund, A. G. Evans, R. M. McMeeking	A test specimen for determining the fracture resistance of biomaterial interfaces	Al/PMMA as a model material couple	
4	14	D. Renusch, H. Echsler, M. Schutze	New approaches to the understanding of failure and life time prediction of thermal barrier coating systems	Life time prediction	
5	15	T. Onoki, K. Ogawa, T. Shoji, H. Torigoe	Influence of thermal aging on interface delamination of thermal barrier coatings	TBC removed without inner load span region.	TBC, Thermal aging, TGO, DCB test, 4-point bending test, Interface strength
6	16	M. Arai, U. Iwata, T. Sakuma, M. Saitoh	Effect of a delamination initiation strength between thermal barrier coating and base metal on thermal aging	Notched specimen.	Gas turbine, TBC, Delamination strength, 4-point bending test, TGO
7	17	K. Takaki, K. Kubo, K. Fujiyama	Report of sub-committee "Superalloy and coatings"	Notched TBC bending specimen. MM-247 substrate, CoNiCrAlY(VPS), 8YSZ(APS)	
8	18	K. Ogawa	Report of sub-committee "Superalloy and coatings"	AE, TBC bending specimen, MM-247 substrate, CoNiCrAlY(VPS), 8YSZ(APS)	

3. Design and Preparation of the Test Rig

3. 1 Determination of spring constant of the spring unit

In the present work, a creep machine was used to apply the loading to the specimen (see section 6-2). Since this machine can apply only a constant displacement $\dot{\delta}$ which is 7 mm/min, a spring unit that can convert the constant displacement speed into a constant loading rate was designed and used.

The relationship between load and displacement of the spring is shown in Fig. 3-1. From this result the spring constant k and the initial tension loading $P_{initial}$ were 7.48 N/m and almost 50 N, respectively.

If the spring unit consists of 6 parallel springs with a spring constant of 7.48 N/mm (as shown in Fig. 3-2), the total spring constant k_6 is 44.9 N/mm. Then, the loading speed $\dot{P}$ can be achieved as following:

$$\dot{P} = k_6 \times \dot{\delta} = 44.9N/mm \times 7/60mm/\sec. = 5.24N/\sec.$$

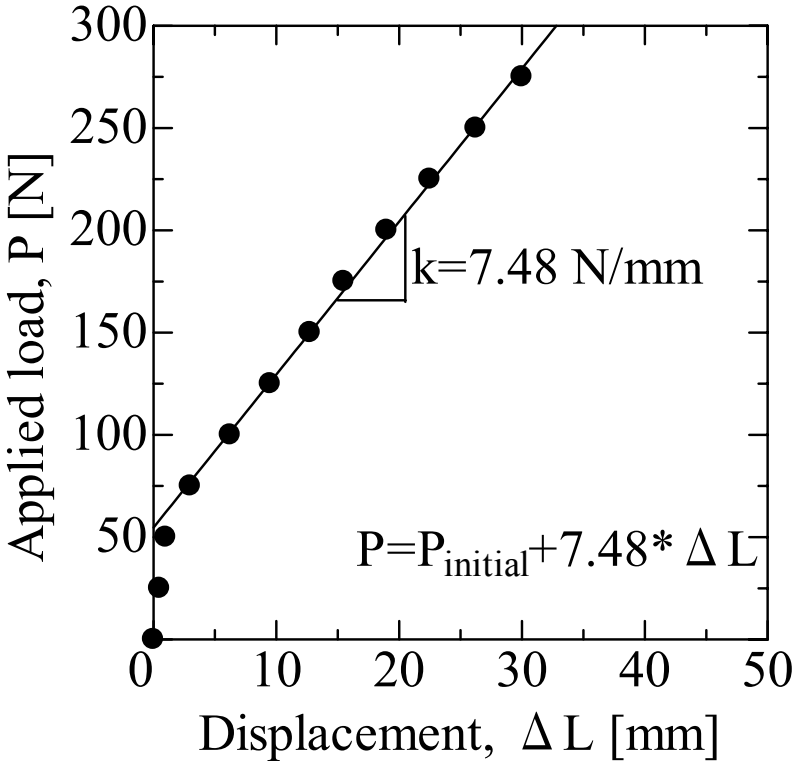

Fig. 3-1 The relationship between the applied loading and the displacement for the chosen spring.

3. 2 Design of the Test Rig

The test rig was designed as shown in Fig. 3-2. This test rig consists of a load cell with a load capacity of 2 kN, the spring unit with the four point bending device, extensometer and some attachments. The draftings of the main parts are shown in Fig. 3-3, 3-4, 3-5, 3-6, 3-7 and 3-8. The manufactured and assembled test rig is shown in Fig. 3-9.

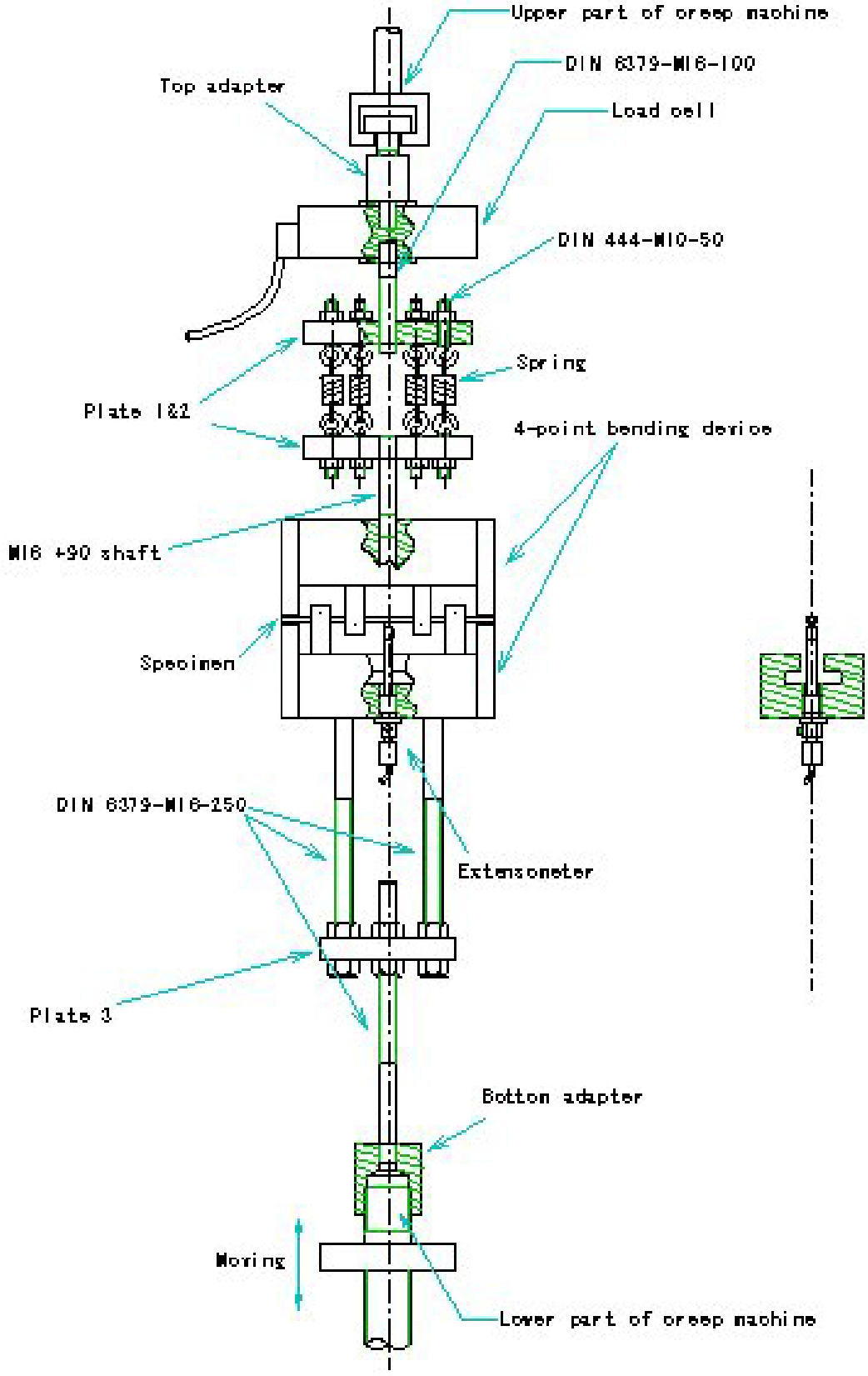

Fig. 3-2 Overview of the test rig.

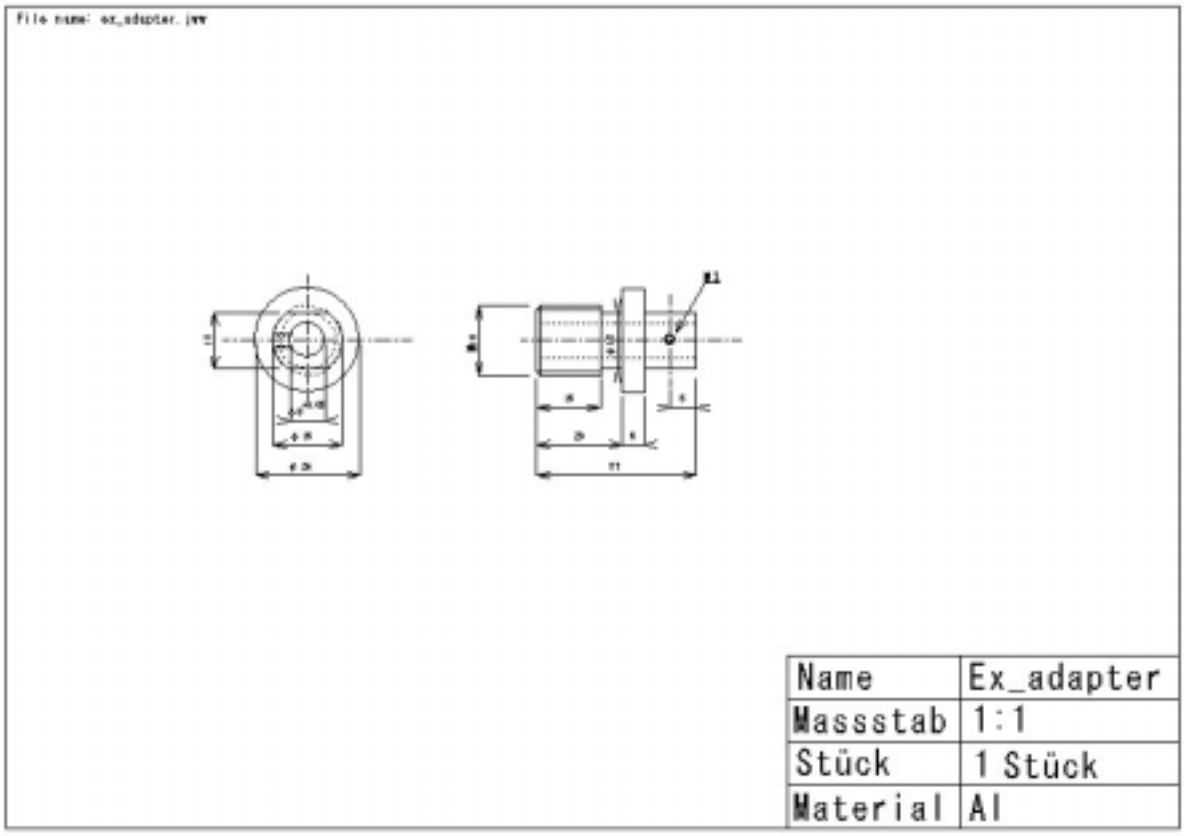

Fig. 3-3 Drafting of the extensometer adapter.

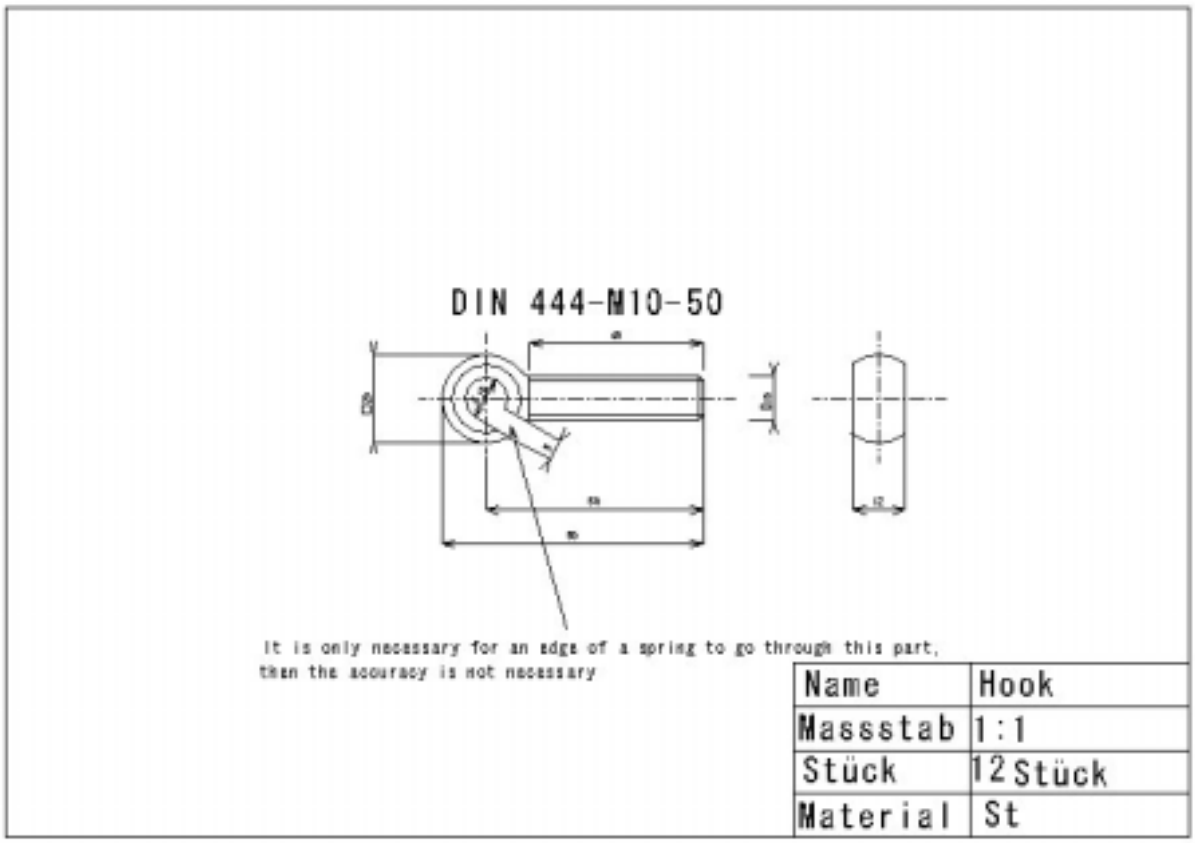

Fig. 3-4 Drafting of the hook for the springs.

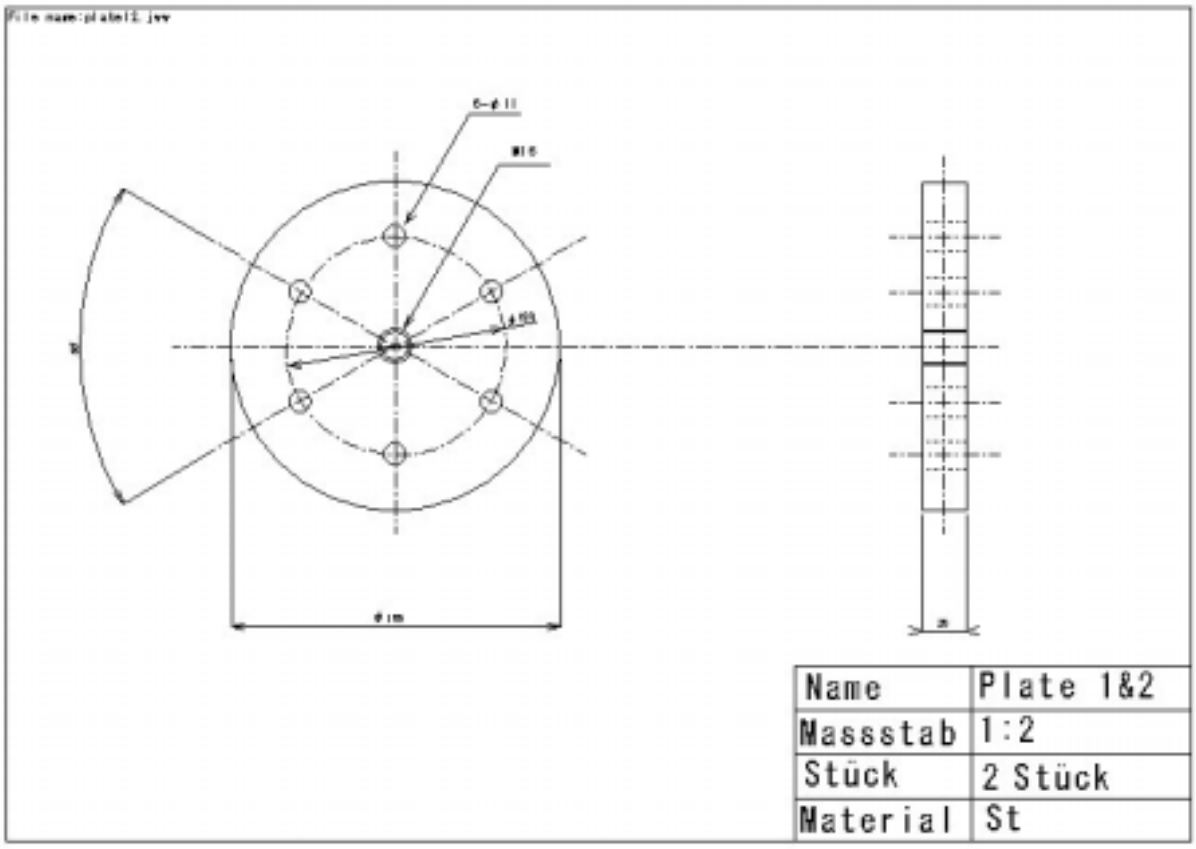

Fig. 3-5 Drafting of plate 1 and 2.

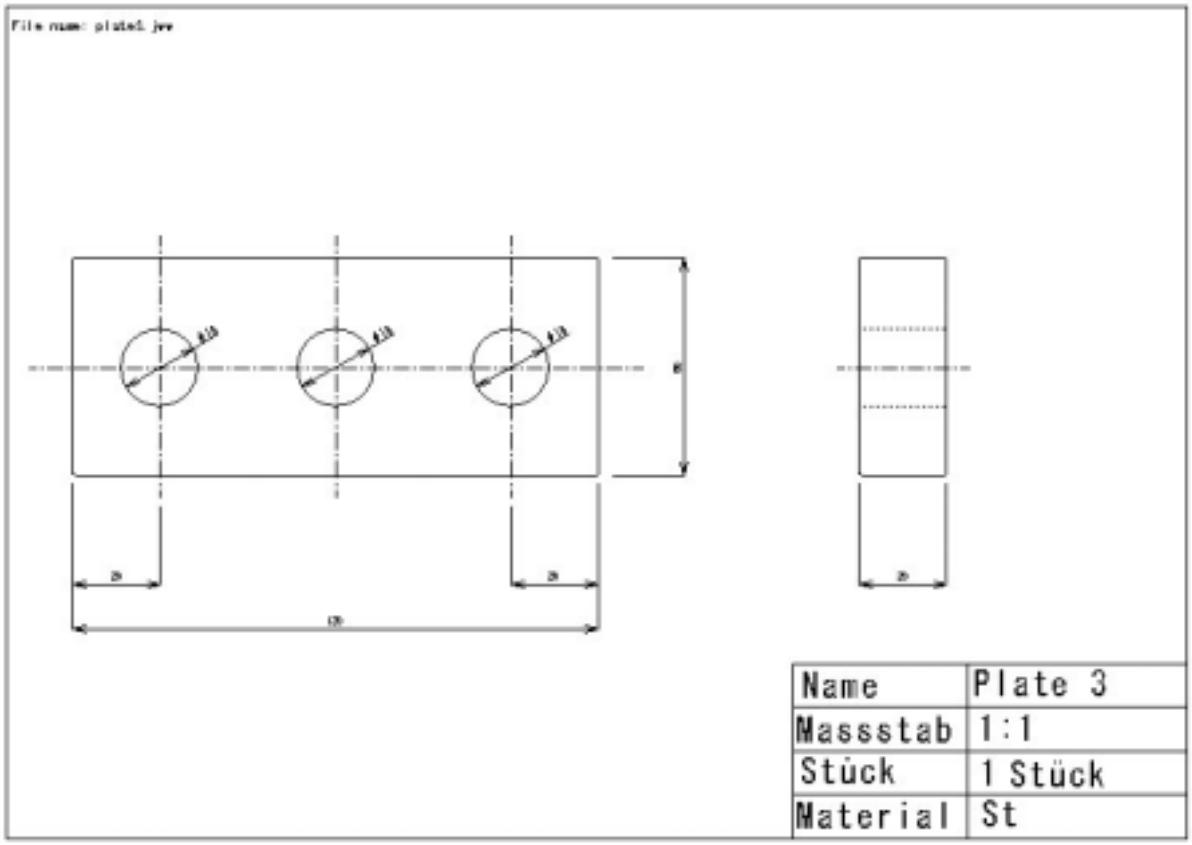

Fig. 3-6 Drafting of plate 3.

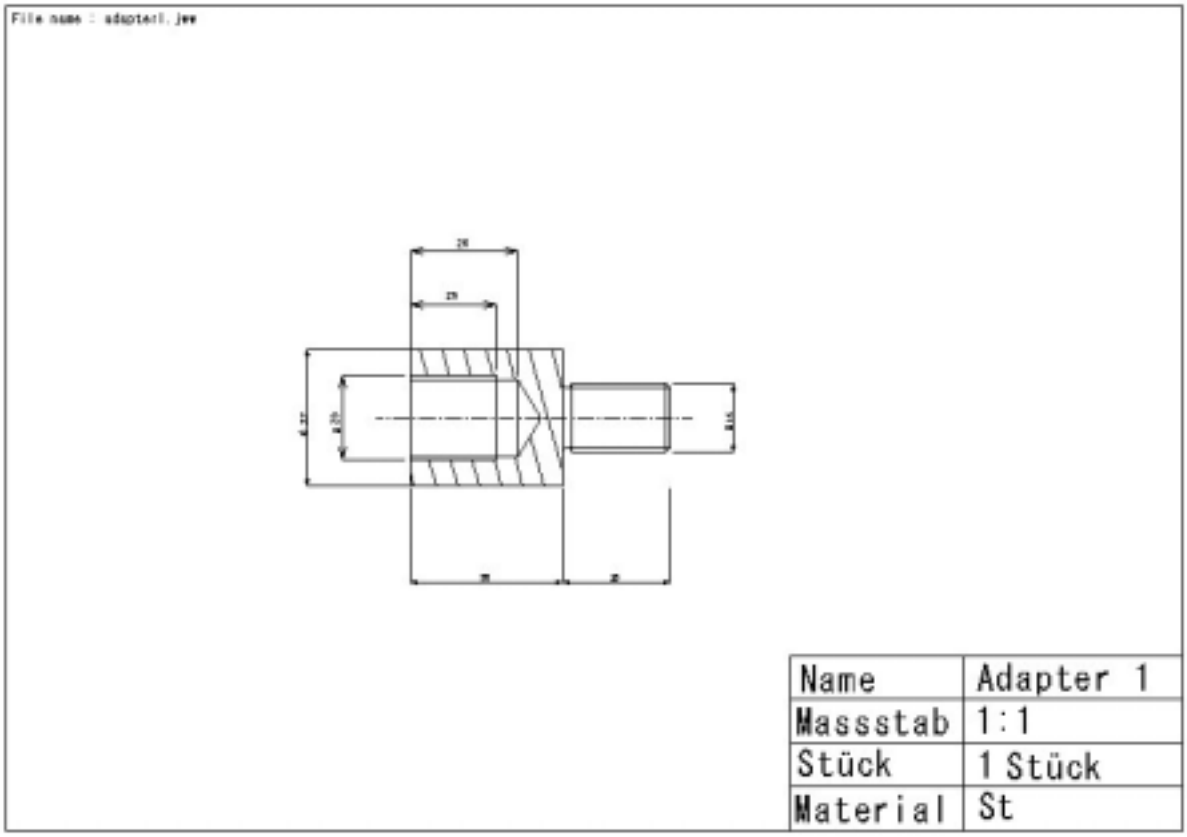

Fig. 3-7 Drafting of adapter 1 (to connect creep machine and load cell).

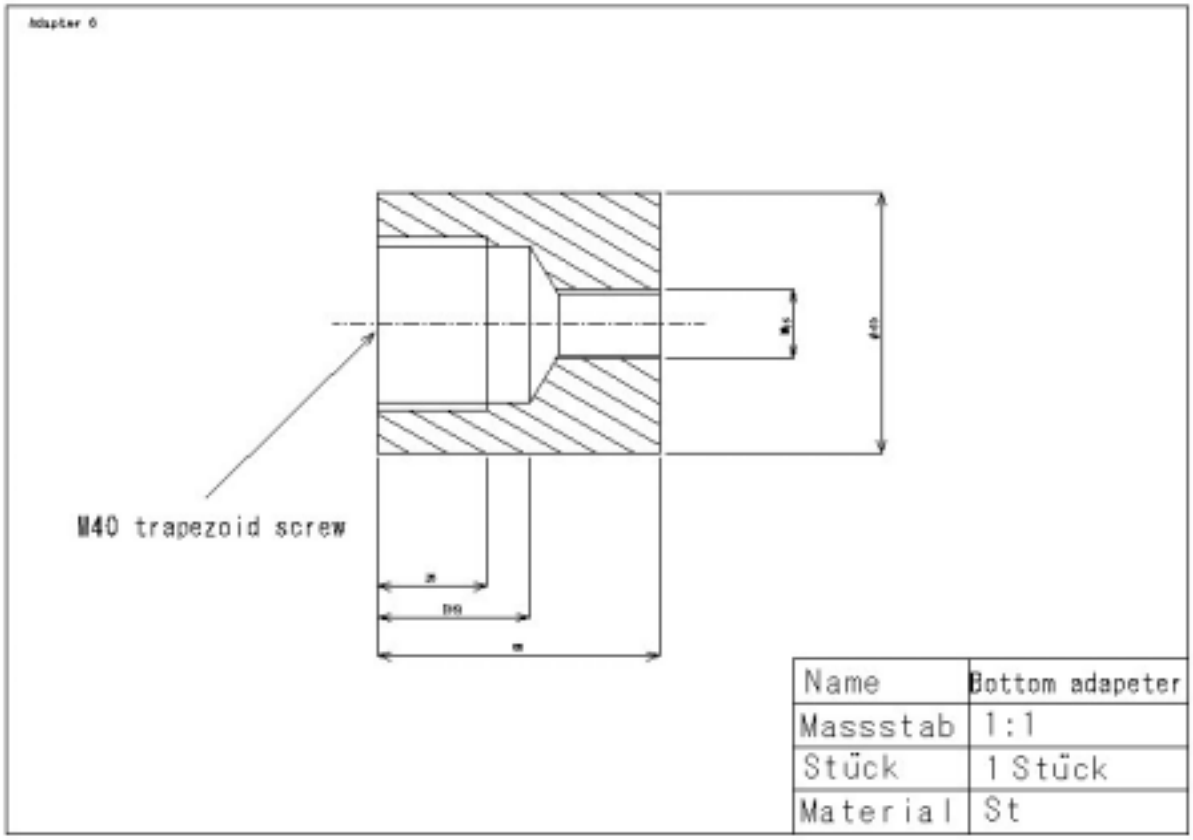

Fig. 3-8 Drafting of bottom adapter (to connect the test rig to creep machine).

Fig. 3-9 Photograph of the test rig.

4. Material and Specimen Preparation

The 8wt.% yttria partially stabilized zirconia, 8YSZ, was used as top coat (TC) layer and was deposited on the bond coat by air plasma spraying. The single crystal Ni-base superalloy CMSX-4 prismatic bar of 5 mm in thickness and 10 mm in width was used as the substrate. The CoNiCrAlY alloy, LCO22, was selected as the bond coat (BC) layer between TC and substrate. In the present work, in order to study the effect of the interface roughness between BC and TC, two kinds of the LCO22 powder with different particle size were used. In this work, the specimens which were sprayed with fine grain LCO22 powder are called fine BC specimens, and those which were sprayed with coarse powder are called coarse BC specimens. The typical surface morphology of the BC is shown in Fig. 4-1. The surface profile and surface roughness of the BC for each specimen are shown in Fig. 4-2 and Table 4-1, respectively.

It was revealed by recent investigations that thermal grown oxide (TGO) grows at the TC/BC interface due to the thermal aging as well as thermal cycling. In addition, TGO prays an important role in spallation fracture in TBC system. In this work, the effect of the TGO thickness on the delamination resistance of the TBC system was also studied. Typical microstructures near the TC/BC interface after thermal exposure at 1000˚C are shown in Fig. 4-3. From these microstructural observations, the TGO thickness was measured and compared with the aging time. The TGO thickness as a function of aging time is shown in Fig. 4-4. In this figure, the TGO thickness increased with increasing aging time. It can be estimated from Fig. 4-4 that the thickness of the TGO is approximately 3, 5 and 7μm after aging for 200, 1000 and 2000 h, respectively. Then, some bending specimens were exposed at 1000˚C for 200 hr, 1000 hr and 2000 hr. The parameters of the specimens are summarized in Table 4-2.

The prismatic notched bar specimens that were 130 mm in length, 10 mm in width and approximately 9.9 mm in thickness (including stiffener), were prepared as shown in Fig. 4-5. The thicknesses of the top coat and the bond coat were approximately 350 μm. The mechanical notch with a width of 2 - 3 mm was induced in the top coat of the specimen's center after the thermal exposures.

In this work, in order to prevent vertical cracking in the top coat, namely to inhibit the segmentation of the top coat, the stiffener with the size of 60×10×4.2 mm was bonded on top coat by adhesion (Araldite AT1), as shown in Fig. 4-5. The material of the stiffener was structural steel. The details of the bonding procedure will be explained in section 6. 1.

The mechanical and thermal properties of substrate, bond coat, top coat, stiffener and TGO are summarized in Table 4-3.

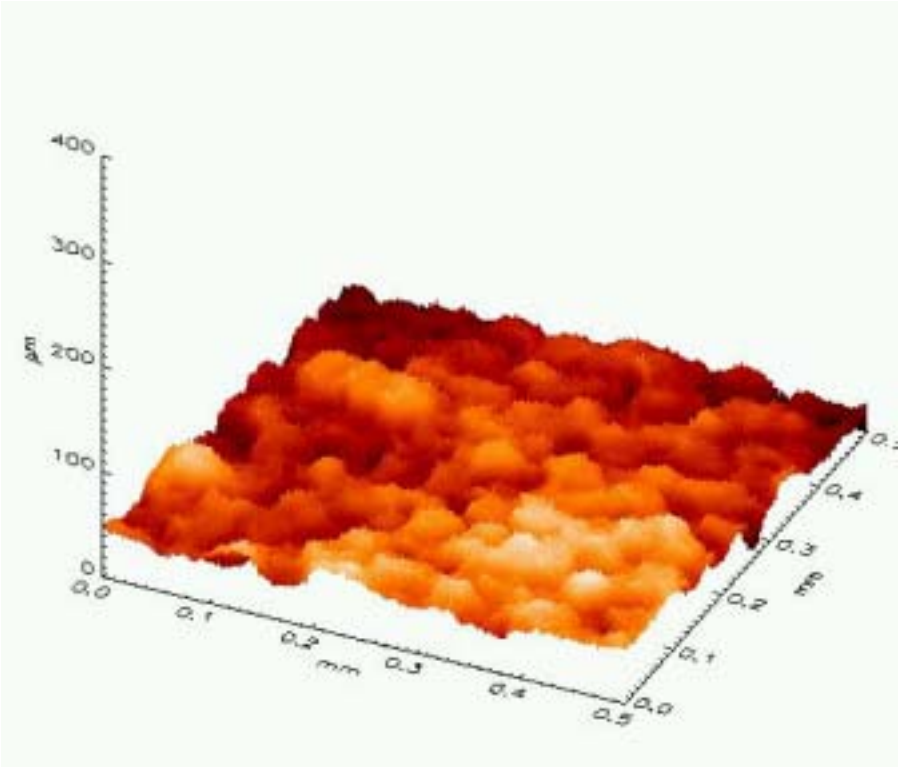

Fig. 4-1 Typical result of an optical measurement of bond coating surface roughness: fine bond coat specimen.

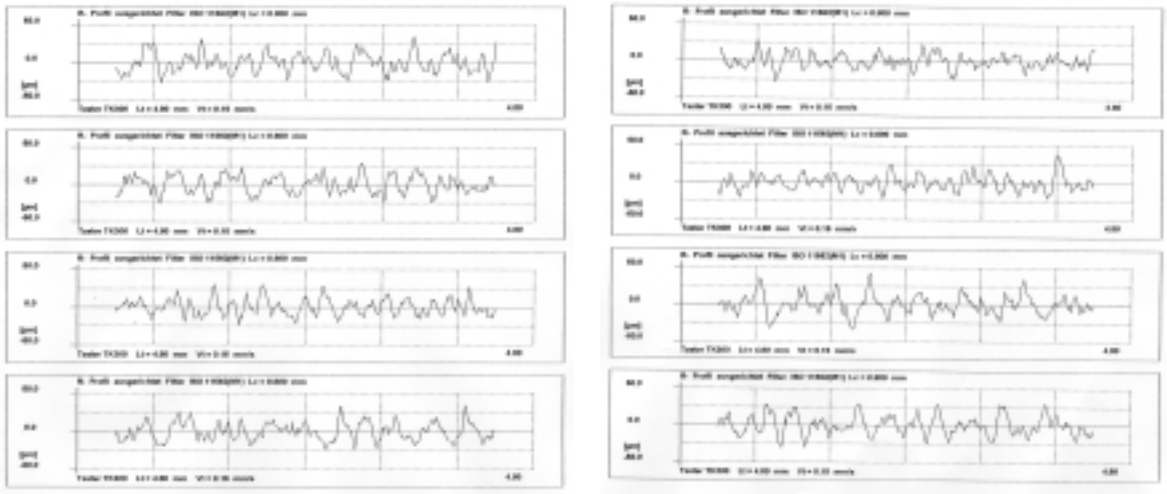

(a) for fine bond coat specimen (b) for coarse bond coat specimen

Fig. 4-2 Surface profiles of bond coat surface.

Table 4-1 Surface roughness of bond coat surface, R_a (unit in μm)

Specimen	Average	Measurement value			
Fine bond coat	8.71	7.14	7.67	9.68	10.36
Coarse bond coat	9.52	10.27	9.89	8.36	9.55

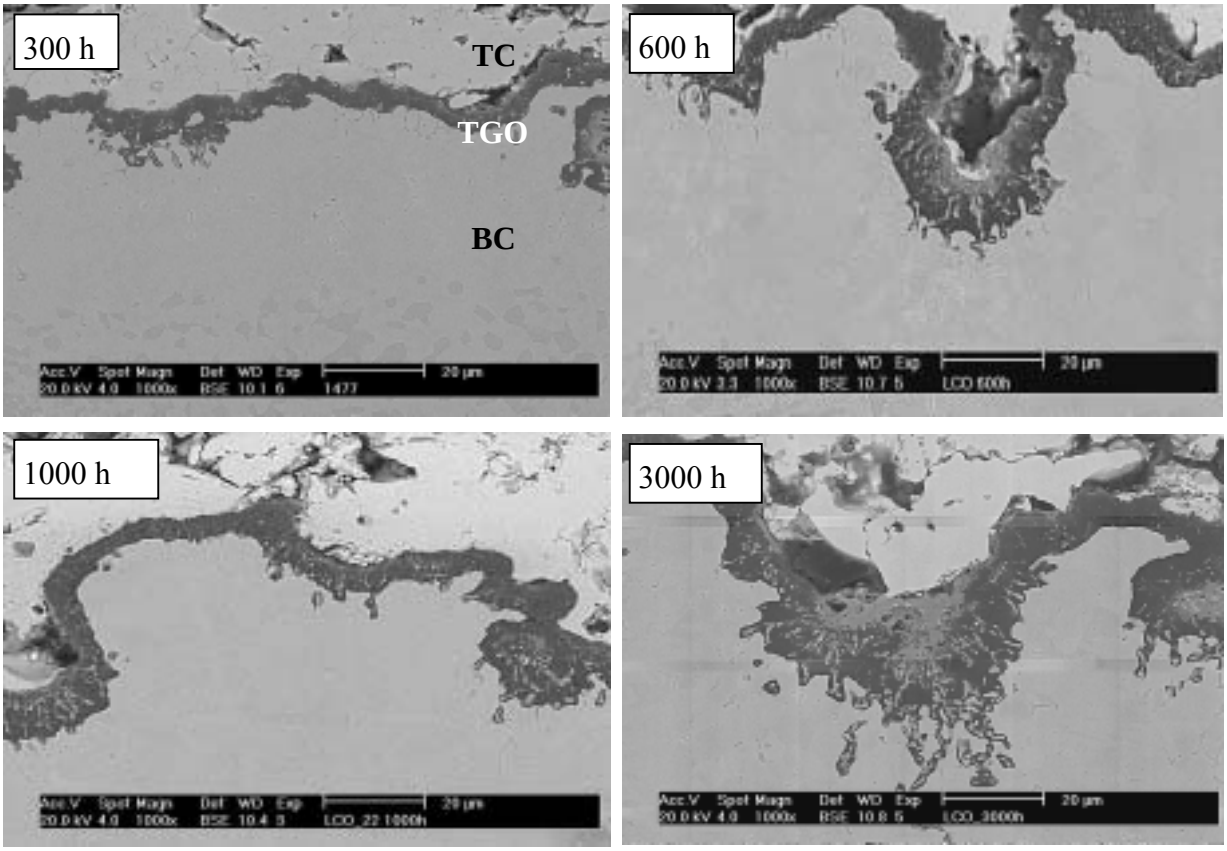

Fig. 4-3 Typical microstructure near TC/BC interface and TGO after aging at 1000°C.

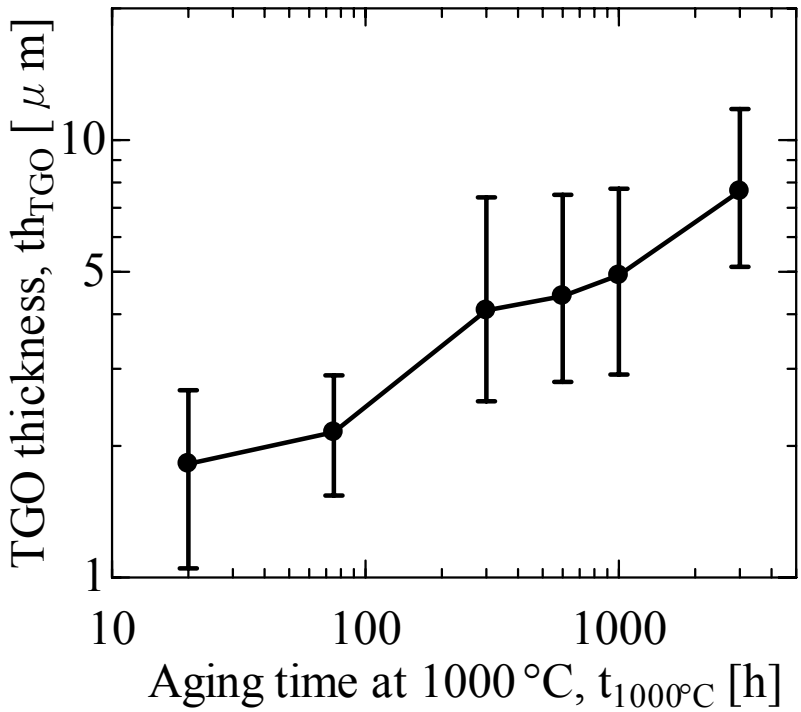

Fig. 4-4 Relationship between TGO thickness and aging time at 1000°C.

Table 4-2 Parameters of the specimens used.

Specimen No.	Bond coat powder size (LCO22)	Thickness of bond coat [μm]	Thickness of APS YSZ [μm]	Isothermal oxidation at 1000˚C	Estimated TGO thickness [μm]
C01-C04	Fine	360	340	0 h	0
C05, C06	Fine	360	340	200 h	3
C07, C08	Fine	360	340	1000 h	5
C09, C10	Fine	360	340	2000 h	7
C18-C20	Coarse	350	330	0 h	0
C12, C13	Coarse	350	330	200 h	3
C14, C145	Coarse	350	330	1000 h	5
C16, C17	Coarse	350	330	2000 h	7

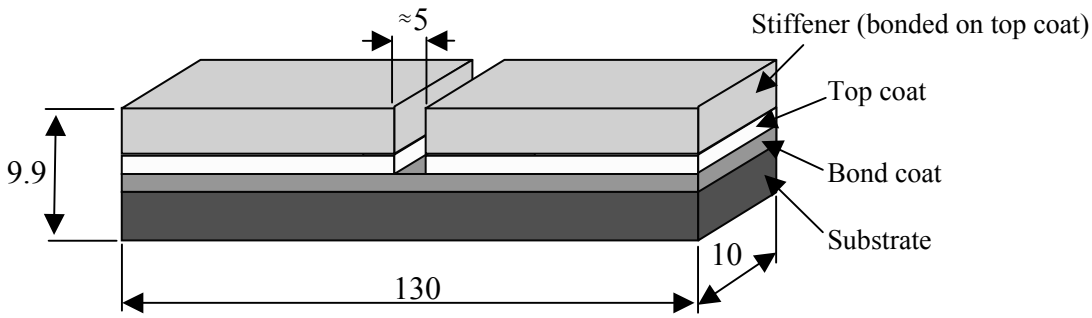

Fig. 4-5 Geometry of specimen used (in mm).

Table 4-3 Mechanical and thermal properties of materials.

	CMSX-4	LCO22	TGO	8YSZ	Steel
Young's modulus [GPa]	135.4 (R.T.) 80 (1000˚C)	183 (R.T.) 80 (1000˚C)	310 (R.T.) 270 (1000˚C)	50 (R.T.) 18.8 (1000˚C)	205 (R.T.)
Density [kg/m^3]	8720	10000	3860	5600	7800
Thermal expansion coefficient [10^{-6} K^{-1}]	10. 4 (R.T.) 15.6 (1000˚C)	12.2 (R.T.) 17.4 (1000˚C)	5.1 (R.T.) 9.8 (1000˚C)	9.68 (R.T.) 10.34 (1000˚C)	-
Heat capacity [$Jkg^{-1}K^{-1}$]	390 (R.T.) 650 (1000˚C)	538 (R.T.) 1149 (1000˚C)	1050 (R.T.) 1050 (1000˚C)	550 (R.T.) 630 (1000˚C)	-
Thermal conductivity [$Wm^{-1}K^{-1}$]	10.4 (R.T.) 23.0 (1000˚C)	20.5 (R.T.) 34.2 (1000˚C)	4 (R.T.) 4 (1000˚C)	0.605 (R.T.) 0.713 (1000˚C)	-

5. Analytical Considerations

5. 1 Model and parameters

For the composite which consists of k layers, with the Euler-Bernoulli beam theory, it can be assumed that each layer is deformed in the same curvature by the applid bending moment, M, as shon in Fig. 5-1.

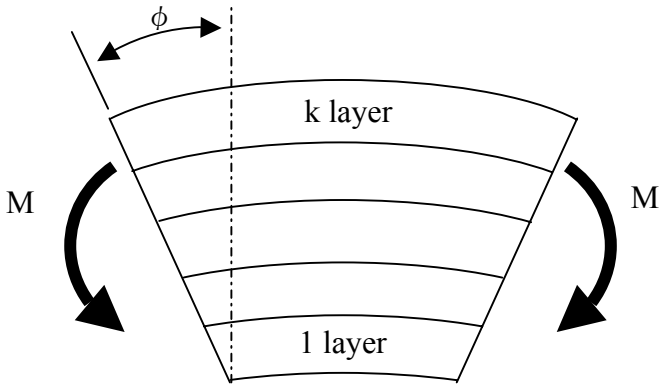

Fig. 5-1 Schematic illustration of bending deformasion in k-layer composite.

With the applied bending moment M, when the delamination occurrs between the layers j and j+1 of the k-layer composite, as shown in Fig. 5-2, the strain energy per unit crosscection before and after delamination are as follows;

for befor deramination,

$$U_k = \frac{M_b^2}{2E_{c,k}^* I_{c,k}^*} \quad \text{Eq. 1}$$

after deramination,

$$U_j = \frac{M_b^2}{2E_{c,j}^* I_{c,j}^*} \quad \text{Eq. 1}$$

where, $E^*_{c,k}$ and $E^*_{c,j}$ are the Young's moduli for the composite which consists of k layers $I^*_{c,k}$ and $I^*_{c,j}$ are second moments per unit width for the composite which consists of k layers, and M_b is the applied bending moment per unit width shown by

$$M_b = M / b \quad \text{Eq. 3}$$

Therefore when the delamination occurrs between j and j+1 layers in the k-layer composite, the energy releace rate by delamination is

$$G_c = -\Delta U = U_j - U_k \quad \text{Eq. 4}$$

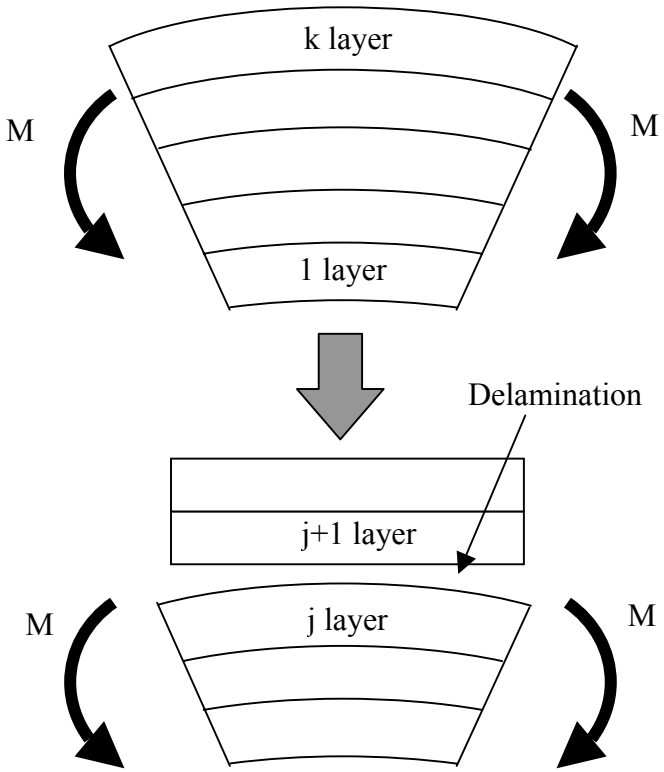

Fig. 5-2 Schematic illustration of delamination for the k-layer composite.

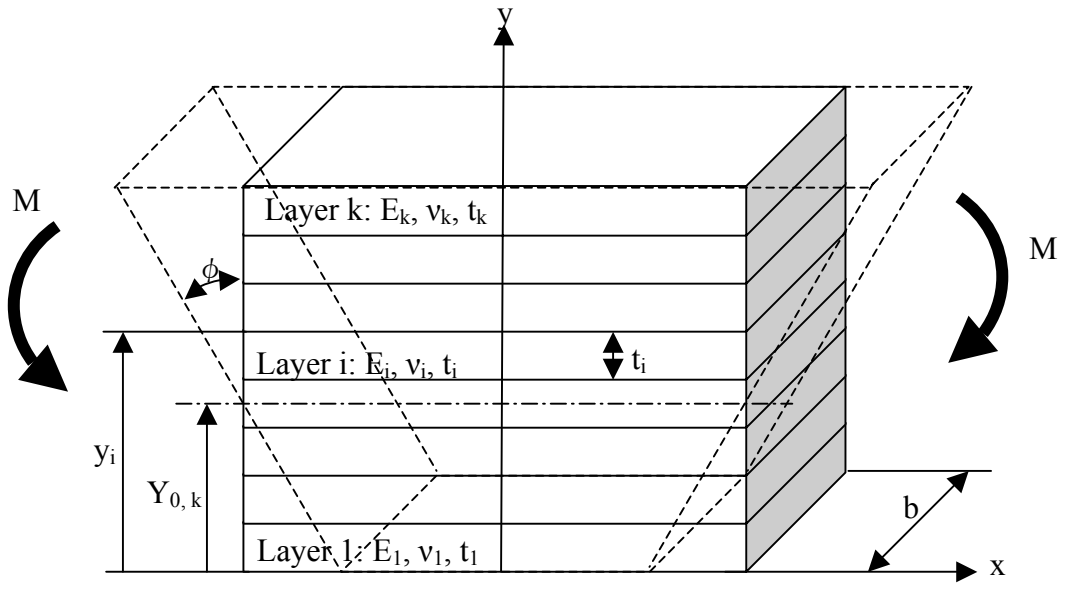

Fig. 5-3 Schematic illustration of the deformed k-layer composite due to bending moment.

The prameters used were as follows. (See Fig. 5-3)

At i-layer,

Young's modulus, E_i

$E^*_i = E_i /(1-\nu_i^2)$: fro plane strain

$= E_i$: for plane stress Eq. 5

Poison ratio, ν_i

Thickness, t_i

Second moment of area, I_i

Second moment of area per unit width, I^*_i

Apparent width, $b'_i=b\times E^*_i/E^*_{c,n}$ (see section 5.2)

For the composite which consists of k layers,

Young's modulus, $E_{c,k}$

$E^*_{c,k} = E_{c,k} /(1-\nu_{c,k}^2)$: fro plane strain

$= E_{c,k}$: for plane stress Eq. 6

Poison ratio, $\nu_{c,k}$

Second moment of area, $I_{c,k}$

Second moment of area per unit width, $I^*_{c,k}$

Width, b

Common

$y_i=\sum_{i=1}^{i} t_i$, & $y_0=0$ Eq. 7

Applied bending moment per unit width, M_b

$M_b=M/b$

5. 2 Instruction and Expansion of the Equation of the Energy Release Rate for k-Layer Composites

For k-layer composite, the Young's modulus can be calculated by following mixture law.

$$E^*_{c,k} = \frac{\sum_{i=1}^{k} t_i E_i^*}{\sum_{i=1}^{k} t_i} \qquad \text{Eq. 8}$$

Now, let us consider the transformation from the k-layer composite to monolithic material of which the cross section isn't rectangle, as shown in Fig. 5-4; i.e., from the k-layer composite of which the cross section is simple rectangle Fig. 5-4 (a), to the monolithic material different widths Fig. 5-4 (b). To keep the same deformation resistance, Eq. 9 must be satisfied.

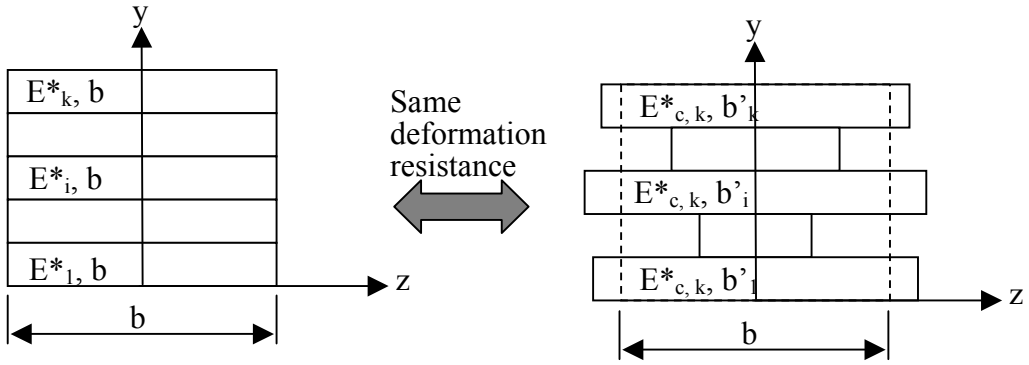

Constant width, b — Variable width, b'_i

Variable Young's modulus, E^*_i — Constant Young's modulus, $E^*_{c,k}$

(a) (b)

Fig. 5-4 Relationship between the original width and the apparent width.

$$\frac{b'}{b} = \frac{E_i^*}{E_{c,k}^*} \quad \text{Eq. 9}$$

Therefore, the statical moment of the area for the k-layer composite S_k is

$$S_k = \int_A y dA = \sum_{i=1}^{k} \int_{y_{i-1}}^{y_i} y b'_i \, dy = \sum_{i=1}^{k} b'_i \left[\frac{y}{2} \right]_{y_{i-1}}^{y_i} = \frac{1}{2} \sum_{i=1}^{k} b'_i \, (y_i^2 - y_{i-1}^2) \quad \text{Eq. 10}$$

Then the position of neutral axis for the k-layer composite $Y_{0,k}$

$$Y_{o,k} = \frac{S_k}{A} = \frac{\frac{1}{2}\sum_{i=1}^{k} b'_i \, (y_i^2 - y_{i-1}^2)}{\sum_{i=1}^{k} b'_i \, (y_i - y_{i-1})} = \frac{\sum_{i=1}^{k} b'_i \, (y_i^2 - y_{i-1}^2)}{2\sum_{i=1}^{k} b'_i \, t_i} \quad \text{Eq. 11}$$

From Eq. 9, Eq. 11 becomes

$$Y_{o,k} = \frac{\sum_{i=1}^{k} E_i^* \, (y_i^2 - y_{i-1}^2)}{2\sum_{i=1}^{k} E_i^* t_i} \quad \text{Eq. 12}$$

On the other hand, the second moment of area for the i-layer in the k-layer composite $I_{k,i}$ is,

$$I_{k,i} = b'_i \frac{t_i^3}{12} + b'_i \, t_i \left(\frac{y_i + y_{i-1}}{2} - Y_{0,k} \right)^2 \quad \text{Eq. 13}$$

Then, second moment of area for k-layer composite $I_{c,k}$ is

$$I_{c,k} = \sum_{i=1}^{k} \left\{ b'_i \frac{t_i^3}{12} + b'_i t_i \left(\frac{y_i + y_{i-1}}{2} - Y_{0,k}\right)^2 \right\} \qquad \text{Eq. 14}$$

Therefore per unit width,

$$I^*_{c,k} = \frac{1}{b} \sum_{i=1}^{k} b'_i \left\{ \frac{t_i^3}{12} + t_i \left(\frac{y_i + y_{i-1}}{2} - Y_{0,k}\right)^2 \right\}$$

$$I^*_{c,k} = \frac{1}{E^*_{c,k}} \sum_{i=1}^{k} E^*_i \left\{ \frac{t_i^3}{12} + t_i \left(\frac{y_i + y_{i-1}}{2} - Y_{0,k}\right)^2 \right\} \qquad \text{Eq. 15}$$

Consequently, if the delamination occurred between the layers j and j+1 of the k-layer composite, the energy release rate G_c is:

$$G_c = \frac{M_b^2}{2} \left\{ \frac{1}{E^*_{c,j} I^*_{c,j}} - \frac{1}{E^*_{c,k} I^*_{c,k}} \right\} \qquad \text{Eq. 16}$$

where,

$M_b^2 = M / b$, $\quad y_i = \sum_{i=1}^{i} t_i$,

$$E^*_{c,k} = \frac{\sum_{i=1}^{k} t_i E^*_i}{\sum_{i=1}^{k} t_i},$$

$$I^*_{c,k} = \frac{1}{E^*_{c,k}} \sum_{i=1}^{k} E^*_i \left\{ \frac{t_i^3}{12} + t_i \left(\frac{y_i + y_{i-1}}{2} - Y_{0,k}\right)^2 \right\},$$

$$Y_{o,k} = \frac{\sum_{i=1}^{k} E^*_i (y_i^2 - y_{i-1}^2)}{2 \sum_{i=1}^{k} E^*_i t_i}$$

For 2 layers composite, the Eq. 16 equals the Charalambides's equation [1], when $h_1=t_2$, $h_2=t_1$ and the indexes are changed, 1➔2, 2➔1.

For 3 layers composites, the relationship between the normalized energy release rate and the normalized stiffener thickness is shown in Fig. 5-5, where for 3 layers composite the energy release rate was calculated by Eq. 16 with $t_2=0$ and $t_3=0$. In Fig. 5-5, the result from the equation proposed by Hofinger [2], Eq. 17, is also shown.

$$G_c = \frac{M_b^2(1-\nu_{sub}^2)}{2E_{sub}}\left(\frac{1}{I_{sub}} - \frac{1}{I_{com}}\right) \qquad \text{Eq, 17 [2]}$$

with

$$I_{sub} = \frac{t_{sub}^3}{12},$$

$$I_{com} = \frac{t_{sub}^3}{3} + \kappa\frac{t_{coat}^3}{3} + \mu\left(\frac{t_{stif}^3}{3} + t_{stif}^2 t_{coat} + t_{coat}^2 t_{stif}\right) - \frac{\left\{t_{sub}^2 - \kappa t_{coat}^2 - \mu(t_{stif}^2 + 2t_{coat}t_{stif})\right\}^2}{4(t_{sub} + \kappa t_{coat} + \mu t_{stif})}$$

$$\kappa = \frac{E_{coat}(1-\nu_{sub}^2)}{E_{sub}(1-\nu_{coat}^2)},\ \mu = \frac{E_{stif}(1-\nu_{sub}^2)}{E_{sub}(1-\nu_{stif}^2)}$$

where, M_b is the bending moment per unit width (Eq. 3), E and ν are Young's modulus and Poison's ratio, t is thickness of layer, while the subscripts, sub, coat and stif indicate substrate, coating and stiffener, respectively. From Fig. 5-5, the results from Eq. 16 were same to the results reported by Hofinger.

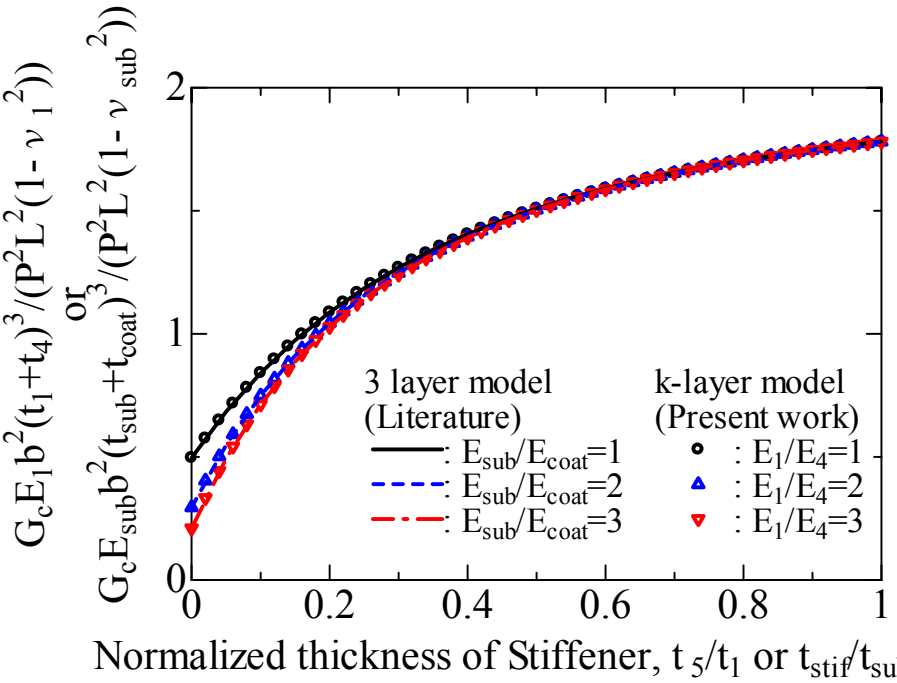

Fig. 5-5 The relationship between normalized energy release rate and the normalized stiffener thickness; $E_1=E_5$, $E_{sub}=E_{sitf}$, $t_4/t_1=t_{coat}/t_{sub}$=0.1, all of Poison ratio were 0.3.

For TBC specimens, i.e., for 5-layers composite, the energy release rate calculated by Eq. 16 is shown in Fig. 5-6, compared with that calculated by Hofinger's equation (Eq. 17). The results were calculated by using the actual material constants listed in Table 5-1, in the case of t_3=0, and

$E_{sub}=(t_1E_1+ t_2E_2)/(t_1+t_2)$ (mixture law), $E_{coat}=E_4$, $E_{stif}=E_5$,

$\nu_{sub}=\nu_1$, $\nu_{coat}=\nu_4$, $\nu_{stiff}=\nu_5$, $t_{sub}=(t_1+t_2)$, $t_{coat}=t_4$, $t_{stiff}=t_5$

for calculating by Eq. 17. From Fig. 5-6, the difference of the energy release rates calculated increased by increasing the critical load of delamination P_c. These results indicate that for TBC specimens the energy release rate must be calculated by Eq. 16, in other words, the bond coating can't be neglected even if the mixture law was considered.

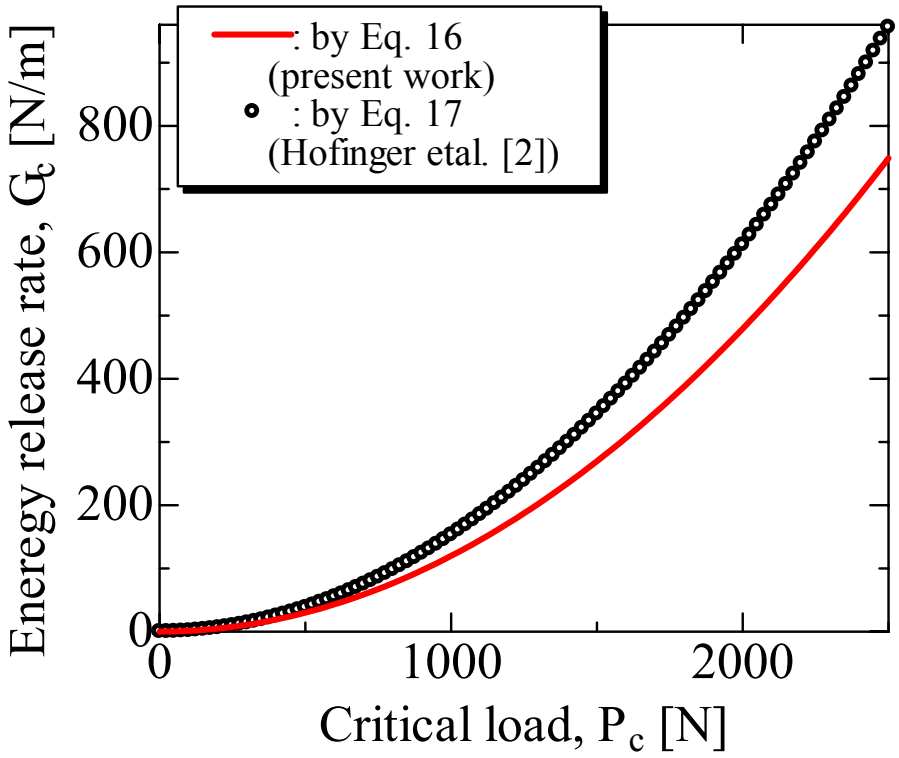

Fig. 5-6 Relationship between energy release rate and critical load calculated by Eq. 16 and Eq. 17.

5.3 Results and Discussion of Analytical Calculation

The specimen geometry of present work is shown in Fig. 5-6 and the material constants of each layer were listed in Table 5-1.

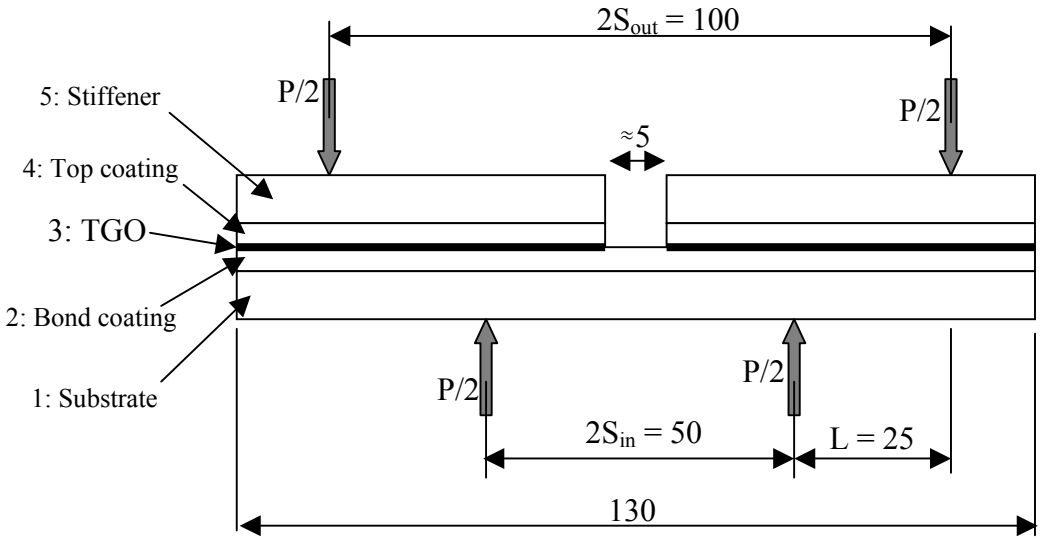

Fig. 5-6 Specimen geometry in present work, specimen width, b =10 (unit in mm).

Table 5-1 Material constants and thickness of each layer.

		material	E_i [GPa]	ν_i	t_i [mm]	b [mm]
1	Substrate	CMSX-4	135.3	0.3	5.0	10
2	Bond coat	LCO22	183	0.3	0.36	
3	TGO		310	0.3	0 - 7	
4	Top coat	8YSZ	50	0.3	0.34	
5	Stiffener	Steel	205	0.3	4.2	

The bending moment per unit width, which was applied at inner span area, M_b, was

$$M_b = \frac{M}{b} = \frac{PL}{2b}$$

The effects of the following parameters on the energy release rate by means of four point bending tests were studied and evaluated by using Eq. 16:

a) Young's modulus of top coating and thickness of the stiffener
b) Young's modulus and thickness of the TGO layer
c) Young's modulus of the bond coating
d) The location where the delamination occurs

The results of calculation were shown as follows.

a) Effects of Young's modulus of top coating and thickness of the stiffener

The effect of the thickness of the stiffener on the energy release rate is shown in Fig. 5-7. In this figure, the horizontal indicates the thickness of the stiffener normalized by that of substrate t_5/t_1, while the vertical axis shows the normalized energy release rate,

$$G_c E_1^* b^2 t_1^3 / (P^2 L^2)$$

where G_c is energy release rate, $E^*_1=E_1/(1-\nu_1^2)$, E_1 is the Young's modulus of the substrate, b is the width of the specimen, t_1 and t_5 are the thickness of the substrate and stiffener, P is the applied load, $L=S_{out}-S_{in}$ (see Fig. 5-7), respectively. In this figure, the energy release rate increased with the stiffener thickness. However the increasing rate of the energy release rate decreased with the increasing of the stiffener thickness.

The result for the Young's modulus of 50 GPa as the as-sprayed condition, is shown in Fig. 5-7, compared with those for two or five times higher Young's moduli. From these results, the energy release rate depends on the Young's modulus of the top coating if the thickness of the stiffener is relatively thin. However, it was independent of the stiffener thickness if the normalized stiffener thickness is larger than almost 0.6. In the present work, the value of the normalized stiffener thickness was 0.84. Therefore, in the present work, the effect on the energy release rate can be neglected even if Young's modulus of the top coating is changed during thermal oxidation exposure.

b) Effects of Young's modulus and thickness of the TGO layer

Fig. 5-8 shows the relationship between the normalized energy release rate and the normalized TGO thickness for the case that the Young's modulus of the TGO was the original value (310GPa) and for the case of two to five times higher values. The normalized energy release rate decreased with increasing not only of the TGO thickness but also of Young's modulus of the TGO.

Fig. 5-9 shows the changing rate of the energy release rate as a function of the normalized thickness and Young's modulus of the TGO. In Fig. 5-9, the energy release rate was changed less than 5% if the thickness and Young's modulus were 2 times higher than those of the present work. Therefore, the effect of thickness and Yong's modulus of TGO can be neglected in the present work.

c) Effect of Young's modulus of the bond coating

The Effect of the Young's modulus of the bond coating on the energy release rate is shown in Fig. 5-10. In Fig. 5-10, the energy release rate was changed less than 5% if the Young's modulus of bond coating was changed 20%. In the present work, it can be considered that the effect of the Young's modulus of the bond coating is neglected, because the bond coating is stable and the mechanical properties of it don't change during oxidation exposure. However if the Young's modulus of the bond coating is changed more than 20%, the effect of it becomes large and can't be neglected.

d) Effect of the location where the delamination occurs

If the delamination occurs at interface between bond coating and TGO, the changing rate of the energy release rate is shown in Fig. 5-11. For comparison, the results for delamination at TGO/top-coating interface are also shown in this figure. From Fig. 5-11, the energy release rate changed only slightly for delamination at the bond-coating/TGO interface compared with that for delamination at the TGO/top-coating. Therefore the influence of the delamination site on the energy release rate can be neglected in the present work.

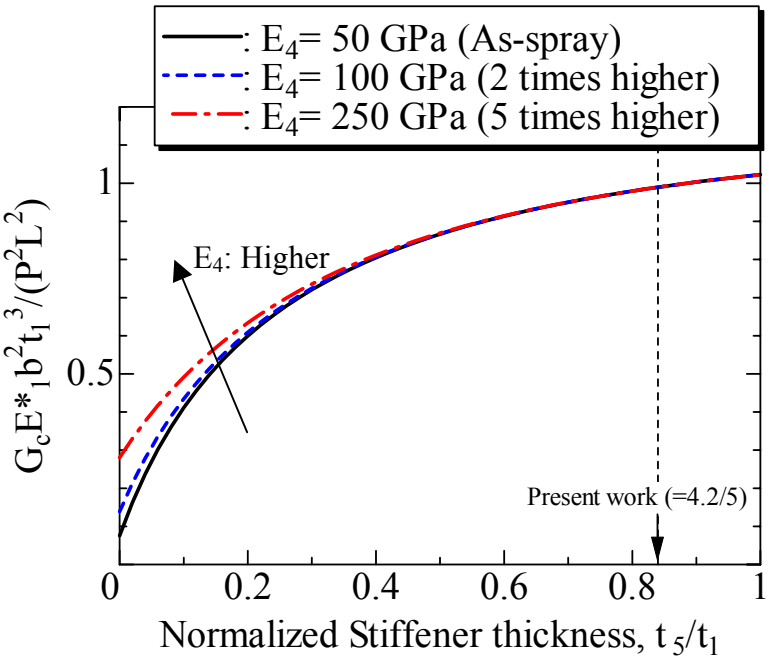

Fig. 5-7 The effect of the Young's modulus of top coating and thickness of the stiffener on the energy release rate.

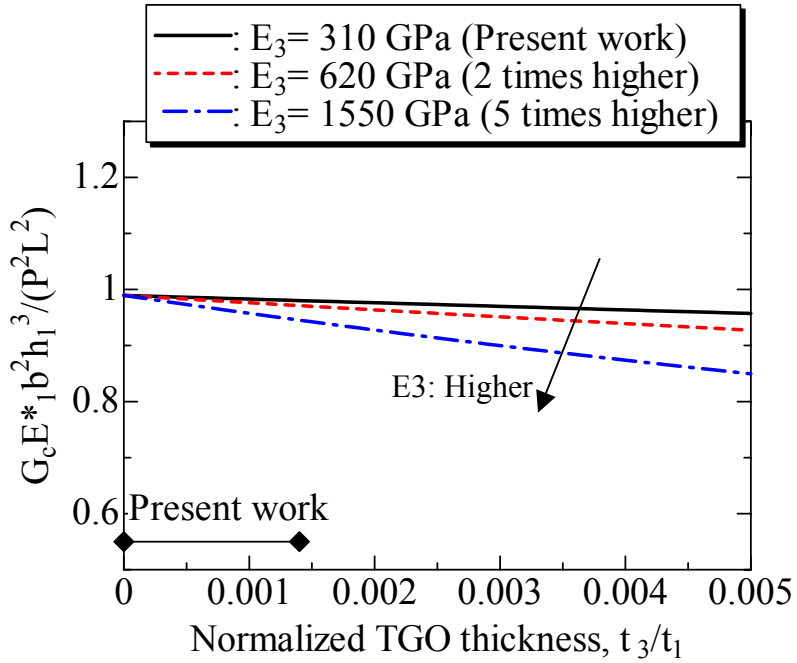

Fig. 5-8 The effect of the Young's modulus and thickness of TGO on the energy release rate.

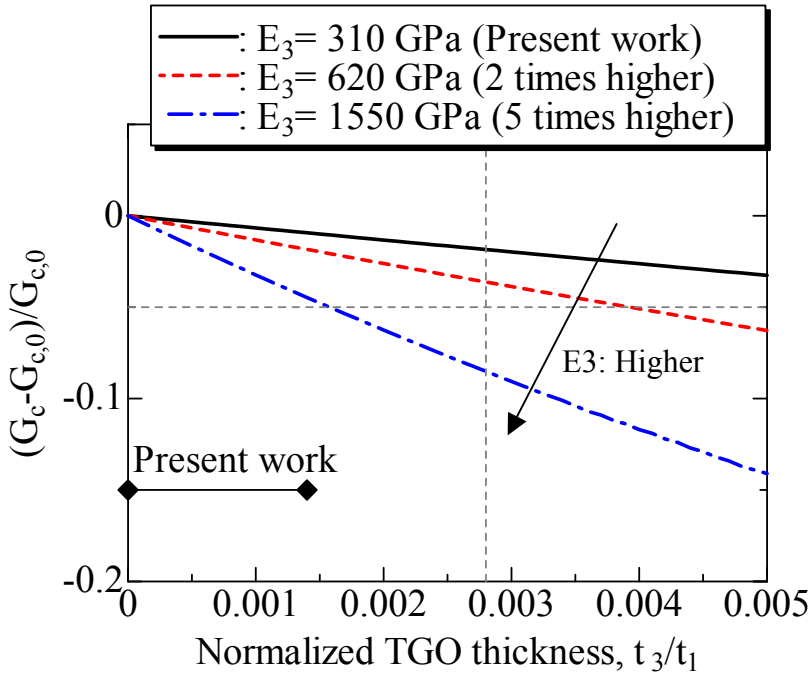

* $G_{c,0}$: Energy release rate without TGO

Fig. 5-9 The change of the energy release rate with Young's modulus and thickness of TGO.

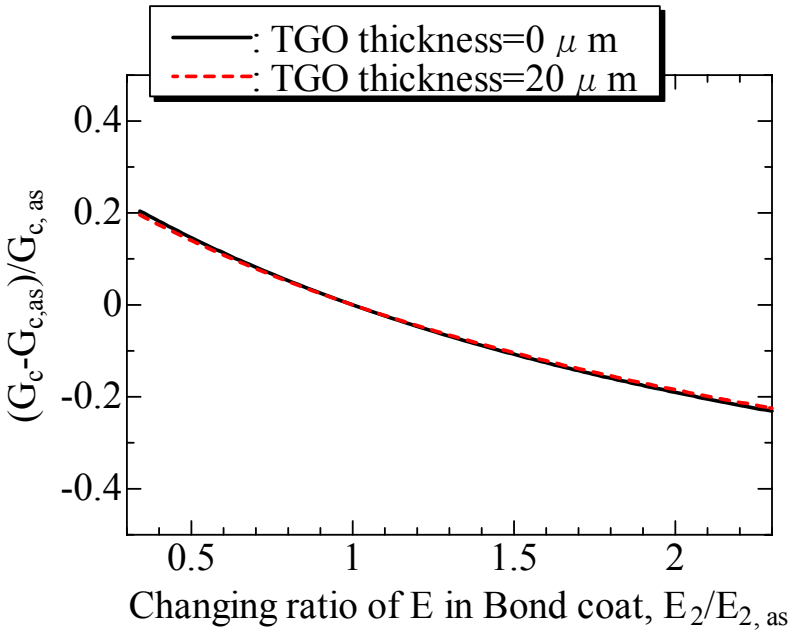

* $G_{c,as}$: Energy release rate at E_2=183 GPa

Fig. 5-10 Effect of Young's modulus of bond coating on the energy release rate.

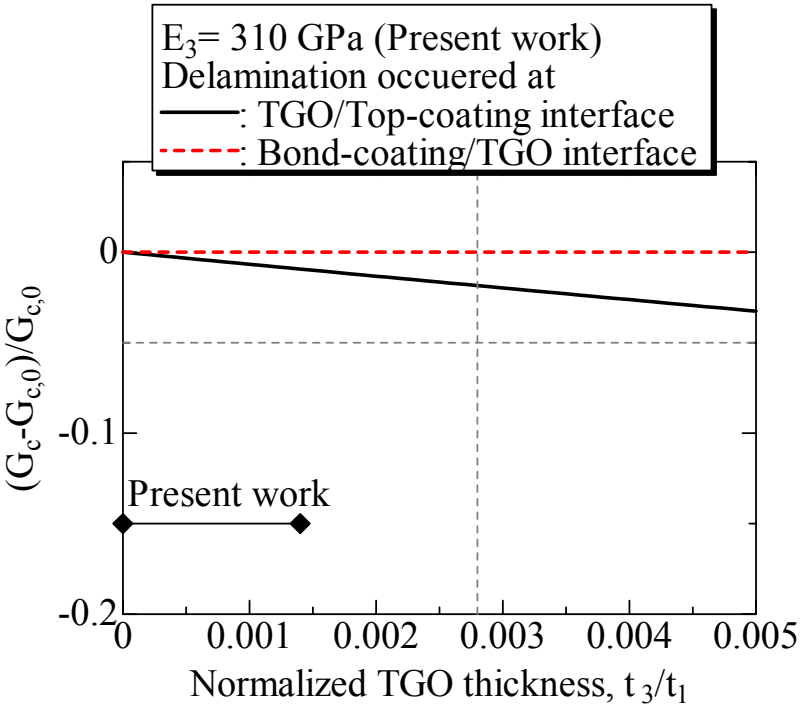

* $G_{c,0}$: Energy release rate without TGO

Fig. 5-11 Effect of the delamination location on the energy release rate.

6. Experimental Procedure

6.1 Procedure of Bonding the Stiffener to the Top Coat

In this work, in order to prevent the vertical crack in top coat, namely to inhibit the segmentation of top coat, the stiffener was bonded on the top coat by means of the adhesive. The requirements of the adhesive are as follows;

a) high bonding strength of the adhesive compared with delamination strength of TBC.
b) it can be distributed uniformly
c) easy handling.
d) it must not infiltrate into TC up to TC/BC interface (infiltration thickness must be less than a half of TC thickness (150μm)).
e) it can be used at high temperature (1000˚C)

However, there is no adhesive satisfying requirement e). Therefore, the test couldn't be performed at elevated temperature.

The heat curing type epoxy adhesive, Araldite AT1 (CIBA-GEIGY Ltd.), satisfied the above requirements except e); because the bonding strength is greater than 70 MPa, it is a powder type adhesive so handling is easy and uniform distribution is can be realized easily, the infiltration thickness was less than 150μm (see section 7). Therefore Araldite AT1 was used in the present work for bonding of the stiffener.

The heating furnace (Heraeus Instruments), as shown in Fig. 6-1, was used for curing of the adhesive. A schematic illustration of the heating cycle for curing is shown in Fig. 6-2. When the stiffener was bonded to the specimen, a fixation jig was used. The photograph and the drafting of it are Fig. 6-3 and 6-4, respectively.

The bonding procedure was summarized as follows;

1. Remove the oil and dirt form the stiffener with alcohol.
2. Put the AT1 powder on the stiffener.
3. Put the stiffener on the fixation jig.
4. Put the specimen on the stiffener and fix stiffener and specimen with the fixation jig.
5. Put the specimens set into the furnace and put the dead weight on the specimens.

*** The detail of the above preparation method and the powder amount were shown in Fig. 6-5**

6. Hold at 180˚C for 2 hr (Fig. 6-2). Note that the limits for the upper and lower temperature are 200˚C and 160˚C, respectivly.
7. Take the specimens out of the furnace.
8. Remove the specimen from the fixation jig.

Note: Araldite AT1 has no toxicity but be careful not to breathe it in from mouth and nose.

Fig. 6-1 The heating furnace for the curing of adhesive.

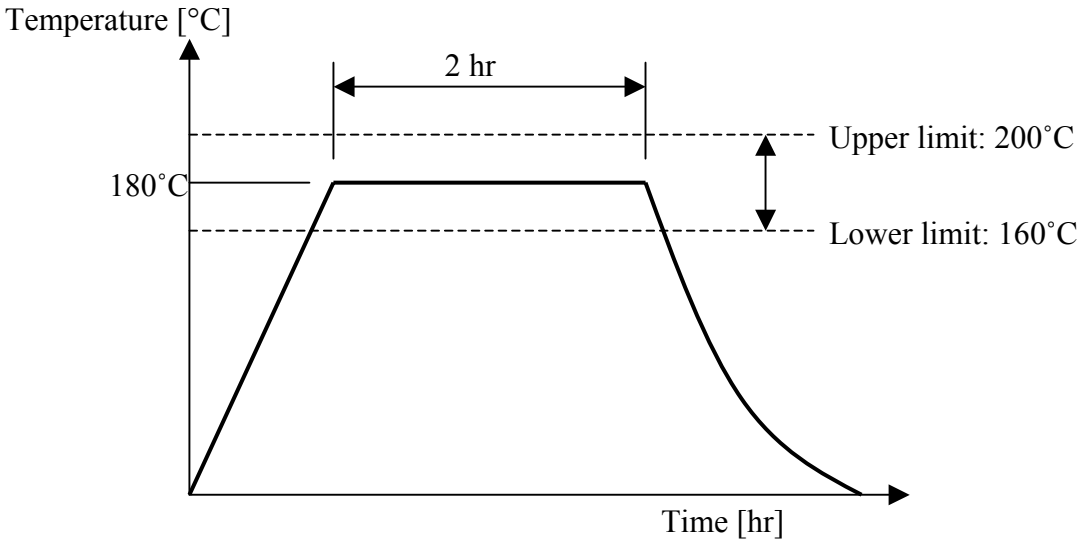

Fig. 6-2 Schematic illustration of the heating cycle for curing of adhesive, Araldite AT1.


Fig. 6-3 The fixation jig (top view).

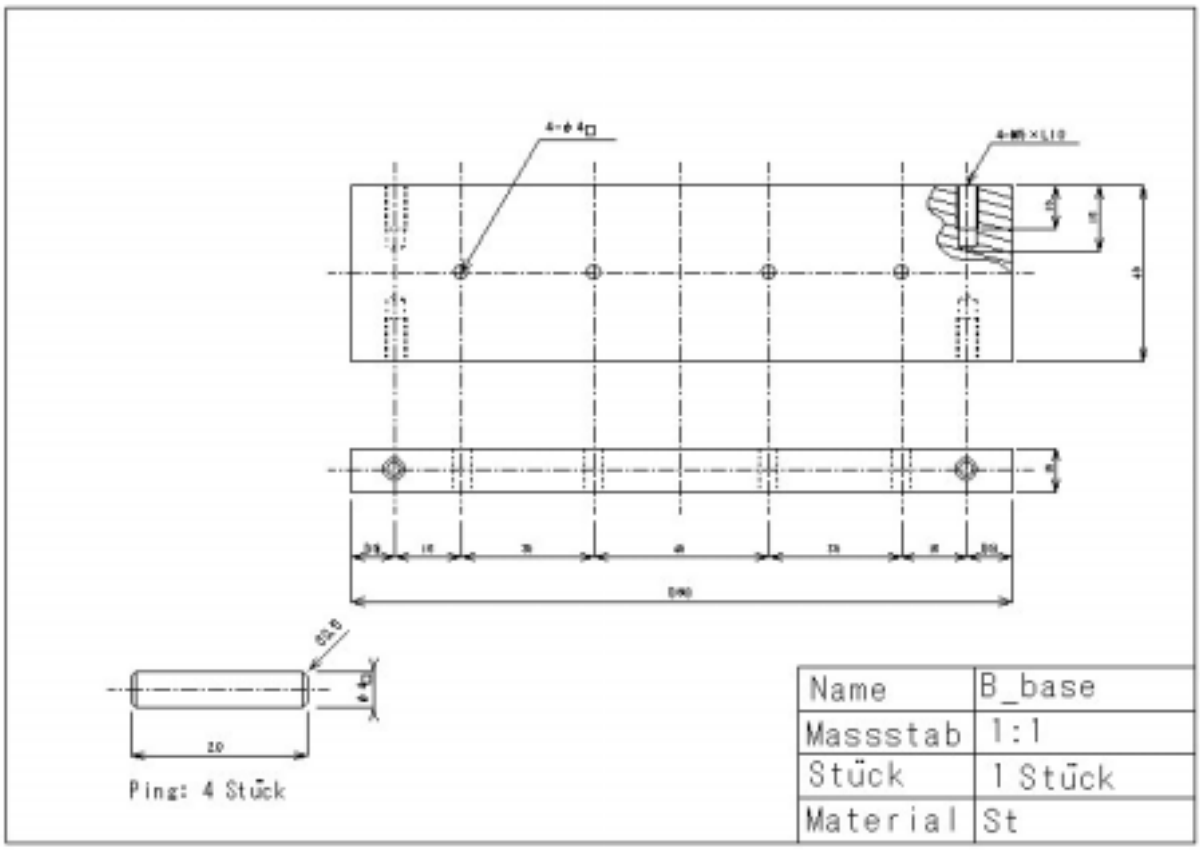

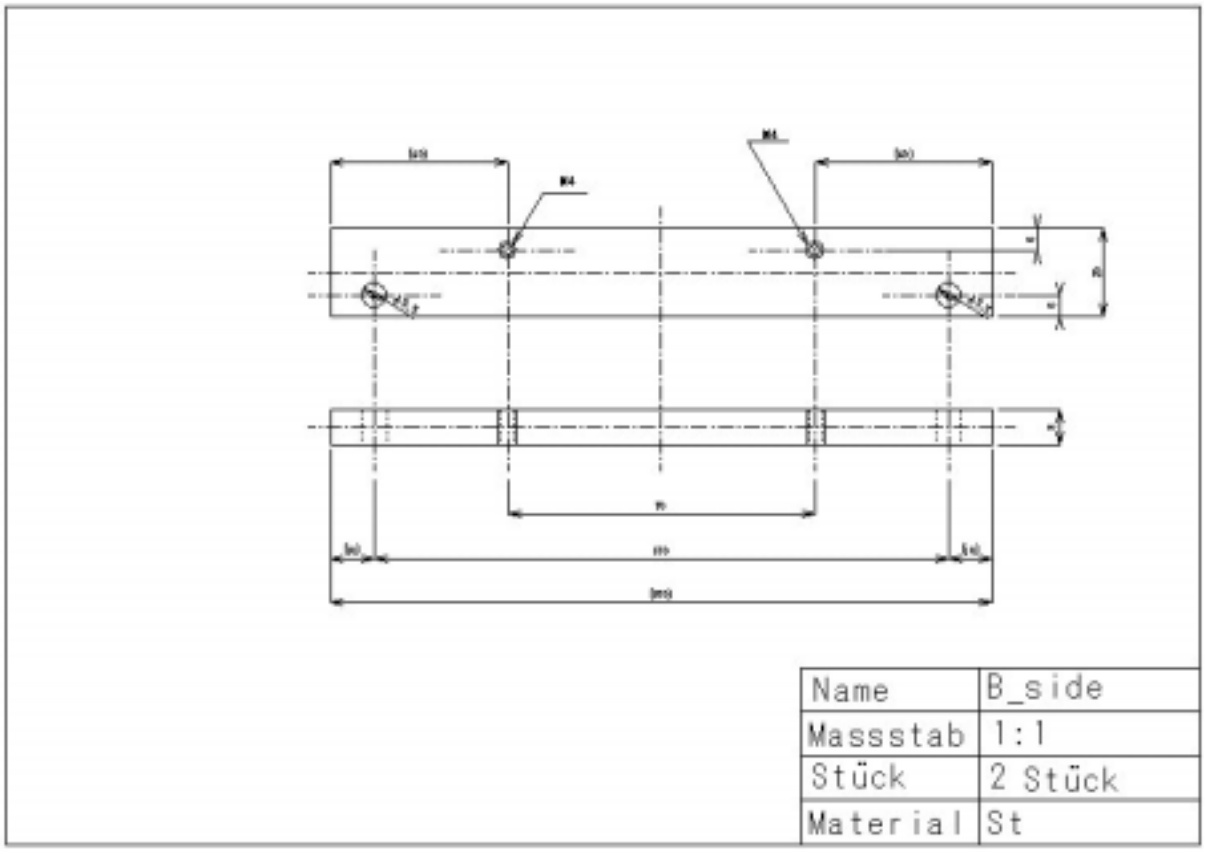

Fig. 6-4 Draftings of the jig for specimen fixation.

1. Put the powder on the edge of the stiffener (only one side).

2. Sprinkle powder uniformly.

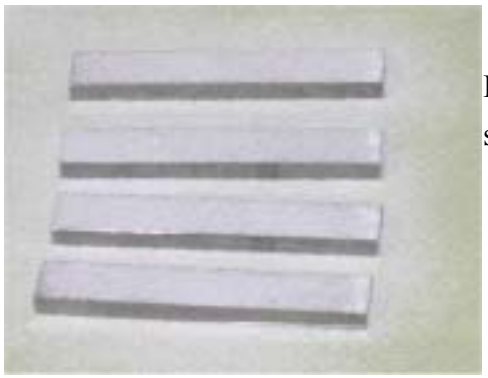

3. The amount of the powder (a lot of the powder on the edge A)

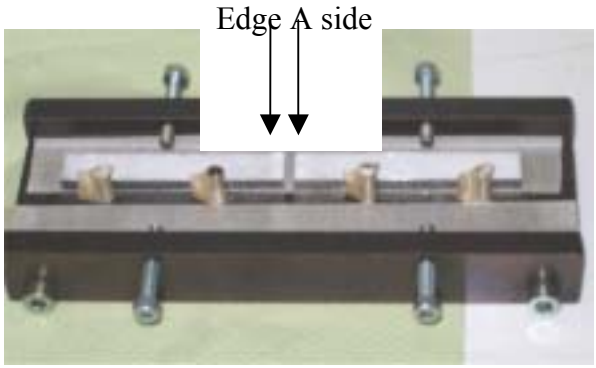

Distance betwee the stiffeners ≈ 5mm

4. Put the stiffeners on the fixation jig.

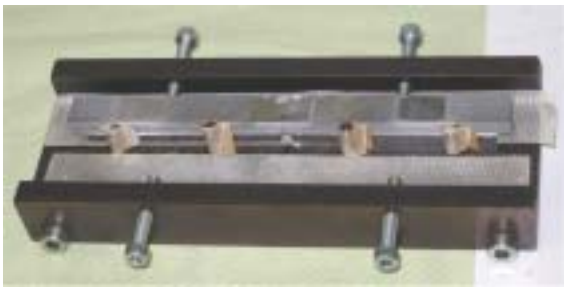

5. Put the specimen on the stiffener
(Top coating side : Downward)

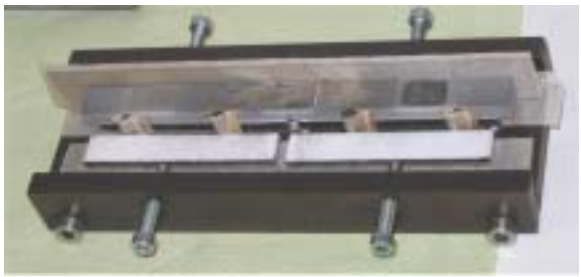

6. Fix the specimen with the screw, and set next specimen.

7. Over view after the preparation.

8. Put in the furnace ➔ put on the dead weight ➔ unscrew ➔ heating ➔ hold ➔ cooling

Fig. 6-5 The preparation method of the bonding and the amount of the AT1 powder on the stiffeners.

6.2 Procedure of Four Point Bending Test

The creep testing machine, as shown in Fig. 6-5, was used in the present work to apply the bending force. Fig. 6-6 and Fig. 6-7 show schematic illustration of the test system and the view of recording software. The piston of the creep testing machine (Fig. 6-5) can be moved at a constant speed of 7 mm/min.. The load cell with a capacity of 20kN and a Solartron extensometer were used in the present tests. The personal computer, HPC 32, was used for recoding the applied load and the deflection of the specimen. The software, so called FPOINT, was programmed for recoding the data (FPOINT was programmed by S. Linn).

The testing procedure (including usage of the recording software) was summarized as follows;

1. Set the upper parts of test rig (5)
2. Set the lower parts of test rig (6)
3. Warm up the Amplifier (8) (for 30 min.)
4. Adjust position by the lever switch (2)

   Note: Down the lever➔Cylinder moves up (Compressive)

   Up the lever➔Cylinder moves down (Tensile)
5. Insert specimen (4) (Note, Coating upwards)
6. Start software “FPOINT”
7. Set the extensometer (9), around 1 mm in displacement (indicator)
8. Click the button “Zero” (e) on the display to set zero displacement
9. Push “zero” button of the Load cell amplifier (8) to set zero load
10. Click the window of “Remote control” (d) (on the display)
11. Finally check the status of all the equipment
12. Click the button “Start” (a) to start recording
13. Apply the constant load, Turn up the lever (2)

    Note: Emergency stop➔ Push the button (3)
14. If the stiffness of the specimen is changed; turn the lever to neutral to stop testing
15. Click the button “Stop” (b) to stop recording
16. Click the button “Save” (c) to save the data
17. Remove the applied loading; Down the lever (2)

    Note: Don’t move the piston too far prevent damage of the test rig
18. Remove the specimen from the test rig
19. Click the “Clean memo” (f) and “Clean diagram”(g) button.
20. Click the “Close” (h) button
21. Clear everything
22. Check the roller of bending equipment

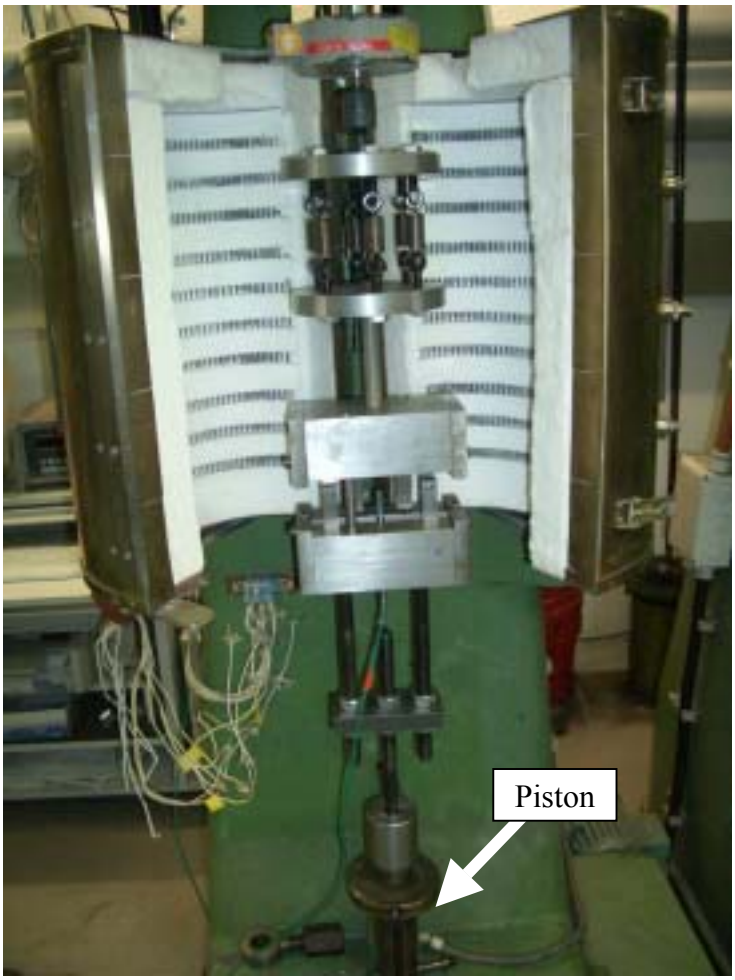

Fig. 6-5 The creep testing machine, EPM 40.

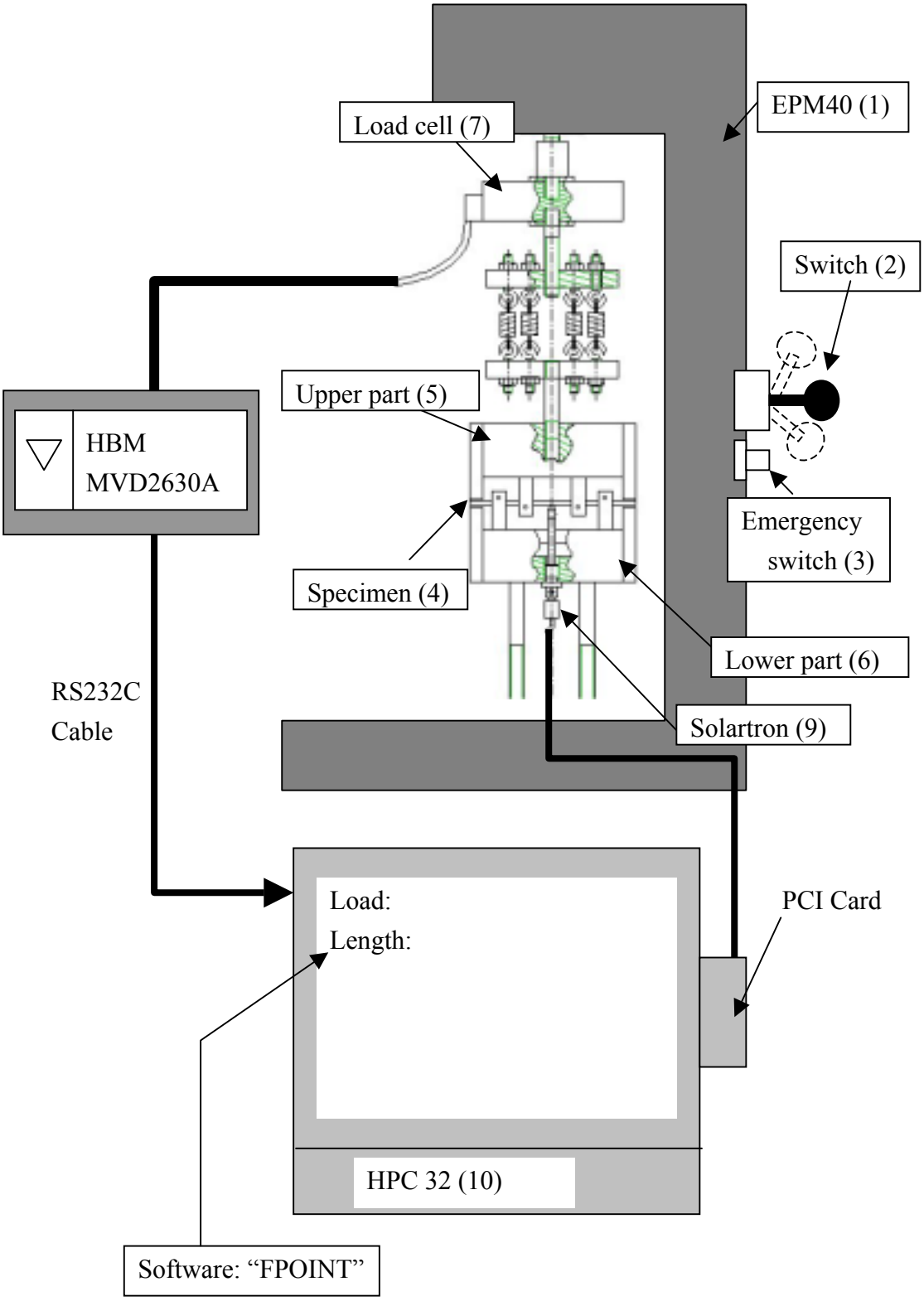

Fig. 6-6 Schematic illustration of test machine.

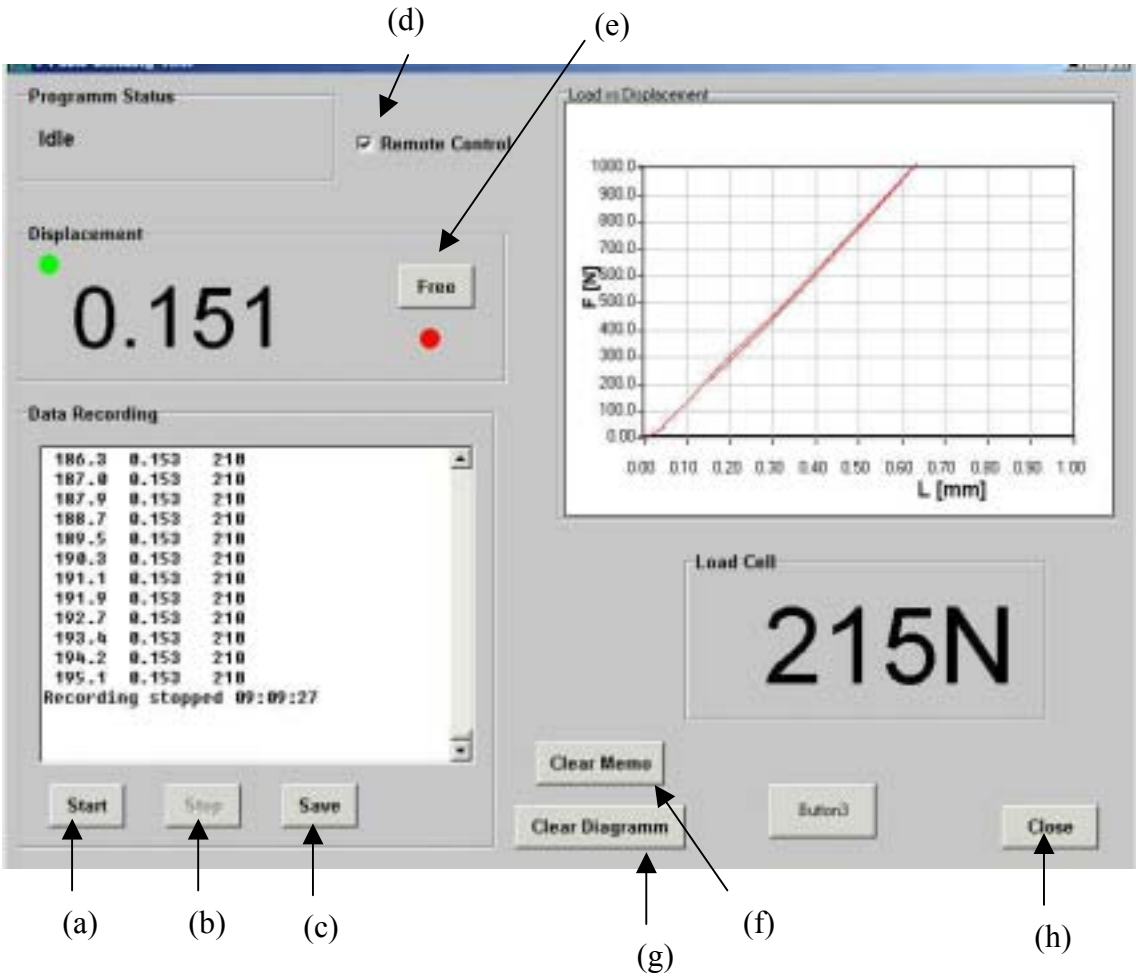

Fig. 6-7 View of FPOINT.

7. Establishment of bonding procedure and evaluation of infiltration depth of adhesive

By using dummy TBC specimens, the bonding conditions were confirmed and the infiltration depth of adhesive into the top coat was also measured. The procedure of preparation and observation was as follows:

i) The steel stiffener, with a size of 50 mm in length and 10 mm width and 4.2 mm in thickness, was bonded to the ceramic coat of the 8YSZ air plasma sprayed on steel specimen, with a size of 50 mm in length and 10 mm width and 5 mm in thickness, by means of above bonding procedures (see Section 6.1).

ii) The bonded TBC/steel specimen was cut across the bonding interface and the cross section was polished.

iii) The morphology of the bonding condition was observed by metal microscope and the depth of the infiltration of the adhesive was measured by means of SEM (EDX analysis).

Typical optical photographs of the cross section of the bonded TBC/steel specimen are shown in Fig. 8-1. In this figure, the thickness of the adhesive was approximately 0.1mm, which equals to recommendation thickness of the adhesive. In addition, pores in the adhesive layer can be observed. The pore ratio in the adhesive layer was almost 30% however this can be permitted because the bonding strength of the adhesion is higher than delamination strength of the TBC.

The microstructure of the TC after bonding was observed by means of SEM and typical results are shown in Fig. 8-2, Fig. 8-3 and Fig. 8-4. From backscattered electron (BE) images shown in Fig. 8-2, the infiltration depth of the adhesive can't be measured because it can’t be decided precisely if the pore is filled with adhesive or not. However, it can be observed in the secondary electron (SE) images shown in Fig. 8-3 and Fig. 8-4 that the pores near the TC/AT1 interface was filled. The results of the EDX analysis are shown in Fig. 8-5. Peaks of carbon and oxygen were found in the filled pores. Because AT1 consists of carbon and oxygen, these pores were filled with adhesive. In particular, the oxygen peaks can be found in the portion of approximately 100μm from TC/AT1 interface, but there is no evidence of oxygen deeper than 100μm. Thereby it can be concluded that the adhesive infiltrated approximately 100μm in depth into TC (less than 150μm) and the influence of the infiltration on the energy release rate by delamination can be neglected.

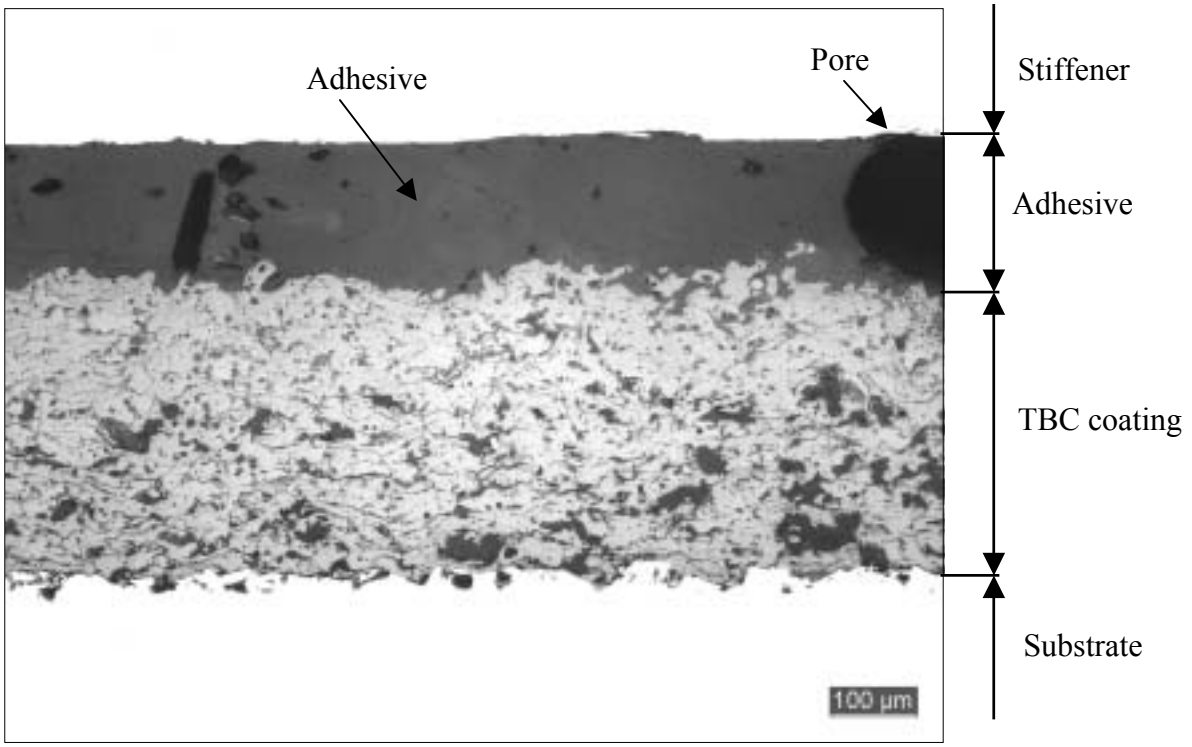

(a)

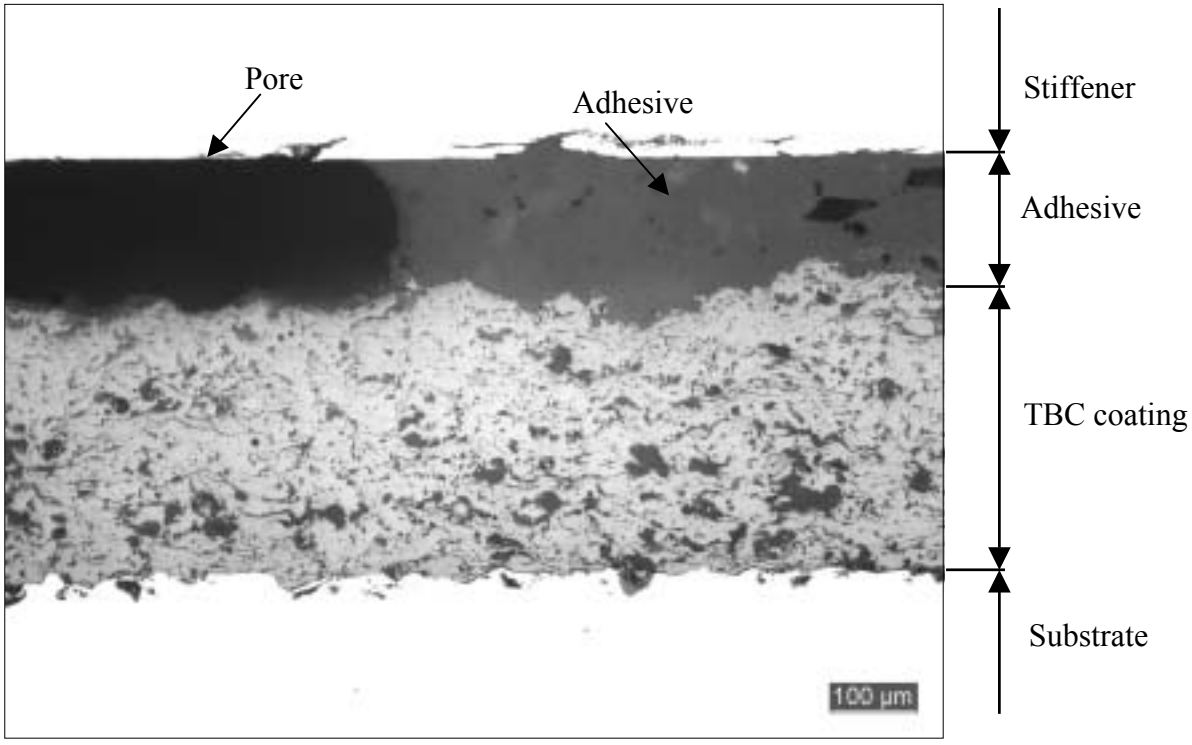

(b)

Fig. 8-1 Microphotograph of the cross section of bonded TBC/Stiffener dummy specimens.

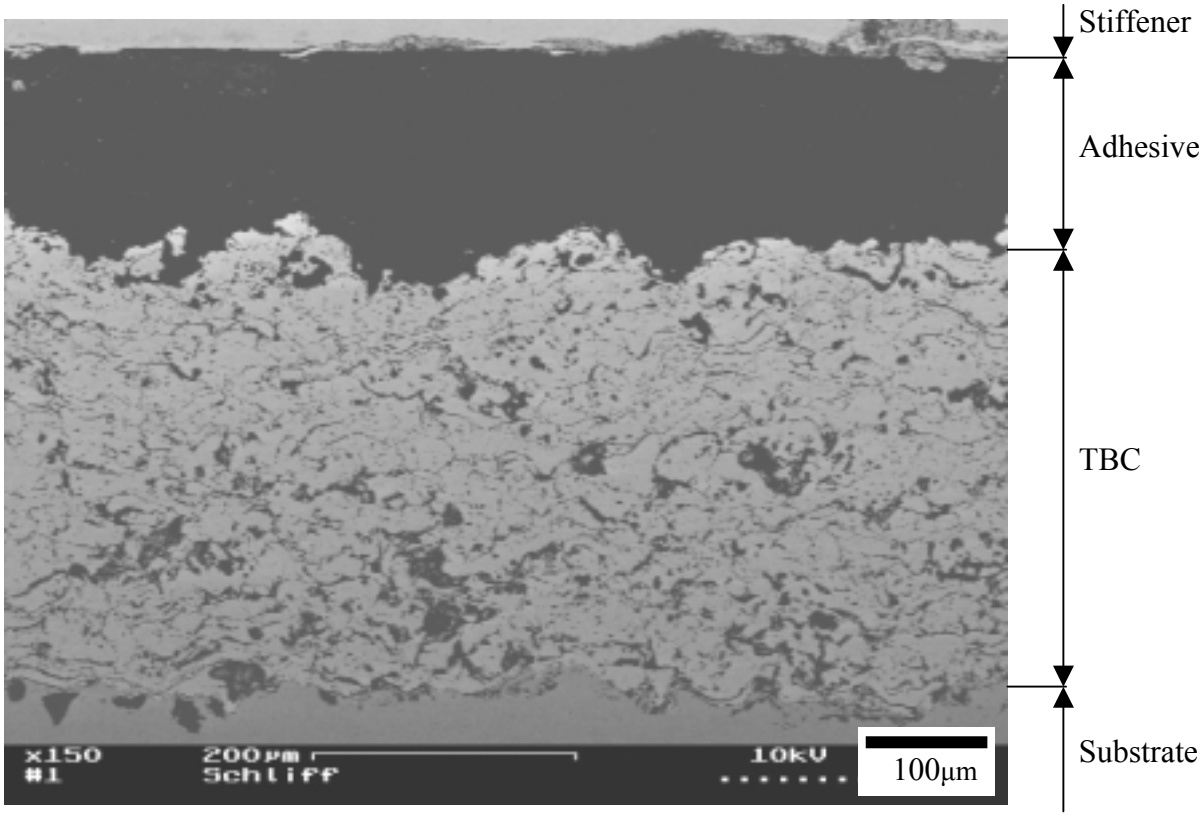

(a)

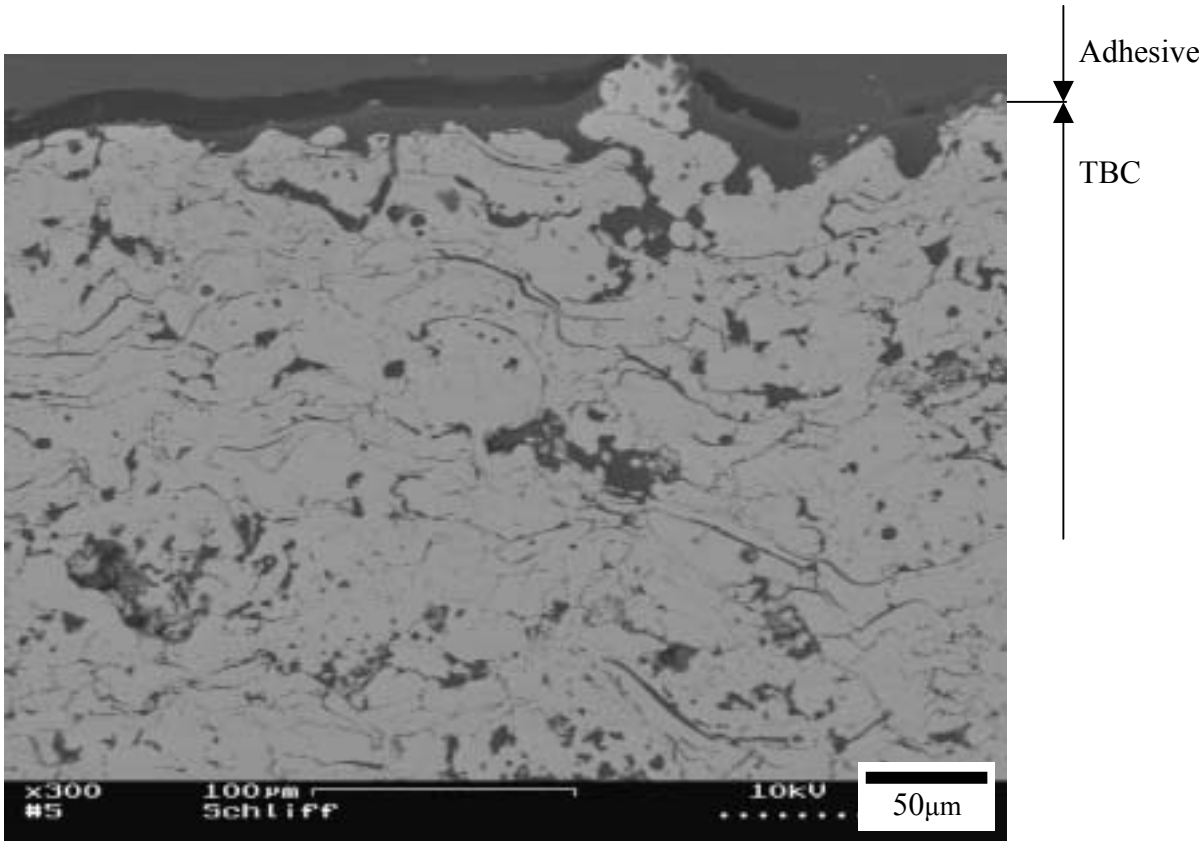

(b)

Fig. 8-2 BE images of the cross sections of the bonded TBC/Stiffener specimens.

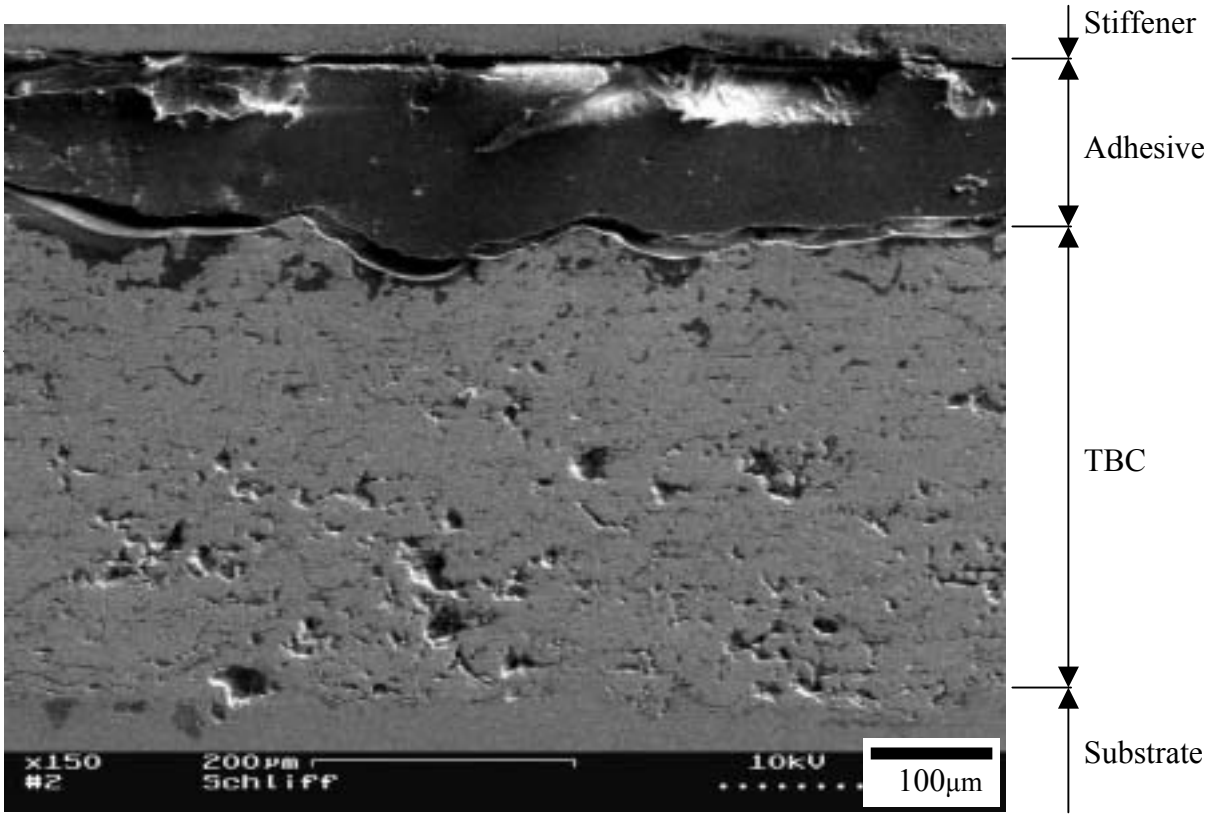

(a)

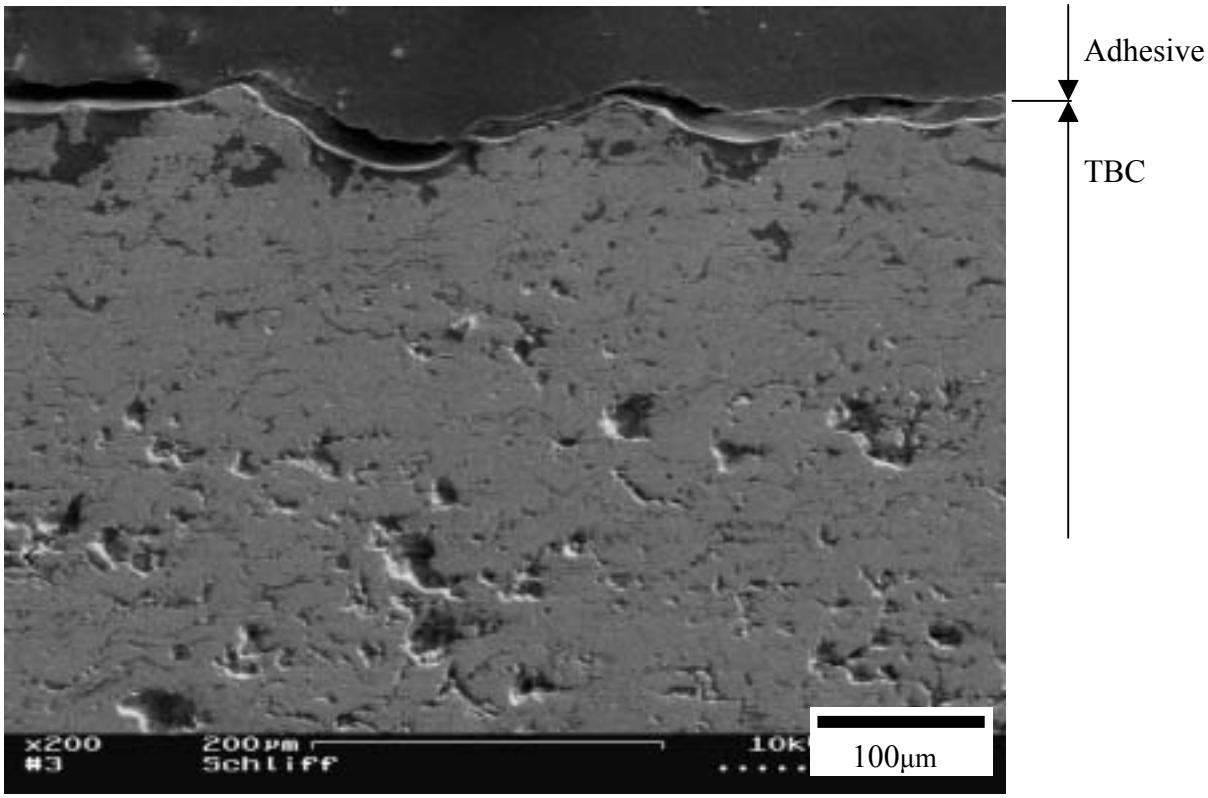

(b)

Fig. 8-3 SE image of the cross sections of the bonded TBC/Stiffener specimens.

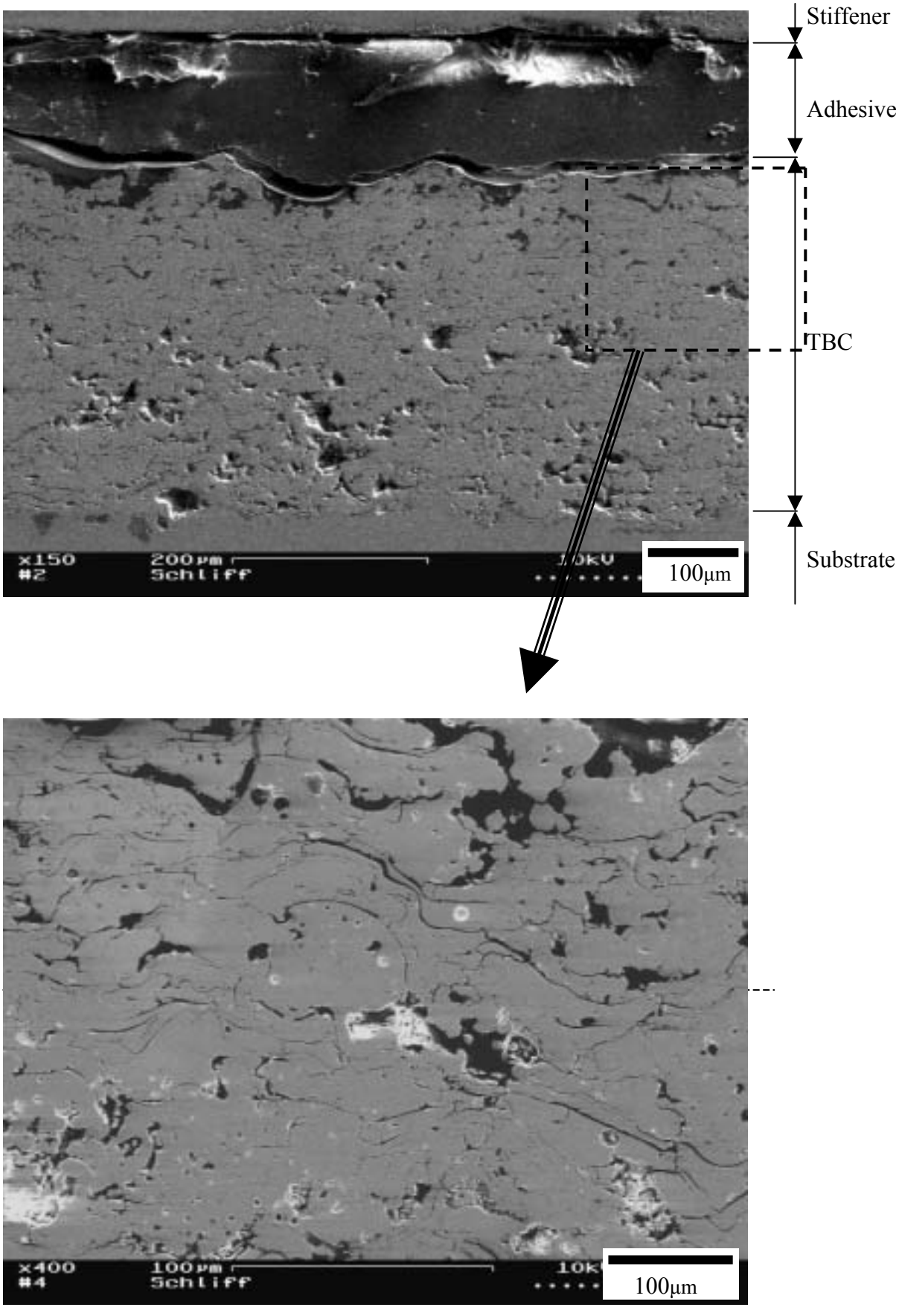

Fig. 8-4 Enraged SE image around infiltration region of the adhesive into the TBC coating.

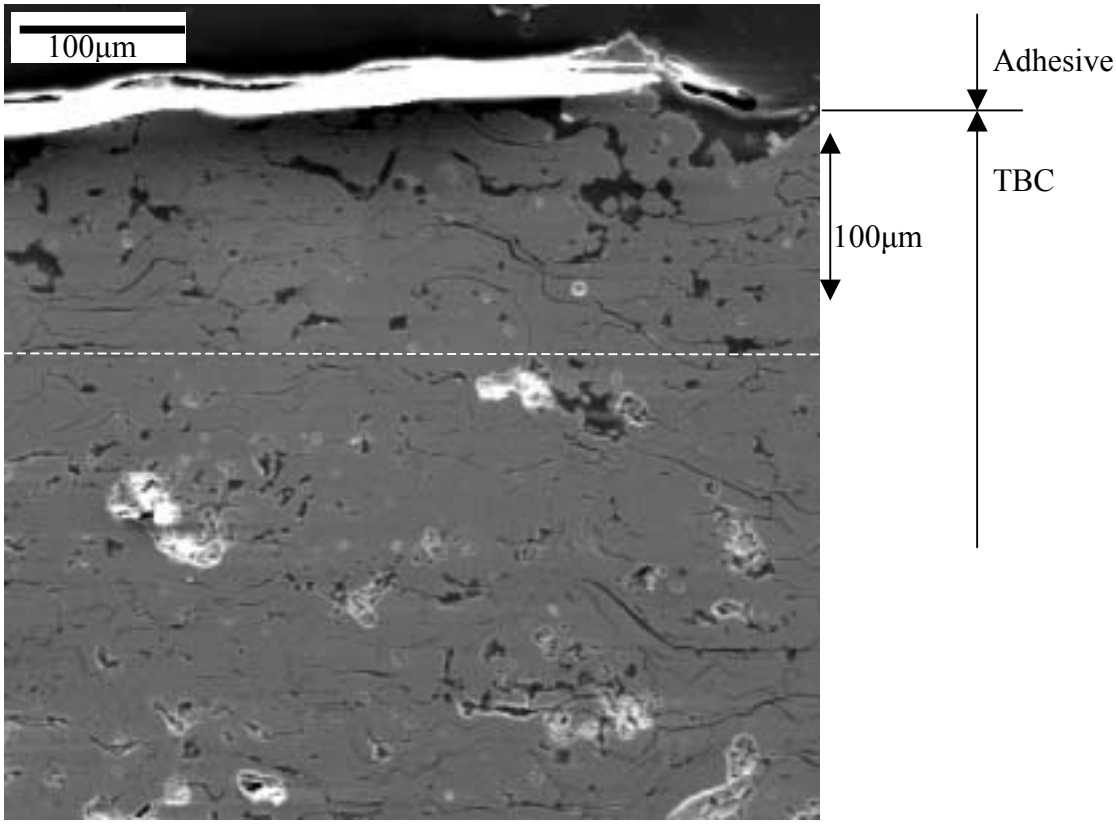

(a) SE image

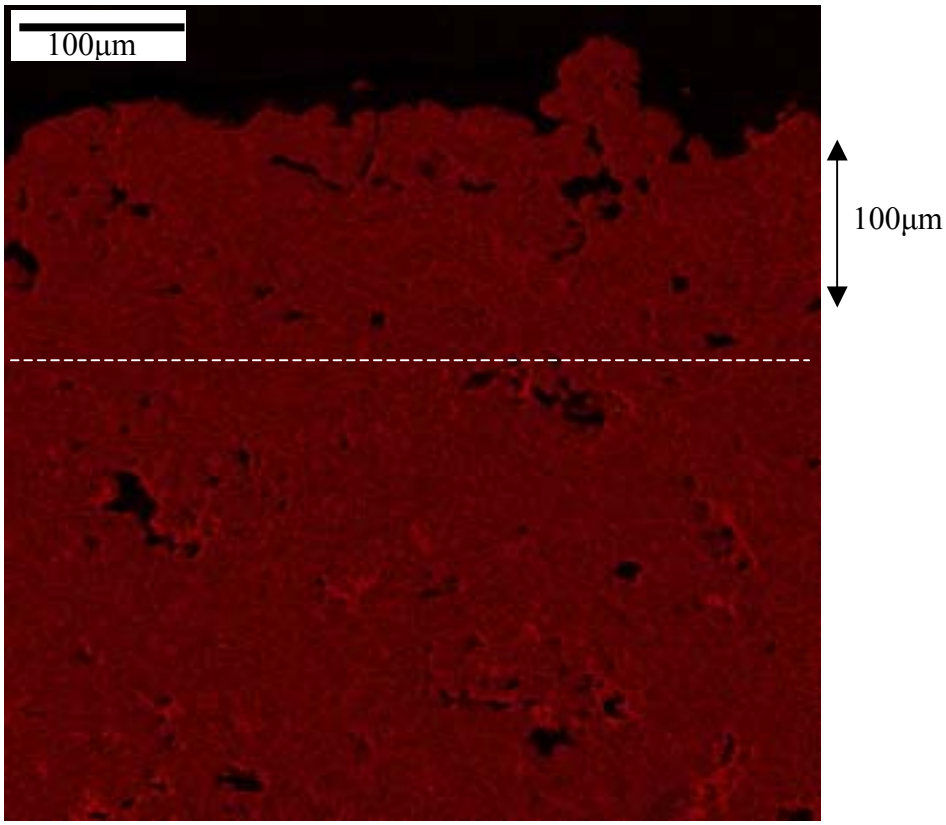

(b) Zr map

Fig. 8-5 EDX analysis results of the bonded TBC/Stiffener specimens.

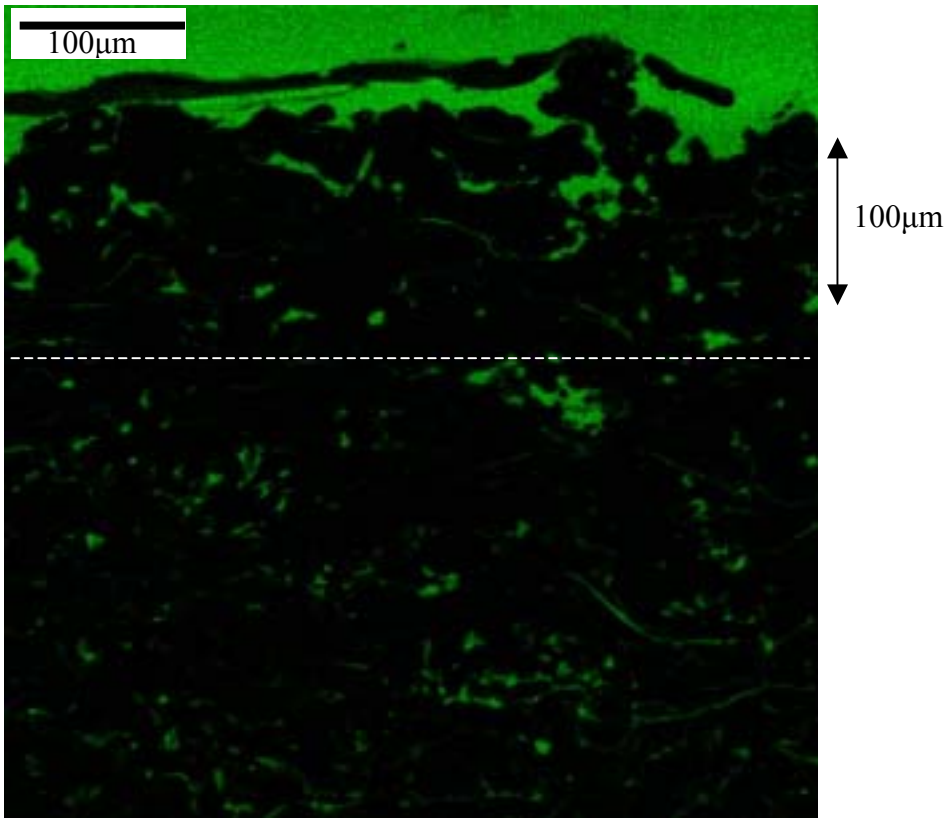

(c) C map

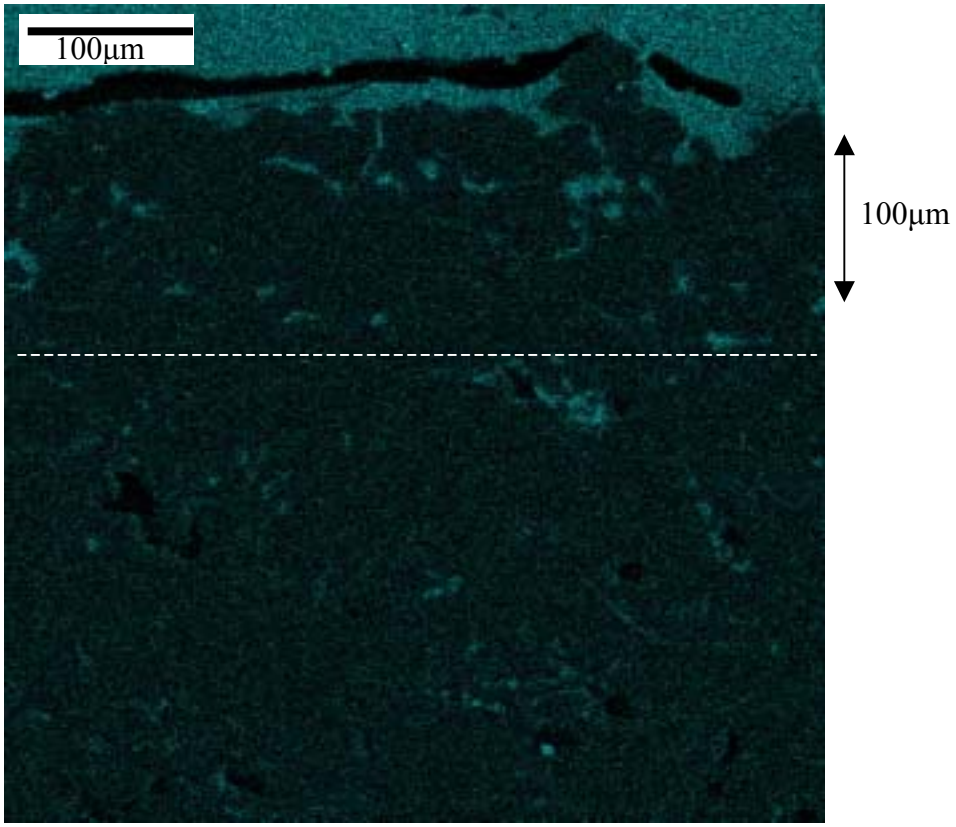

(d) O map

Fig. 8-5 EDX analysis results of the bonded TBC/Stiffener specimens (continued).

8. Confirmation of Reproducibility by using Dummy specimens

Before the testing of TBC specimens pre-tests were performed by using steel specimens with the size of approximately 130 mm in length, 11.9 mm in width and 4.85 mm in thickness. The typical load-time curves during loading and unloading tests by using steel specimens are shown in Fig. 7-1. The loading and unloading rates were approximately 5.3 N/sec (see section 2). Due to the spring properties ($P_{initial}$ =50 N, see section 3.1), the applied load rapidly to 220 or 230 N. The typical load - deflection curve during bending tests by using steel specimen is shown in Fig. 7-2. From the bending theory for thin bars, the relationship between load, P, and deflection, δ, was;

$$P = \frac{12EI}{(6S_{in}L^2 + 3L^3 + 2S_{in}^3)} \times \delta = 1619[N/mm] \times \delta$$

where, E is the Young's modulus, E=205 GPa, I is the second moment of area, $I=bh^3/12$, b and h are width and thickness of the specimen, $L=S_{out}-S_{in}$, S_{in} and S_{out} are inner and outer half span of the four point bending device, respectively. In order to compare, the theoretical load-deflection curve is also shown in Fig. 7-2. The slope of the load-deflection curves during loading and unloading tests are summarized in Table 7-1 compared with the theoretical slope. It can be observed from Fig. 7-2 and Table 7-1 that in the experiment the relationship between load and deflection corresponds well with the theoretical one. The difference between experimental slope and the theoretical one was less than 5% (Table 7-1). In addition, the bending tests can be performed with great reproducibility. The difference of slope in each test was less than 3% and the standard deviation of the slope was approximately 16.5 N/mm, which was 1% of the slope.

From these results, it can be concluded that the bending tests with this equipment can be performed with great accuracy and great reproducibility.

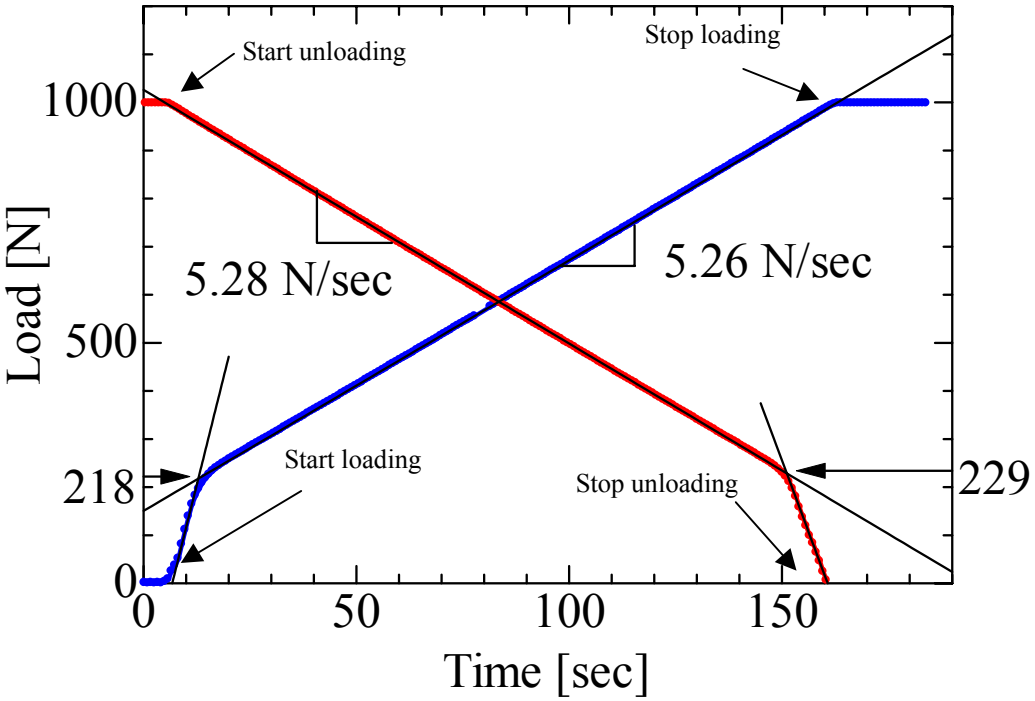

Fig. 7-1 Typical load –time curves during loading and unloading test by using steel specimens.

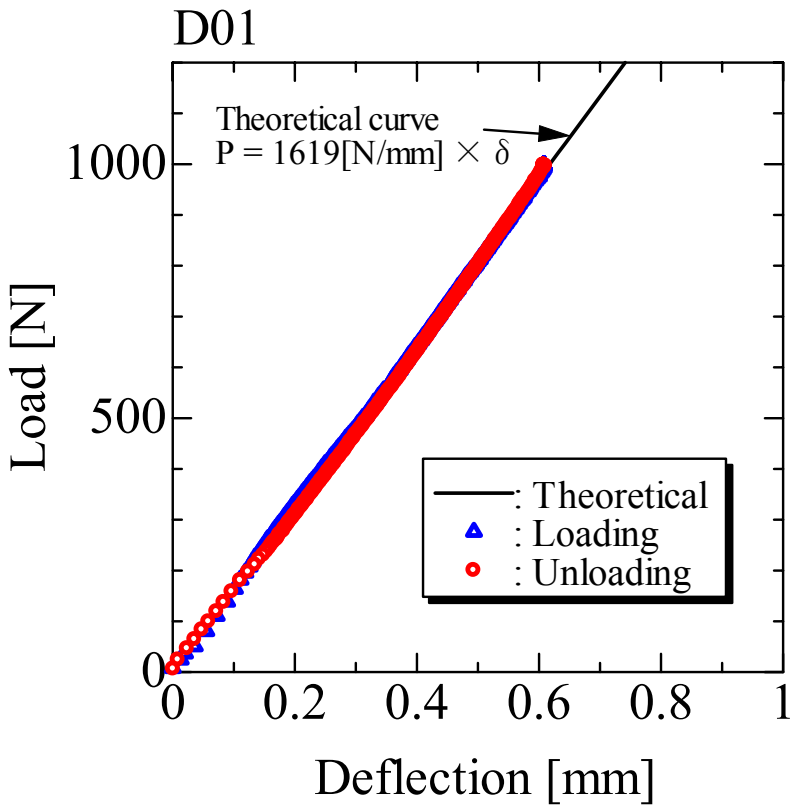

Fig. 7-2 Typical load-deflection curves during bending tests by using steel specimens.

Table 7-1 The slopes of the load-deflection curve in the dummy tests using steel specimen.

Specimen No.		Slope of curve in the test [N/mm]		Theoretical value of the slope [N/mm]	Error* [%]	
		Loading	Unloading		Loading	Unloading
D01		1627	1664	1619	0.45	2.74
D02	1	1665	1681	1619	2.83	3.79
	2	1640	1673	1619	1.28	3.34
	3	1664	1687	1619	2.75	4.19
	4	1646	1664	1619	1.68	2.79
D03	1	1636	1645	1619	1.03	1.58
	2	1643	1668	1619	1.46	3.01
	3	1628	1650	1619	0.56	1.89
D04		1667	1682	1619	2.94	3.87
D05		1670	1698	1619	3.12	4.84
Average		1649	1671	1619	1.81	3.82
Max.		1670	1698			
Min.		1627	1645			
Standard deviation		16.52	16.39			

* Error = (experimental slope - theoretical slope) / theoretical slope×100

9. Results and Discussions

A typical load – deflection curve during the 4-point bending test is shown in Fig. 9-1. In this figure, the analytical load – deflection curve which was calculated by Eq. 9-1 is also shown.

$$\delta=PL/\ (-L/3E_{c,5}I_{c,5}+(S_{out}-D)^2/\ E_{c,5}I_{c,5}+(2S_{out}D-D^2)/E_{c,3}I_{c,3})/4 \qquad \text{Eq. 9-1}$$

where, $E_{c,5}$ and $E_{c,3}$ are the Young's moduli without and with stiffener, $I_{c,5}$ and $I_{c,3}$ are the second moments of area without and with stiffener, P is the Load, S_{in} and S_{out} are the inner and outer half span, $L= S_{out} - S_{in}$, D is half of the distance between the stiffeners, respectively. In Fig. 9-1, the load – deflection curve consists of 6 stages. At stage I, the load – deflection curve of the specimen was linear. The experimental curve was equivalent to the analytical one. After the linear stage in the load – deflection curve, at stage II, the slope of the load - deflection curve decreased with increasing deflection. At stage IV the same behavior can be observed. The plateaus of the curve can be observed at stage III and at stage V. At stage VI, the deflection increased again in proportion to the load.

Photographs of delamination crack initiation and propagation during the test are shown in Fig. 9-2. For the shown specimen (C01), the crack initiated from the edge of the right side stiffener and propagated through the TC to the TC/BC interface. After the vertical crack propagated to the TC/BC interface, the crack propagated along the TC/BC interface, in other words, the delamination occurred. At left side, the same crack initiation and propagation process was observed. Note that the delamination didn't always occur on right side first, sometimes it occurred first on left side, or on both sides simultaneously. In other words, the delamination from either side occurred at random. These delamination processes correlated with each stage are also shown in Fig. 9-1 schematically. At stage II and stage IV, the vertical cracks were initiated at edge of stiffener and propagated through the TC to the TC/BC interface. In response to that, the deformation resistance of the specimen decreased. At stage III and stage V, the delamination crack propagated rapidly until the crack tip approached the inner loading lines. Accordingly, the plateaus of the curve were observed in the load – deflection curve. The energy release rate for delamination was calculated from the critical load value corresponding to these plateaus.

A typical deflection – time curve is shown in Fig. 9-3. The deflection rate of the specimen (in other words, the slope of the deflection – time curve) is also shown in Fig. 9-3. The peak deflection rate may correspond to the delamination crack growth rate. The influence of thermal aging on the deflection rate will be discussed later (Sec. 9-5).

Typical microphotographs of crack propagation path after the test are shown in Fig. 9-4. It is revealed from Fig. 9-4(a) that the crack mainly propagated in the TC for the as-sprayed specimen. On the other hand, after the thermal aging for 2000h, the crack propagated partially at the TC/BC interface as shown in Fig. 9-4(c) and (d). It can be also observed from these figures that the TGO grew at the TC/BC interface after the thermal. In the 200h and 1000h aged specimens, as shown in Fig. 9-4(b), although the TGO also grew at the TC/BC interface, the crack however mainly propagated in the TC. Typical fracture surfaces for the as-sprayed and the aged specimens are represented in Fig. 9-5. The fracture surface of the

as-sprayed specimen exhibits mainly inter-splats fracture mode, on the other hand, the aged specimen takes the mixed mode of transgranular and inter-splats fractures. The relationship between the fracture strength and the inter-splats fracture of the free-standing APS-TBC film was reported in Ref. 18. Fig. 9-6 represents the tensile strength of the free-standing APS-TBC film as a function of the area ratio of the inter-splats fracture surface [20]. From Fig. 9-6 the tensile strength increased with decreased inter-splats fracture mode. These results indicate that the inter-splats strength of TBC was increased by the sintering. It can be also considered in this work that the TC sintered during the thermal aging. The crack path in the specimen by the four-point bending test is summarized in Fig. 9-7 schematically. For the as-spray condition, because the TC has lower fracture strength compared with the TC/BC interfacial strength, the crack mainly propagated in the TC. After aging at 1000˚C for 2000h, the fracture strength of the TC became high by the sintering. On the other hand, the TC/BC interfacial strength decreased with the aging time due to the TGO nucleation and growth. Therefore the crack propagated partially at the TC/BC interface. The crack mainly propagated in the TC after the thermal aging for 200h and 1000h because the TC/BC interface maintained high strength in comparison with the TC.

The results in present work are summarized in Table 9-1. The details of experimental results are as follows.

9. 1 Effect of the distance between the stiffeners

In this work, the effect of the distance between the stiffeners on the energy release rate was also checked. The results in which the distance was 10 mm are shown in Fig. 9-8 compared with those where the distance was 5 mm. From this figure, the distance between the stiffeners was not significant for the evaluation of the energy release rate in TBC specimen.

9. 2 Effect of loading speed

In order to study the effect of the loading rate on the energy release rate, the bending tests were also performed under slow loading speed. Fig, 9-9 shows a typical load – time curve of a slow test compared with a normal speed. The loading speed of a slow test (approximately 0.6 N/sec) was ten times lower than that of a normal test (approximately 5 N/m). Fig. 9-10 shows the typical deflection – time curve of a slow test compared with a normal test. The deflection speed of the slow test was approximately 0.2 μm/s (13 μm/min) except for the delamination stage.

The average energy release rate as a function of the loading speed (also deflection speed) is shown in Fig. 9-11. In this figure, the scatter of the energy release rate is also shown by an error bar. In this figure, the average energy release rates of slow tests were almost equivalent to those of normal tests, the data of the slow test was within the scatter band of the normal test data. Therefore, there is no significant influence of the loading speed on the delamination resistance in this work.

9. 3 Effect of thermal aging

The average energy release rate as a function of aging time (at 1000˚C) was shown in Fig. 9-12. In this figure, the average energy release rate was indicated by each dot together with the scatter of the energy release rate. The number close to the scatter bar indicates the number of specimens tested for each condition, respectively. From Fig. 9-12, the average energy release rate increased with increasing aging time at 1000˚C, for both fine and coarse BC specimens. On the other hand, the scatter of the energy release rates decreased with increasing aging time.

Fig. 9-13 shows the adhesion strength of an APS-TBC determined by means of tensile tests as a function of aging time at 900˚C [19]. These tests were performed in the "Subcommittee on Superalloys and Coatings" in the Society of Materials Science, Japan (JSMS). The difference of the A1 and A3 specimens was the flying particle velocity of YSZ powder in APS. Each symbol indicates the mean value of the adhesive strength determined by using 5 – 10 specimens. Comparing Fig. 9-12 with Fig. 9-13, the trend of both results was equal, i.e. the delamination resistance increased with increasing aging time.

Fig. 9-14 shows the tensile strength and Young's modulus of the TBC film itself as a function of the aging time at 900°C [20]. Both tensile strength and Young's modulus of the TBC film itself increased with increasing aging time. It can be considered that the following mechanisms cause these phenomena of the TBC film. The as-sprayed APS-TBC has an unstable microstructure compared to the bulk YSZ materials, which was fabricated by HIP or another process. Therefore there is a possibility that the

strength of the APS-TBC can be changed by thermal aging at lower temperatures compared of the bulk YSZ. However there is no evidence, therefore further investigation must be performed.

The fracture toughness K_{Ic} of the TBC film itself and also G_{Ic}, which was calculated from K_{Ic}, are shown in Fig. 9-15 [21]. Comparing Fig. 9-15 with Fig. 9-12 the G_{IC} of TBC film itself was almost equivalent to the average energy release rate in this work for as-spray specimen. In addition, the influence of aging time of G_{IC} of TBC film itself was similar to results in this work.

From the above discussion, the effect of the thermal aging on the energy release rate is summarized in Fig. 9-16 schematically. In as-sprayed TBC specimen, the TC/BC interface has the higher strength compared with the TC. The fracture strength of the TC increases with the thermal aging by the sintering, on the other hand, the TC/BC interfacial strength decreases due to TGO growth. When the thermal aging time becomes longer than the critical certain time, the TC/BC interfacial strength becomes lower than the fracture strength of the TC. The energy release rate Gc evaluated by the four-point bending test is correlated with the fracture strength of the weakest parts of the TBC specimen. Therefore it increases with the thermal aging time until the critical time. In addition, it is easily expected that the Gc decreases with the thermal aging after the critical aging time. The critical aging time in this TBCs is approximately 2000h. The thermal aging for 10000h is now being applied to TBC specimens, which will be presented elsewhere.

The Young's modulus of the TC may also be changed during thermal aging in this work. However, it was revealed from analytical work (Sec. 5.3 a)) that the influence of the Young's modulus of TC on the energy release rate is negligible even if it is changed during thermal aging.

9. 4 Effect of TC/BC interface roughness on the delamination resistance

Comparing the energy release rate of fine and coarse BC specimens in Fig. 9-12, the influence of the TC/BC interface roughness on delamination resistance wasn't significant.

9. 5 Propagation rate of delamination crack

Fig. 9-17 shows the relationship between the peak deflection rate (i.e. crack growth rate) and the aging time. In this figure, the scatter of the peak deflection rate was also shown by an error bar. From Fig. 9-7 the peak deflection rate, i.e. delamination crack growth rate, increased with increasing aging time. During the 4-point bending test, different behaviors of crack initiation and propagation were observed. Since this observation, it was also seen that the delamination crack growth rate for as-sprayed specimens was much lower than that for aged specimens, for both of fine and coarse bond coat specimens.

The mechanism of this phenomenon was not clear. However, following possibilities can be considered.

1. The delamination of aged specimen occurred at higher critical load compared with as-spray specimen. Therefore the higher load may induce the higher crack propagation rate.
2. If the connection of splats for as-spray TBC was looser than that for aged TBC, the crack propagation may be disturbed by the shielding effects produced by micro-crack nucleation near the delamination crack-tip.

However, there is no evidence for above consideration, therefore further investigations, such as metallurgical ones, must be performed.

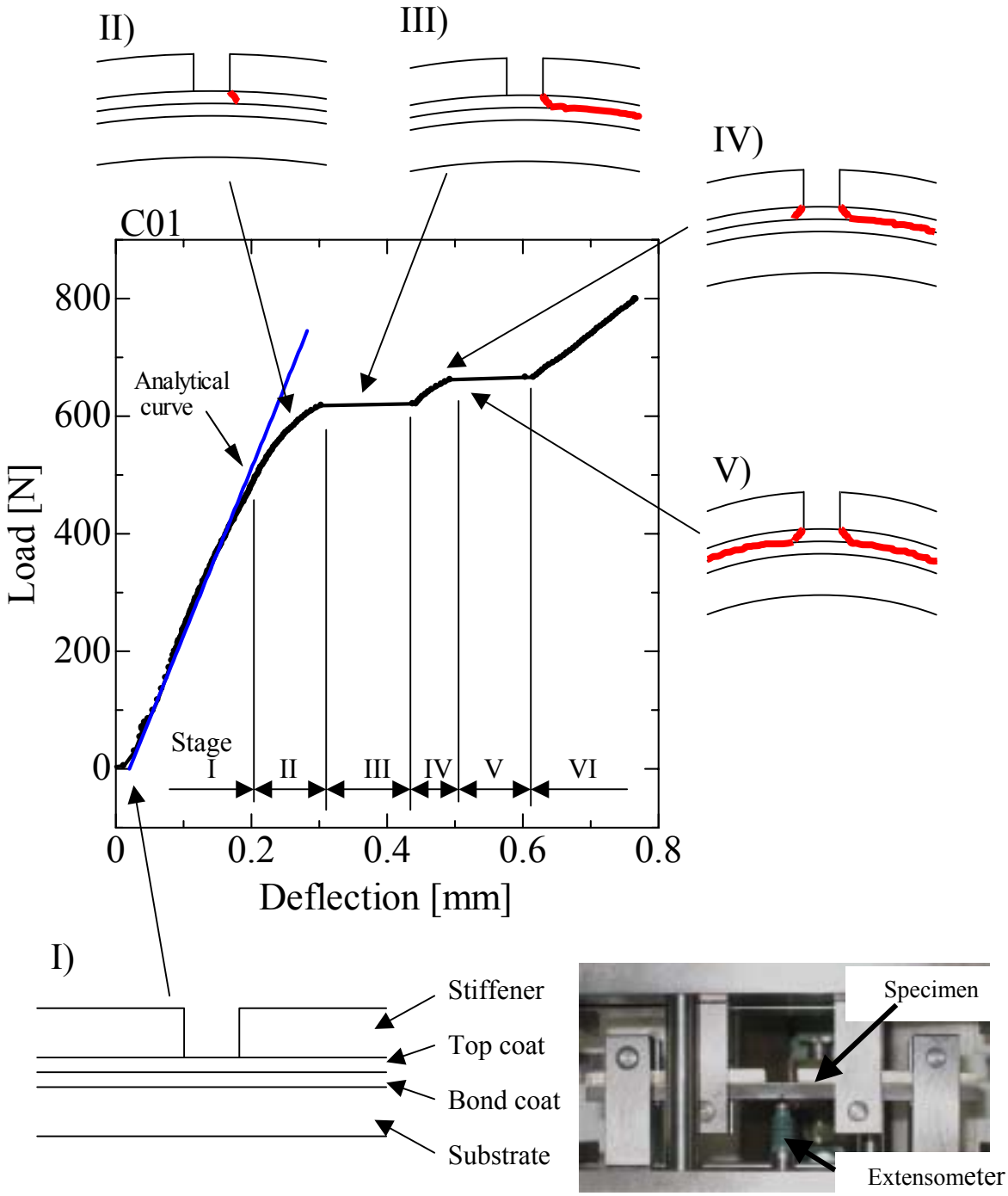

Fig. 9-1 Typical load-deflection curve during 4-point bending test.

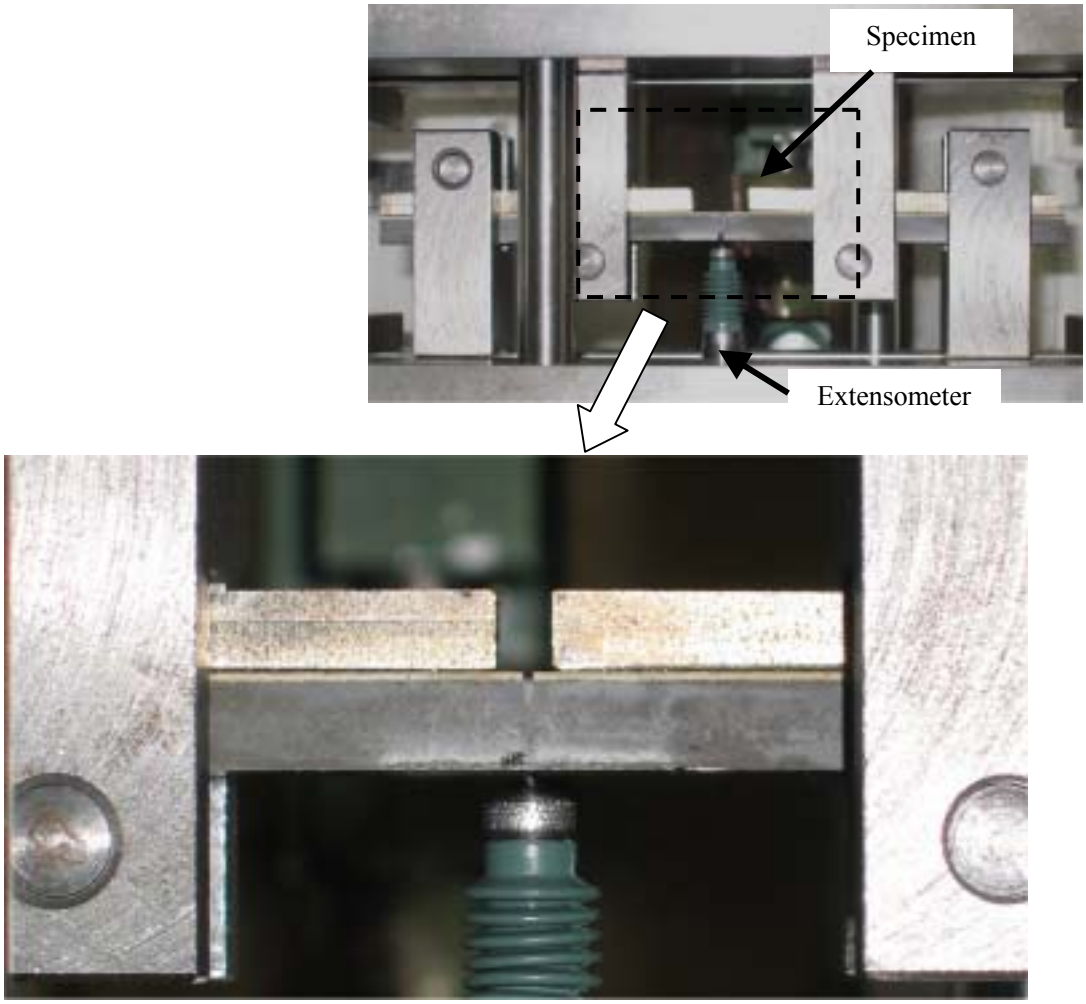

(a) before test: Corresponding to i) in Fig. 9-1

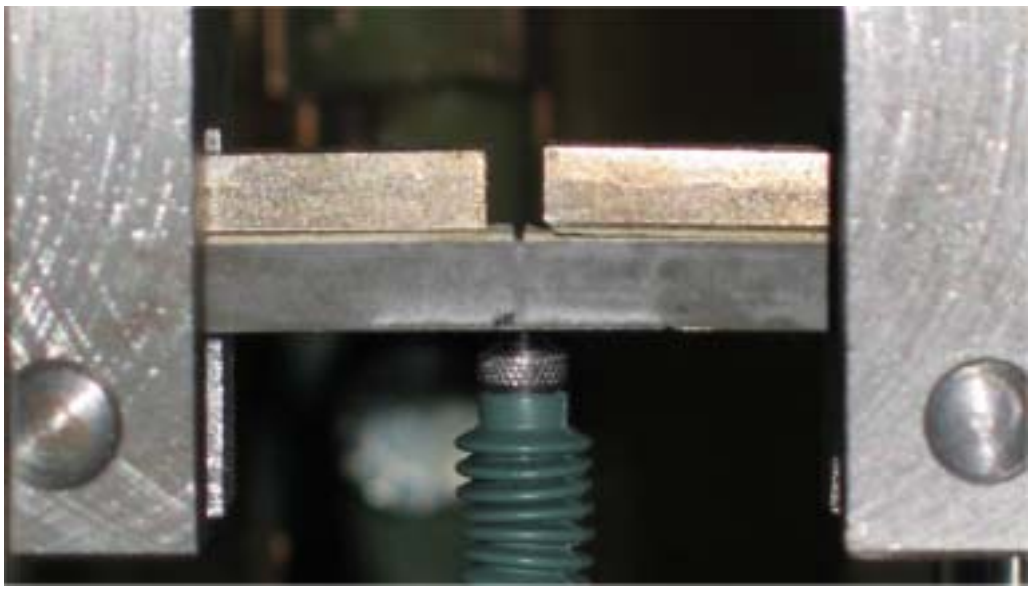

(b) Delamination crack initiated and propagated (right side only) : Corresponding to iii) in Fig. 9-1

Fig. 9-2 Initiation and propagation morphologies of delamination crack during test (continued).

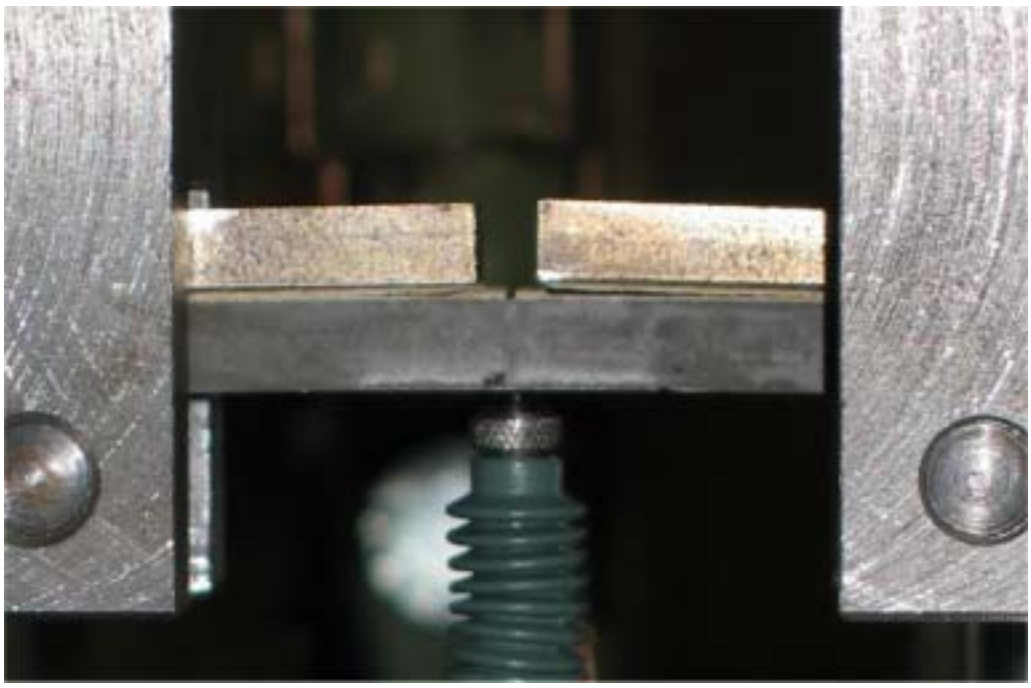

(c) Delamination crack initiated and propagated (other side) : Corresponding to v) in Fig. 9-1

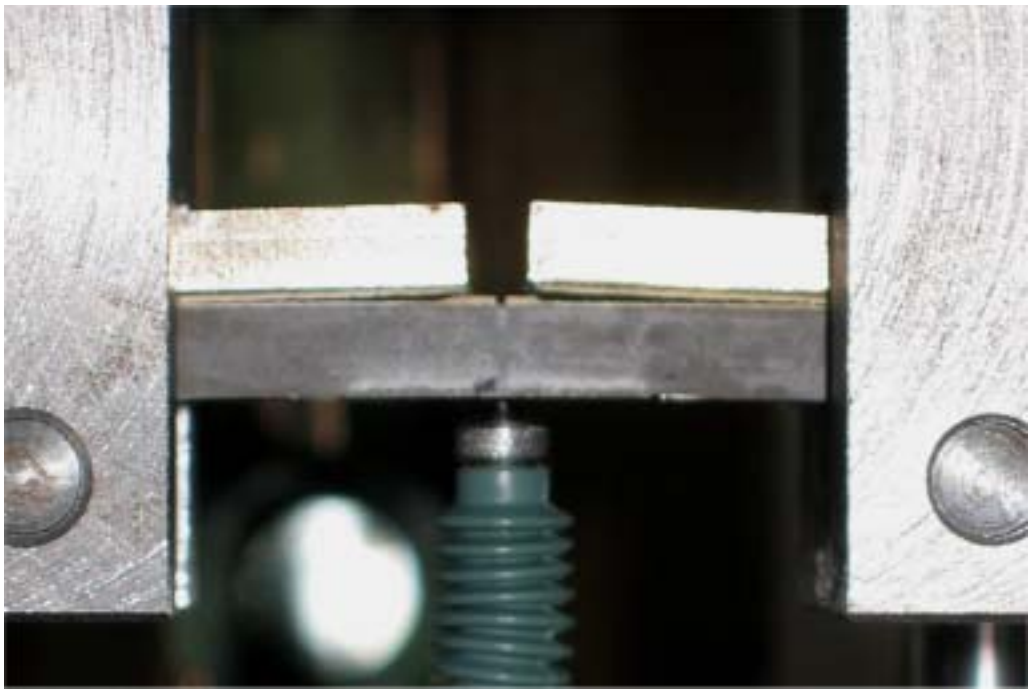

(d) Aspect of delamination

Fig. 9-2 Initiation and propagation morphologies of delamination crack during test.

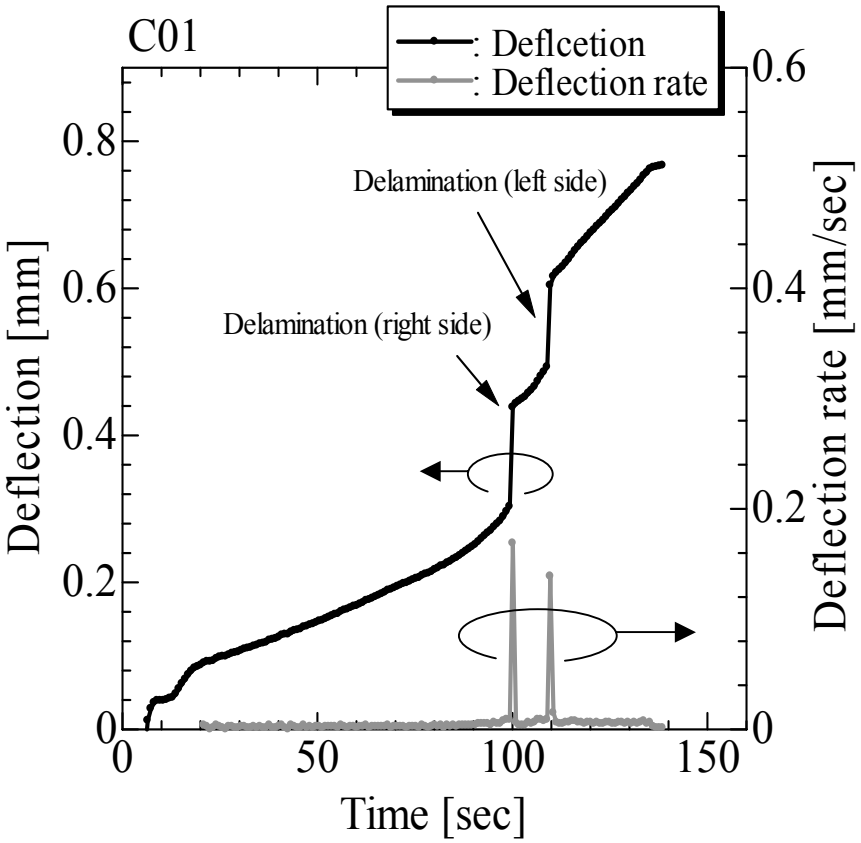

Fig. 9-3 Typical deflection-time curve during 4-point bending test.

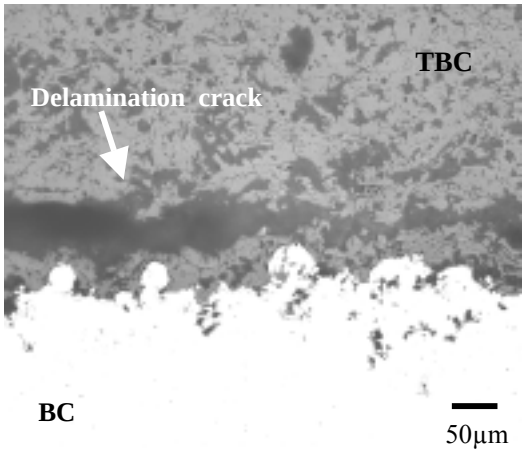

(a) As-sprayed, fine BC specimen.

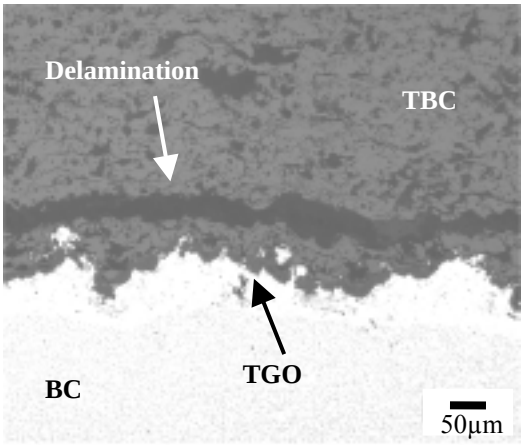

(b) Aged at 1000°C for 200h, fine BC specimen

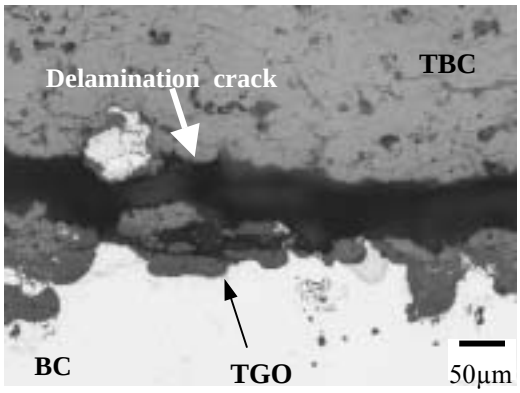

(c) Aged at 1000°C for 2000h, fine BC specimen

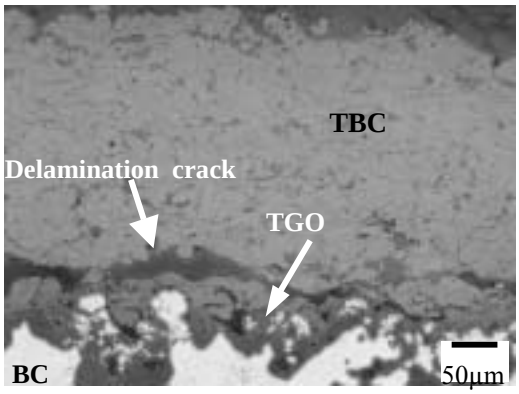

(d) Aged at 1000°C for 2000h, coarse BC specimen

Fig. 9-4 Microphotographs of the crack propagation path after the tests (cross section).

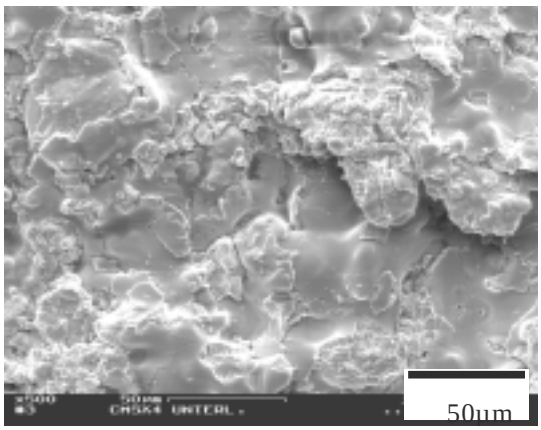

(a) As-sprayed, coarse BC specimen.

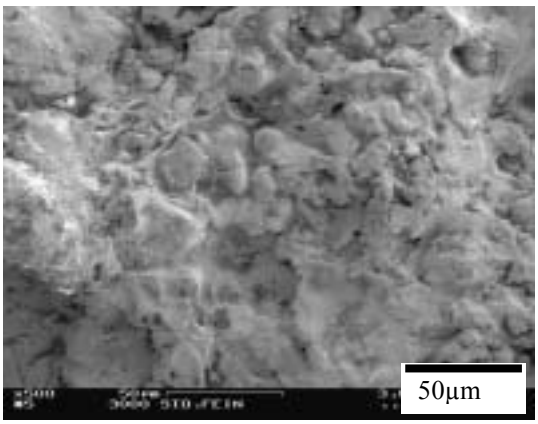

(b) Aged at 1000°C for 2000h, coarse BC specimen.

Fig. 9-5 Typical fracture surfaces after the tests.

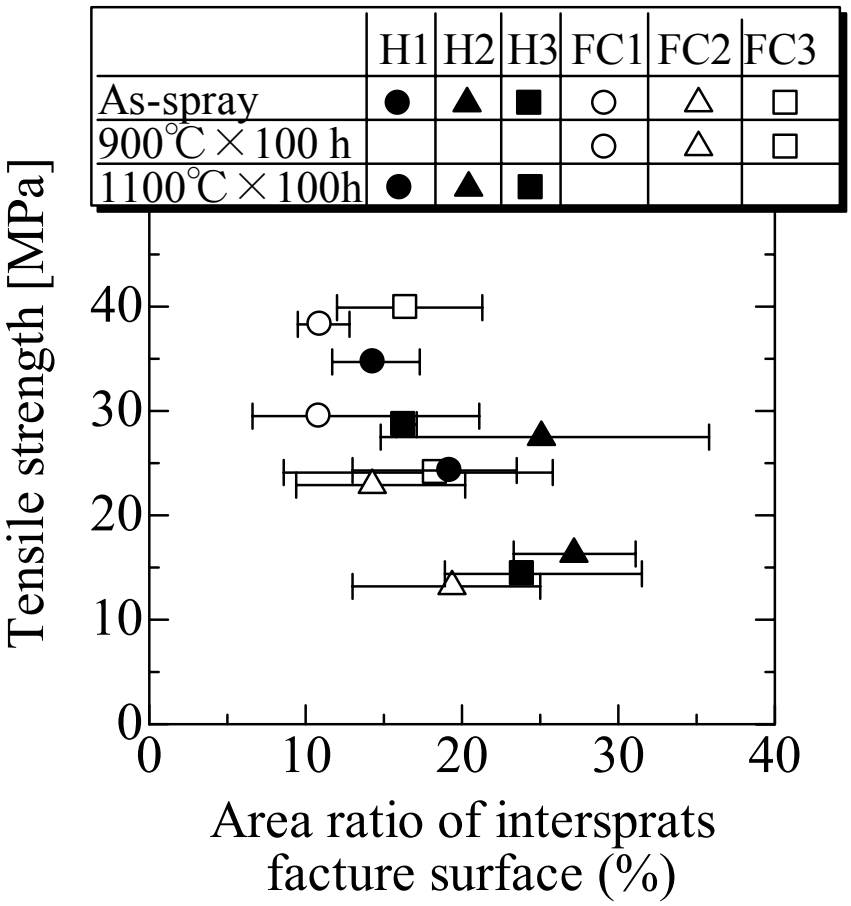

Fig. 9-6 Tensile strength of free-standing APS-TBC film as a function of the area ration of inter-splats fracture surface; H1-H3 used the hollow powder, FC1-FC3 used the fused crashed powder [20].

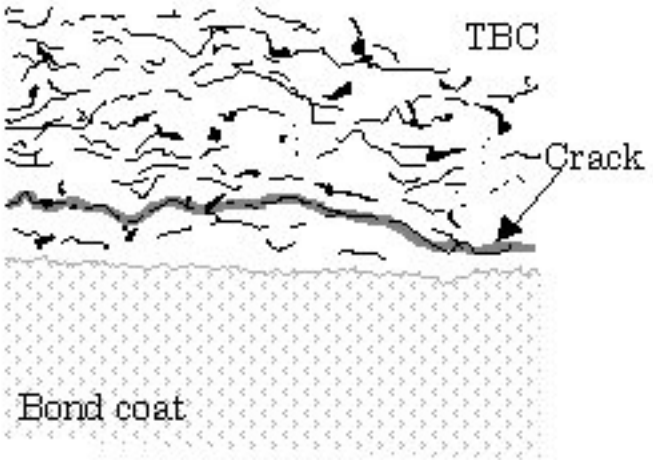

(a) As-sprayed

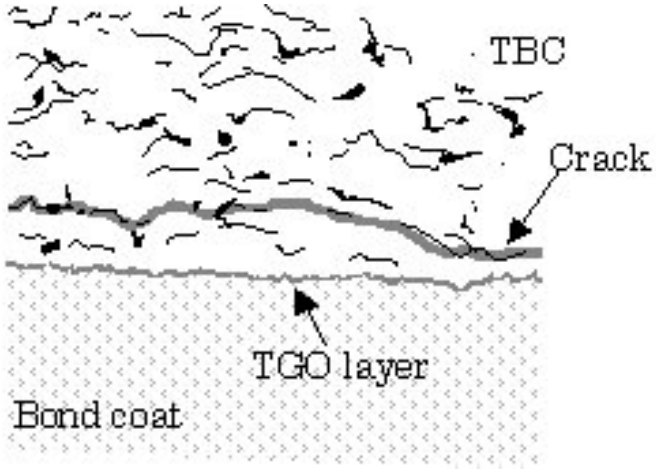

(b) Aged for 200h and 1000h

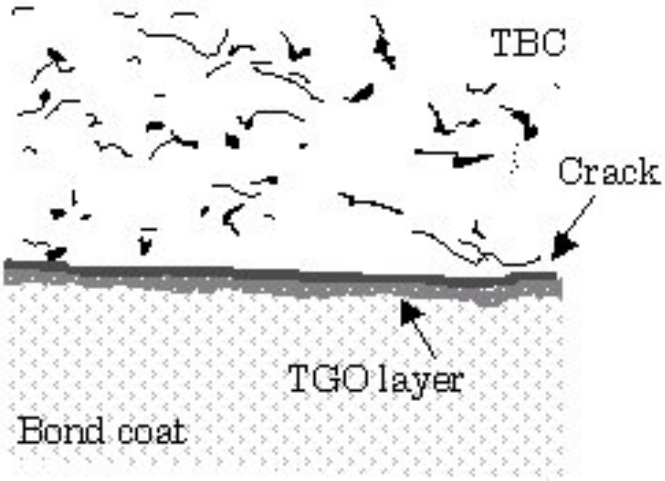

(c) Aged for 2000h

Fig. 9-7 Schematic illustration of fracture mode in TBC specimen by the 4-point bending tests: Aging temperature = 1000°C.

Table 9-1 Summary of 4-point bending test .

(a) Fine BC specimen

TP	Side	Aging time [h]	TGO thickness [μm]	Gc [N/m]	P [N]	dL/dt max [μm/sec]	notes
C01	Right	0	0	158,8	621	168,8	
	Left	0	0	182,7	666	138,8	
C02	Right	0	0				Error
	Left	0	0	125,5	552	43,8	
C03	Right	0	0	134,3	571		lower rate
	Left	0	0	123,2	547		lower rate
C04	Right	0	0	165,0	633	107,5	DS=10mm
	Left	0	0	185,4	671	87,5	DS=10mm
C05	Right	200	3	201,6	701	124,4	
	Left	200	3	201,6	701	124,4	
C06	Right	200	3	139,4	583	38,8	
	Left	200	3	227,0	744	200,0	
C07	Right	1000	5	242,5	770	217,5	
	Left	1000	5	233,8	756	201,3	
C08	Right	1000	5	213,2	722	116,3	
	Left	1000	5	214,4	724	77,5	
C09	Right	2000	7	240,0	767	128,1	
	Left	2000	7	240,0	767	128,1	
C10	Right	2000	7	253,9	789	196,3	
	Left	2000	7	250,7	784	124,4	

DS: Distance between stiffeners

(b) Coarse BC specimen

TP	Side	Aging time [h]	TGO thickness [μm]	Gc [N/m]	P [N]	dL/dt max [μm/sec]	notes
C12	Right	200	3	230,0	746	50,8	
	Left	200	3	214,2	720	148,8	
C13	Right	200	3	209,5	712	156,3	
	Left	200	3	209,5	712	156,3	
C14	Right	1000	5	210,7	715	173,8	
	Left	1000	5				Error
C15	Right	1000	5	256,5	789	176,3	
	Left	1000	5				Error
C16	Right	2000	7	215,4	724	161,3	
	Left	2000	7	217,2	727	122,0	
C17	Right	2000	7	249,4	779	207,5	
	Left	2000	7	248,1	777	223,8	
C18	Right	0	0	122,8	544	96,3	
	Left	0	0				Error
C19	Right	0	0	132,4	565	65,0	
	Left	0	0	155,9	613	66,3	
C20	Right	0	0	112,6	521		lower rate
	Left	0	0	121,4	541		lower rate

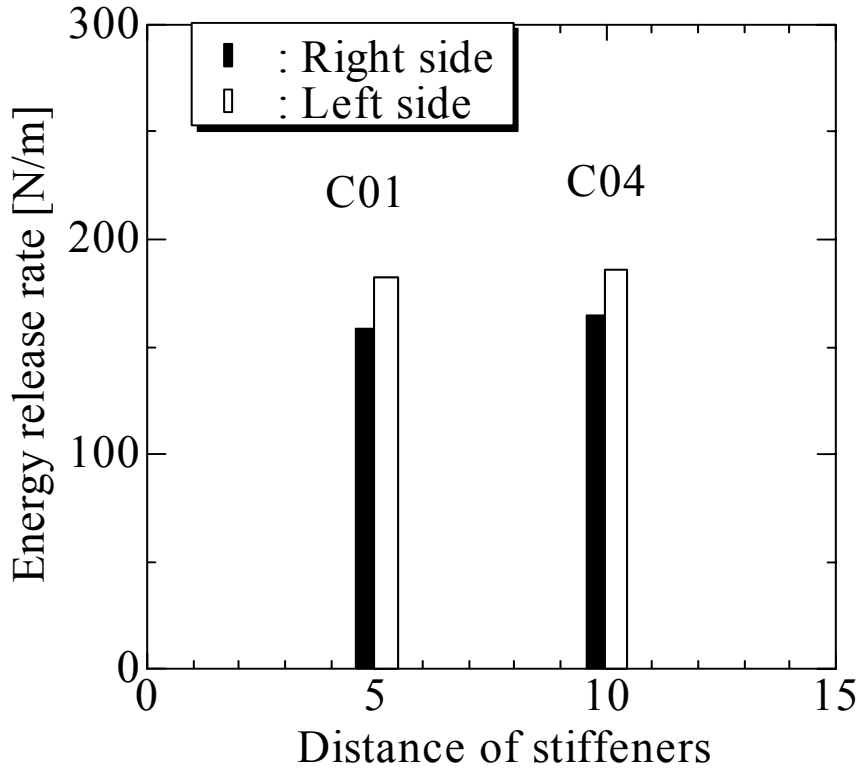

Fig. 9-8 Effect of distance between stiffeners on energy release rate.

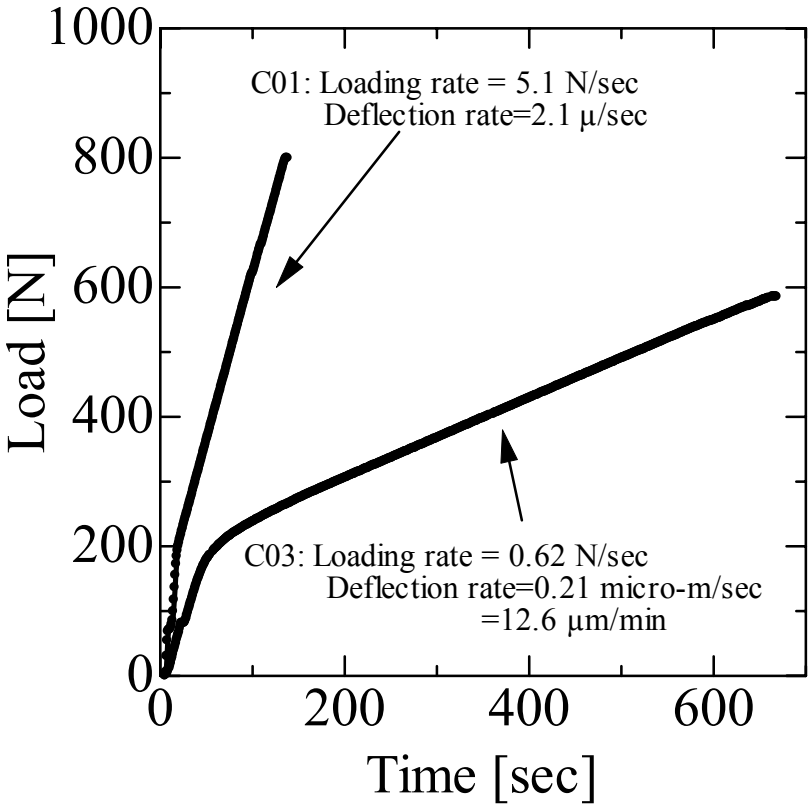

Fig. 9-9 Load – time curve under different loading speed conditions.

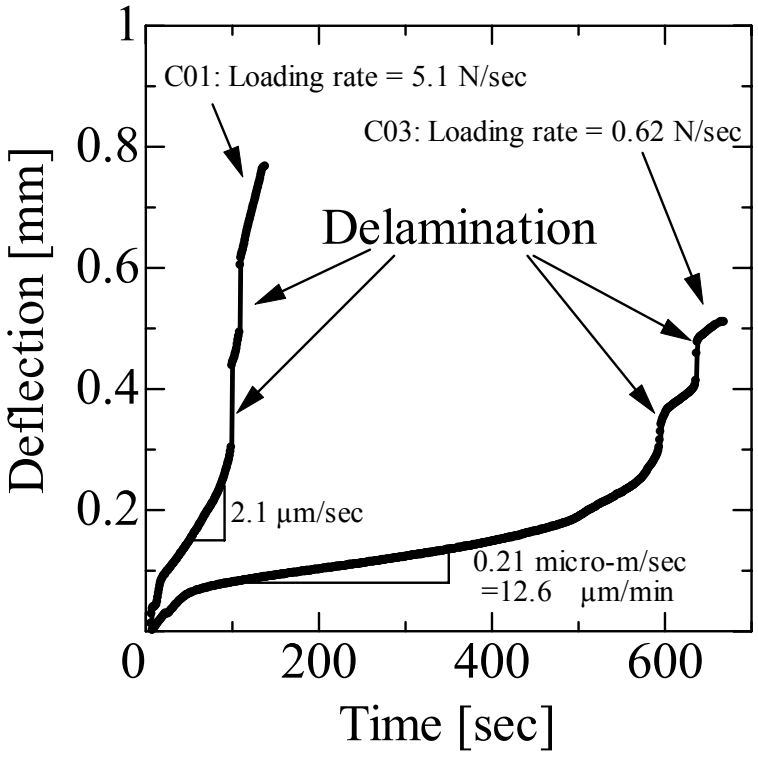

Fig, 9-10 Deflection – time curve under different loading speed conditions

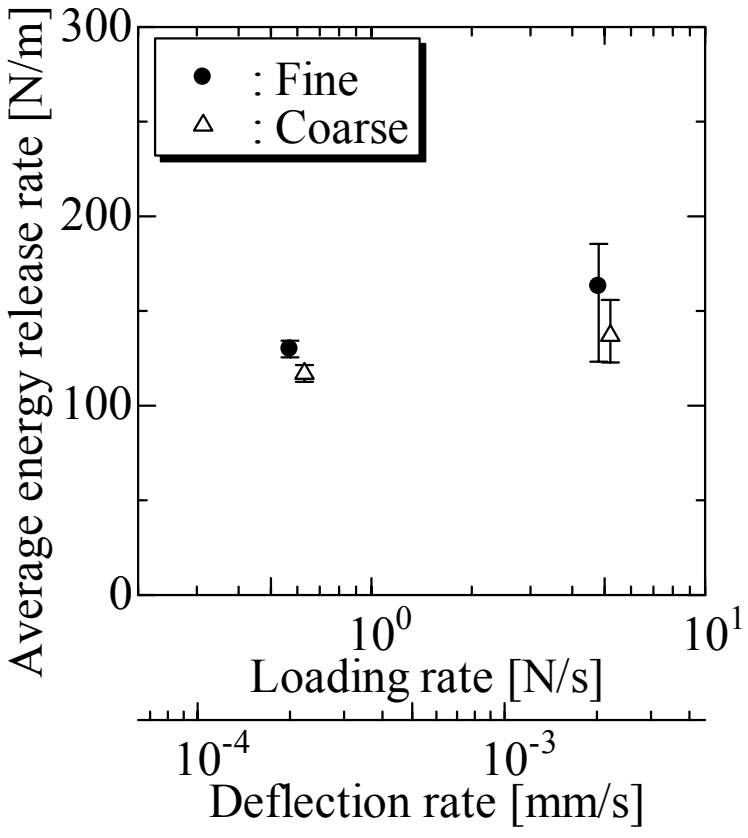

Fig. 9-11 Effect of loading speed on the energy release rate of TBC specimen.

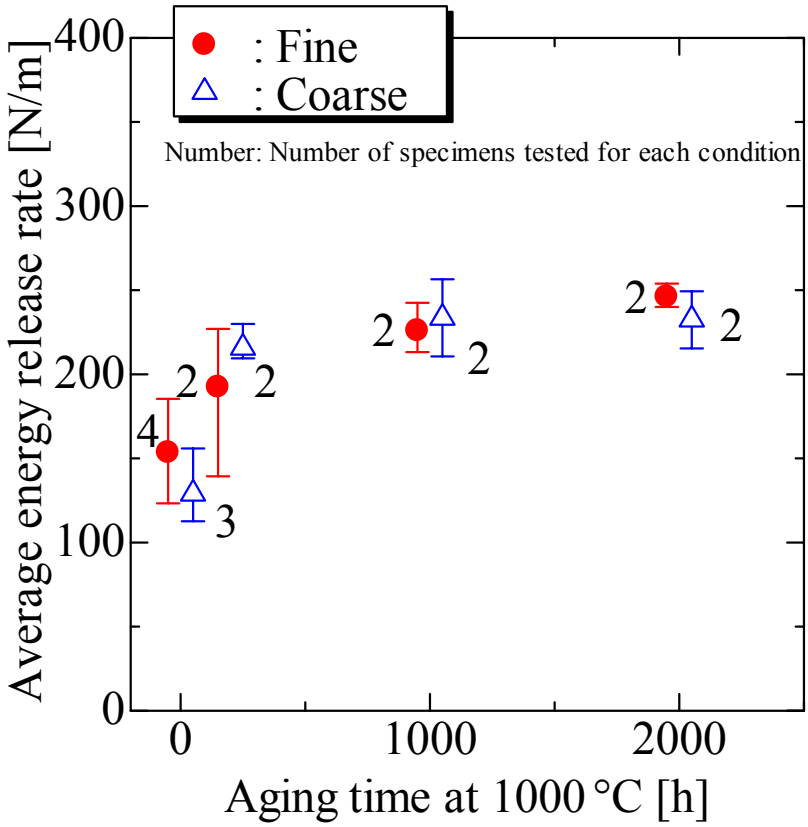

Fig. 9-12 Effect of thermal aging on delamination resistance in TBC.

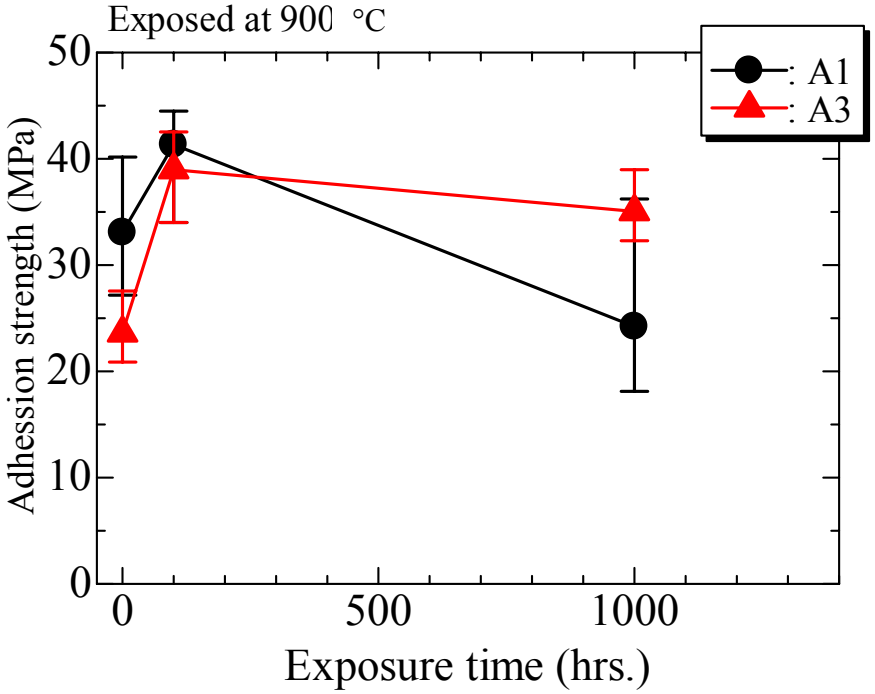

Fig. 9-13 Relationship between adhesion strength of APS-TBC and aging time at 900˚C [19].

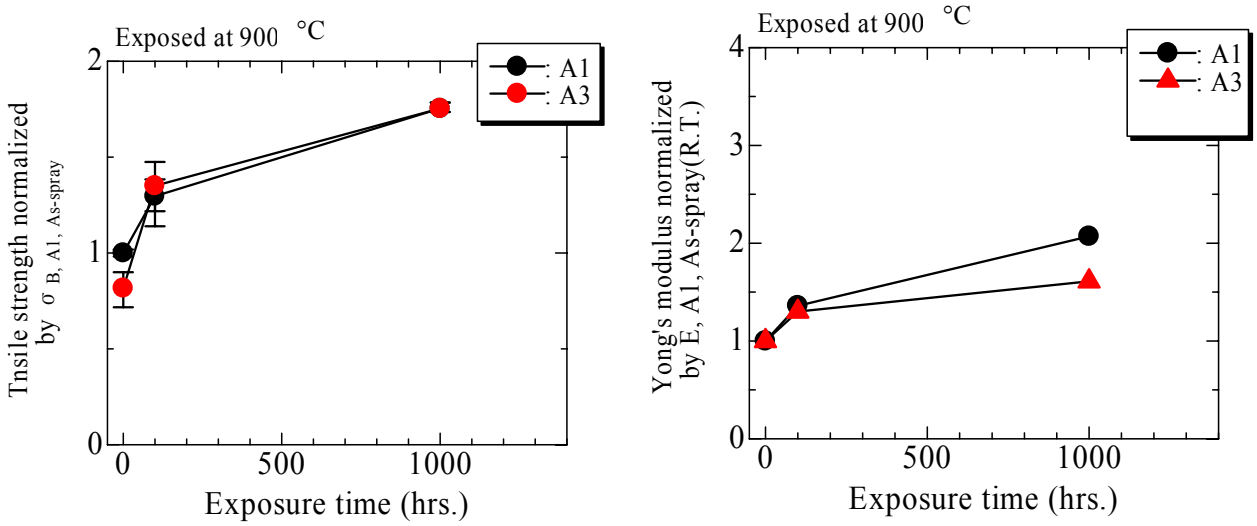

(a) tensile strength (b) Young's modulus

Fig. 9-14 Tensile strength and Young's modulus of TBC film itself correlated with aging time [20].

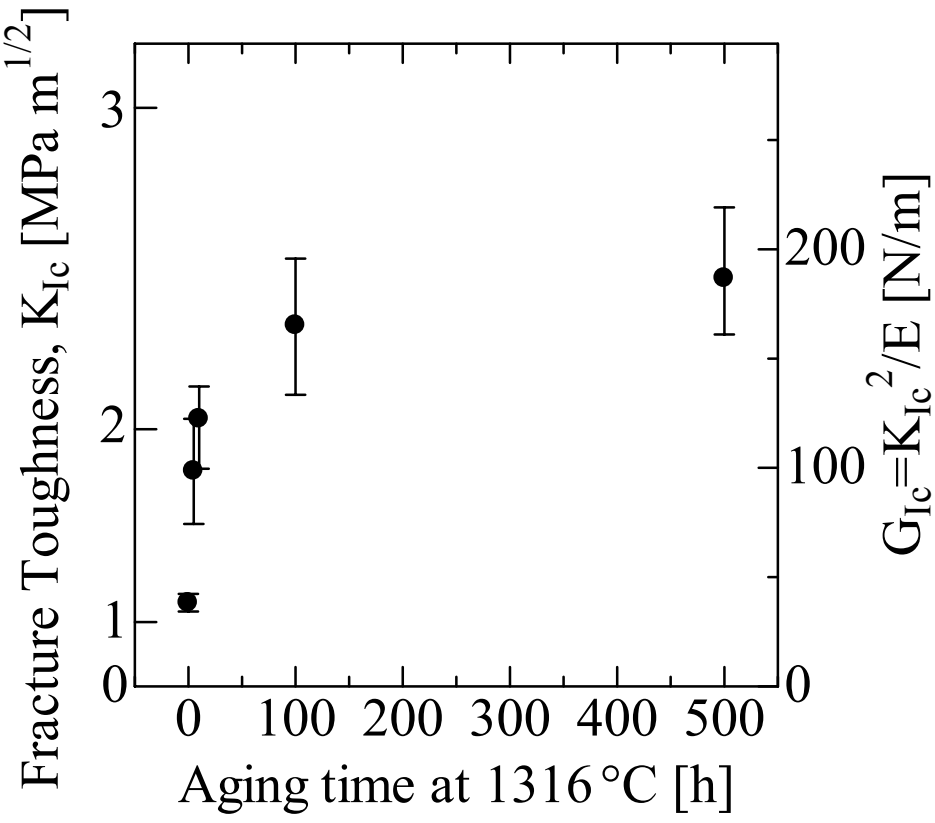

Fig. 9-15 Fracture toughness as a function of aging time for APS-8YSZ film itself at 1316°C in air [21]; by means of bending test of single-edge-precracked-beam specimen.

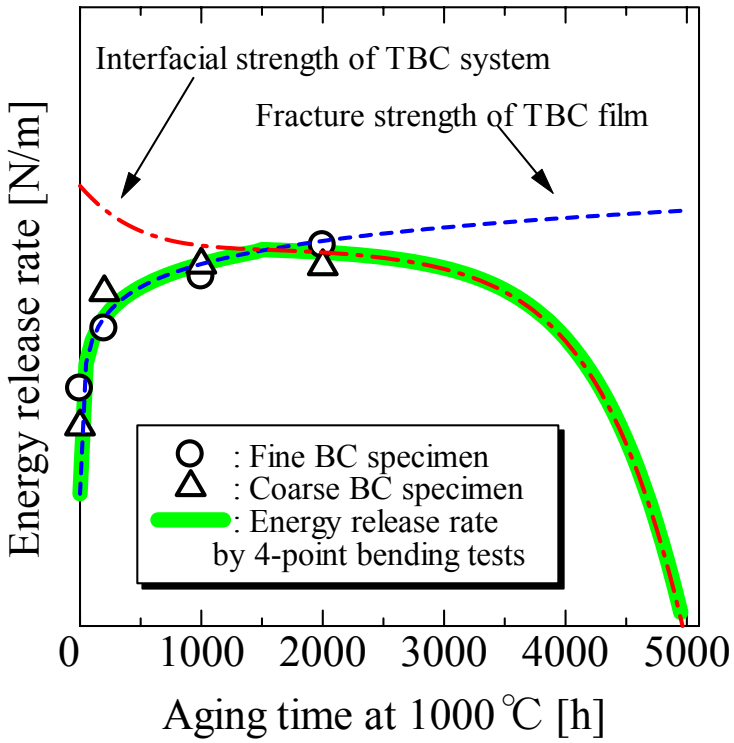

Fig. 16 Schematic illustration of the energy release rate of the TBC specimen evaluated by the 4-point bending tests.

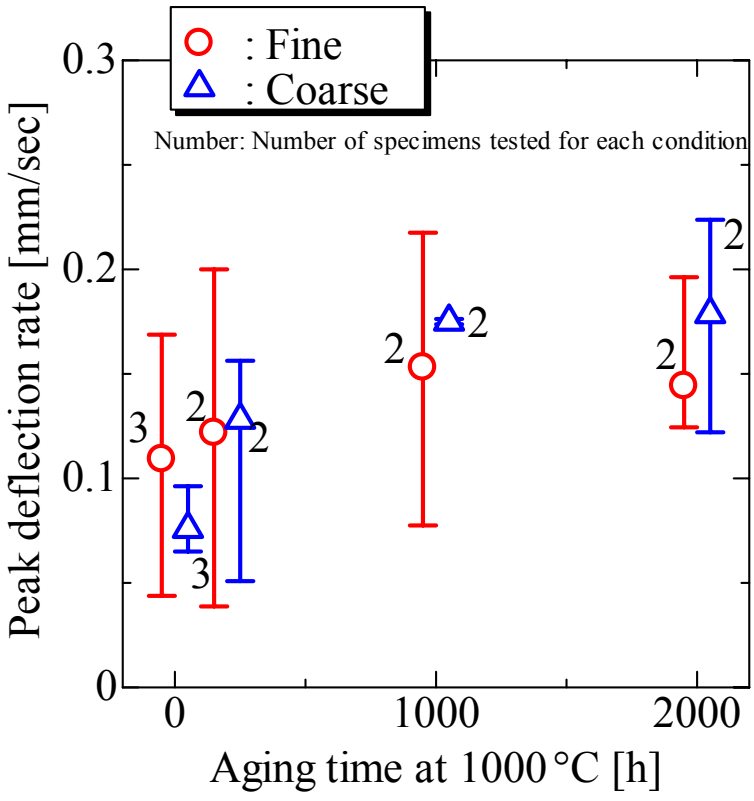

Fig. 9-17 Effect of thermal aging on peak deflection rate.

10. Summary and Conclusions

In this study, the evaluation of the delamination resistance in TBC systems was carried out by means of four point bending tests. The effects of thermal aging and top-coat/bond-coat interface roughness on the delamination resistance were also discussed. The following conclusions were made:

1. The 4 – point test rig was designed and manufactured. The 4–point bending tests by using this equipment can be performed with great accuracy and great reproducibility.
2. The heat curing type epoxy adhesive, Araldite AT1, was selected and used for bonding the stiffener on the top coating. From SEM and EDX analyses, the adhesive infiltrated approximately 100μm in depth into top coat and there is no significant influence of the infiltration on the energy release rate by delamination.
3. The equation of estimating energy release rate was modified and extended for TBC systems. From analytical considerations, the effect of the Young's modulus of the top coating on the energy release rate is negligible even if it was changed during thermal aging.
4. The energy release rate G_c, which was estimated by the four-point bending tests, was independent with the loading rate and the top-coat/bond-coat interface roughness
5. The energy release rates estimated under slow loading condition were almost equivalent to those under higher loading conditions. Therefore, the energy release rate of TBC specimen was independent of the loading rate.
6. Comparing energy release rates in between fine and coarse bond coating specimens, the effect of top-coat/bond-coat interface roughness wasn't significant on the delamination resistance.
7. The crack mainly propagated in the top coating for as-spray condition, however the crack propagated partially at the top-coat/bond-coat interface after the thermal aging for 2000h.
8. The G_c was correlated with fracture strength of weakest parts of the TBC specimen. The G_c increases with the thermal aging until the critical time due to the sintering of the top-coating. It can be expected that the G_c decreases with the thermal aging after the critical aging time because the top-coat/bond-coat interfacial strength decreases by the TGO growth. The critical aging time in the present work is approximately 2000h.
9. The delamination crack growth rate increased with increasing aging time.

Future work

Following articles must be investigated in near future.

(a) Effect of thermal cycle on delamination resistance

In this work, the delamination resistance increased with increasing iso-thermal aging time because of the increasing fracture resistance of TBC film itself. However it can be considered that the thermal cycle induce the micro delamination crack near the interface due to thermal stress cycle. Therefore the delamination resistance may be reduced by thermal cycle.

(b) Effect of test temperature on the delamination resistance

The influence of the test temperature on the delamination resistance must be investigated because TBC systems undergo thermal cycle between room temperature and elevated temperature (up to 900°C). If the delamination resistance is estimated by modified Charallambides four-point bending test, the adhesive that is applicable at elevated temperature is necessary. Other bonding methods, such as brazing, must be used because usual adhesives can't be applied at elevated temperature. Even if the stiffener is bonded by braze, the test results may be affected by residual stress because the brazing temperature must be higher than test temperature. Therefore other test methods may be necessary.

(c) Effect of loading mode on delamination resistance

Mode I loading is dominant near the delamination crack tip in the tensile test. In modified Charallambides four-point bending test (present study), the stress condition near the delamination crack tip is mixed mode of I and II, but Mode I may be dominant because the stiffing layer is thick enough (FEM analysis is necessary). On the other hand, the Mode II stress condition, which is produced by thermal stress due to the mismatch of the thermal expansion coefficient, may be dominant in the actual turbine brad and vane. Therefore the effect of loading mode on the delamination resistance must be investigated. A modified or a new test method may be necessary.

Acknowledgements

The author is grateful to Prof. Dr.–Ing. C. Berger, Dr.–Ing. A. Scholz, Mr. A. Schmidt and Mr. S. Linn of Institute of Materials Technology, Darmstadt University of Technology. The author is also grateful to helpful discussions with Prof. Dr. –Ing. H. W. Grünling and Dr.-Ing. W. Stamm. The author gratefully thanks all of the staff of the department of high temperature material and all of the staff in the work shop of the Institute of Materials Technology, Darmstadt University of Technology.

References

1. Bernstein, H. L., Grant, T. S., McClung, R.C., and Allen, J.M., “Prediction of Thermal-Mechanical Fatigue Life for Gas Turbine Blades in Electric Power Generation,” ASTM STP1186, American Society for Testing and Materials, Philadelphia, 1993, pp. 212–238.
2. National Research Council, Coatings for High Temperature Structural Materials —Trends and Opportunities—, National Academy Press, Washington, D.C., 1996.
3. Seth, B.B., “Superalloys: The Utility Gas Turbine Perspective,” Superalloy 2000, TMS, Warrendale, PA, 2000, pp. 3-16.
4. Schneider, K. and Grunling, H.W., “Mechanical Aspects of High Temperature Coatings,” Thin Solid Films, Vol. 107, 1983, pp. 395–416.
5. Hocking, M.G., Vasantathan, V., and Sidky, P.S., Metallic and Ceramic Coatings, Longsman Scientific & Technical Publishers, London, 1989.

6. H. Echosler, D. Renusch and M. Schütze, “Kinetics of the Evaluation of Physical Defects in the TGO and its Vicinity for Life Time Prediction of TBC Systems”, Proc. of Turbomat Symposium (2002) pp. 17-19
7. D. Renusch, H. Echosler and M. Schütze, Progress in Life Time Modeling of APS-TBC Part I: Critical strains Macro-Cracking, and Thermal Fatigue (2002)
8. H. Echosler, D. Renusch and M. Schütze, “Bond coat oxidation and its significance for life expectancy of thermalk barrier coating systems”, Material Science and Technology, **vol. 20** (2004) pp. 307-318.
9. T. Xu, S. Faulhaber, C. Mercer, M. Maloney and A. Evans, “Observation and analyses of failure mechanisms in thermal barrier systems with two phase bond coats based on NiCoCrAlY”, Acta Materialia, **Vol 52** (2004) pp. 1439-1450.
10. M. S, Ali, S. Song and P. Xiao, “Degradation of thermal barrier coatings due to thermal cycling up to 1150˚C”, J. of Material Science, **Vol. 37** (2002) pp. 2097-2102.
11. I. Hofinger, M. Oechsner, H. Barhr and M. V. Swain, “Modified four-point bending specimen for determining the interface fracture energy for thin, brittle layers”, Int. J. of Fracture, **vol. 92** (1998) pp. 213-220.
12. A. K. Ray, N. Roy, and K. M. Godiwalla, “Crack propagation studies and bond coat properties in thermal barrier coatings under bending”, Bull. Mater. Sci. **Vol. 24**, No. 2 (2001) pp.203-208.
13. P. G. Charallambides, J. Lund, A. G. Evans and R. M. McMeeking, “A Test Specimen for Determining the Fracture Resistance of Bimaterial Interface”, J. of Applied Mechanics, **vol. 56**, March (1989) pp. 77-82
14. D. Renusch, H. Echsler and M. Schütze, “New approaches to the understanding of failure and life time prediction of thermal barrier coating systems”, Conf. Proc. in Life Time Modeling of High Temperature Corrosion Process (M. Schütze, W. J. Quadakkers and J. R. Nicholls Edts), **EFC-Publication No.34** (2001) pp.324-338.
15. T. Onoki, K. Ogawa, T. Shoji and H. Torigoe, “Influence of thermal aging on interface delamination of thermal barrier coatings”
16. M. Arai, U. Iwata, T. Sakuma and M. Saitoh, “Effect of a delamination initiation strength between thermal barrier coating and base metal on thermal aging“, J. Soc. Mat. Sci., Japan, **Vol. 49**, No. 8 (2000) pp.912-918.
17. K. Takaki, K. Kubo and K. Fujiyama, Report of sub-committee “Superalloy and coatings”, no-printed.
18. K. Ogawa, Report of sub-committee “Superalloy and coatings”, no-printed.
19. Subcommittee on Superalloys and Coatings JSMS, Proceedings of the Symposium on Strength of Materials at High Temperature (2005) 157 (in Japanese).
20. K. Kaise, Y. Yamazaki, M. Okazaki and H. Fukanuma, Proceedings of the 2004 Annual Meeting of the JSME/MMD (2004) 219 (in Japanese).

21. S. R Choi, D. Zhu and R. A. Miller “Mode I, Mode II, and Mixed-Mode Fracture of Plasma-Sprayed Thermal Barrier Coatings at Ambient and Elevated Temperatures”, **NASA/TM-2003-212185** (2003).